

1980

SANDIA REPORT

SAND91--1532 • UC--610

Unlimited Release

Printed September 1991

MELCOR 1.8.1 Assessment: LACE Aerosol Experiment LA4

L. N. Kmetyk

Prepared by
Sandia National Laboratories
Albuquerque, New Mexico 87185 and Livermore, California 94550
for the United States Department of Energy
under Contract DE-AC04-76DP00789

Issued by Sandia National Laboratories, operated for the United States Department of Energy by Sandia Corporation.

NOTICE: This report was prepared as an account of work sponsored by an agency of the United States Government. Neither the United States Government nor any agency thereof, nor any of their employees, nor any of their contractors, subcontractors, or their employees, makes any warranty, express or implied, or assumes any legal liability or responsibility for the accuracy, completeness, or usefulness of any information, apparatus, product, or process disclosed, or represents that its use would not infringe privately owned rights. Reference herein to any specific commercial product, process, or service by trade name, trademark, manufacturer, or otherwise, does not necessarily constitute or imply its endorsement, recommendation, or favoring by the United States Government, any agency thereof or any of their contractors or subcontractors. The views and opinions expressed herein do not necessarily state or reflect those of the United States Government, any agency thereof or any of their contractors.

Printed in the United States of America. This report has been reproduced directly from the best available copy.

Available to DOE and DOE contractors from
Office of Scientific and Technical Information
PO Box 62
Oak Ridge, TN 37831

Prices available from 00150-576-8401, FTS 026-8401

Available to the public from
National Technical Information Service
US Department of Commerce
5285 Port Royal Rd
Springfield, VA 22161

NTIS price codes
Printed copy: A07
Microfiche copy: A01

SAND91-1532
Unlimited Release
Printed September 1991

MELCOR 1.8.1 Assessment: LACE Aerosol Experiment LA4

L. N. Kmetyk
Thermal Hydraulic Analysis Division
Sandia National Laboratories
Albuquerque, NM 87185

Abstract

The MELCOR code has been used to simulate LACE aerosol experiment LA4. In this test, the behavior of single- and double-component, hygroscopic and non-hygroscopic aerosols in a condensing environment was monitored. Results are compared to experimental data, and to CONTAIN calculations. Sensitivity studies have been done on time step effects and machine dependencies; thermal-hydraulic parameters such as condensation on heat structures and on pool surface, and radiation heat transfer; and aerosol parameters such as number of MAEROS components and sections assigned, the degree to which plated aerosols are washed off heat structures by condensate draining, and the effect of non-default values for shape factors and diameter limits.

MASTER

Table of Contents

1	Introduction	1
2	Facility and Test Description	3
3	MELCOR Computer Model	9
4	Final Reference Calculation Results	13
4.1	Thermal Hydraulic Response	13
4.2	Aerosol Behavior	18
5	Time Step Effects and Machine Dependency	31
5.1	Machine Dependencies	31
5.2	Time Step Effects	31
6	Aerosol Sensitivity Studies	41
6.1	Aerosol "Washdown"	41
6.2	Number of MAEROS Aerosol Components	41
6.3	Number of MAEROS (Size) Sections	48
6.4	Use of (Non)Default RN Parameters	53
7	Thermal/Hydraulic Sensitivity Studies	59
7.1	Condensation on Pool Surface	59
7.2	Condensation on Walls	62
7.3	Radiation Heat Transfer	64
7.4	Insulation Thermal Conductivity	72
8	Comparison to CONTAIN	84
9	Code Limitations Identified	89
10	Summary and Conclusions	91
	Bibliography	95
A	Reference Calculation Input Deck	99

List of Figures

2.1	Schematic Diagram of the LACE CSTF Test Facility	4
4.1.1	Total and Steam Partial Pressures - Final Reference Results	14
4.1.2	Atmosphere and Pool Temperatures - Final Reference Results	16
4.1.3	Pool Masses - Final Reference Results	17
4.1.4	Condensation Mass Fluxes - Final Reference Results	19
4.1.5	Inside (top), Interface (middle) and Outside (bottom) Wall Temperatures - Final Reference Results	20
4.1.6	Leakage Mass Flow Rates - Final Reference Results	21
4.2.1	Suspended Aerosol Masses - Final Reference Results	22
4.2.2	CsOH (top) and MnO (bottom) Suspended Aerosol Masses - Final Reference Results	23
4.2.3	Saturation Ratio (top) and Water Aerosol Mass (bottom) for Suspended Aerosols - Final Reference Results	25
4.2.4	Aerodynamic Mass Median Diameter (top) and Geometric Standard Deviation (bottom) for Suspended Aerosols - Final Reference Results	27
4.2.5	Size Distributions at ~4400s (top) and ~11000s (bottom) for Suspended Aerosols - Final Reference Results	28
5.1.1	Total and Steam Partial Pressures - Machine Dependency Sensitivity Study	32
5.1.2	Suspended Aerosol Masses - Machine Dependency Sensitivity Study	33
5.1.3	Total CPU Run Times (top) and VAX Package Run Times - Machine Dependency Sensitivity Study	34
5.2.1	Total and Steam Partial Pressures - Time Step Sensitivity Study	36
5.2.2	Atmosphere and Pool Temperatures - Time Step Sensitivity Study	37
5.2.3	Suspended Aerosol Masses - Time Step Sensitivity Study	38
5.2.4	Total CPU Time - Time Step Sensitivity Study	39
6.2.1	Suspended Aerosol Masses - Aerosol Component Sensitivity Study	43
6.2.2	Aerodynamic Mass Median Diameter (top) and Geometric Standard Deviation (bottom) for Suspended Aerosols - Aerosol Component Sensitivity Study	45
6.2.3	Size Distributions at ~11000 for One-Component (top) and Three-Components (bottom) for Suspended Aerosols - Aerosol Component Sensitivity Study	47

6.2.4	Total CPU Run Times - Aerosol Component Sensitivity Study	47
6.3.1	Suspended Aerosol Masses - Aerosol Sections Sensitivity Study	49
6.3.2	Aerodynamic Mass Median Diameter (top) and Geometric Standard Deviation (bottom) for Suspended Aerosols - Aerosol Sections Sensitivity Study	51
6.3.3	Size Distributions at $\sim 11000s$ for 5- (top) and 10- (bottom) Sections for Suspended Aerosols - Aerosol Sections Sensitivity Study	52
6.3.4	Total CPU Run Times - Aerosol Sections Sensitivity Study	54
6.4.1	CsOH (top) and MnO (bottom) Suspended Aerosol Masses - Shape Factors Sensitivity Study	55
6.4.2	Aerodynamic Mass Median Diameter (top) and Geometric Standard Deviation (bottom) for Suspended Aerosols - Shape Factors Sensitivity Study	56
6.4.3	Size Distributions for Suspended Aerosols at $\sim 11000s$ for Reference Calculation (upper left), Nondefault Agglomeration Shape Factor (upper right), Nondefault Dynamic Shape Factor (lower left), and Default Shape Factors (lower right) - Shape Factors Sensitivity Study	58
7.1.1	Total and Steam Partial Pressures (top) and Atmosphere and Pool Temperatures (bottom) - Pool Condensation Sensitivity Study	60
7.1.2	Suspended Aerosol Masses - Pool Condensation Sensitivity Study	61
7.2.1	Pool Masses - HS Wall Initialization/Condensation Sensitivity Study	63
7.3.1	Total and Steam Partial Pressures - HS Radiation Sensitivity Study	65
7.3.2	Atmosphere and Pool Temperatures - HS Radiation Sensitivity Study	66
7.3.3	Suspended Aerosol Masses - HS Radiation Sensitivity Study	68
7.3.4	Saturation Ratio (top) and Water Aerosol Mass (bottom) - HS Radiation Sensitivity Study	69
7.3.5	Aerodynamic Mass Median Diameter (top) and Geometric Standard Deviation (bottom) for Suspended Aerosols - HS Radiation Sensitivity Study	70
7.3.6	Size Distributions at $\sim 11000s$ for Suspended Aerosols with (top) and without (bottom) Radiation - HS Radiation Sensitivity Study	71
7.4.1	Total and Steam Partial Pressures - Insulation Conductivity Sensitivity Study	73
7.4.2	Atmosphere and Pool Temperatures - Insulation Conductivity Sensitivity Study	74
7.4.3	Suspended Aerosol Masses - Insulation Conductivity Sensitivity Study	76

7.4.4	Saturation Ratio (top) and Water Aerosol Mass (bottom) - Insulation Conductivity Sensitivity Study	77
7.4.5	Aerodynamic Mass Median Diameter (top) and Geometric Standard Deviation (bottom) for Suspended Aerosols - Insulation Conductivity Sensitivity Study	78
7.4.6	Size Distributions for Suspended Aerosols at ~11000s with Increased (top) and Cited (bottom) Insulation Thermal Conductivities - Insulation Conductivity Sensitivity Study	79
8.1	Total Pressures - MELCOR/CONTAIN Comparison	82
8.2	Atmosphere Temperatures - MELCOR/CONTAIN Comparison	83
8.3	Suspended Aerosol Masses - MELCOR/CONTAIN Comparison	85
8.4	Saturation Ratio (top) and Water Aerosol Mass (bottom) for Suspended Aerosols - MELCOR/CONTAIN Comparison	86
8.5	Size Distributions for Suspended Aerosols at ~11000s for Reference Calculation (upper left), Default Agglomeration Shape Factor (lower left) and at ~10000s from CONTAIN (middle right) - MELCOR/CONTAIN Comparison	87

List of Tables

2.1	CSTF Containment Vessel Properties for Test LACE LA4	5
2.2	CSTF Containment Initial Conditions for Test LACE LA4	6
2.3	Thermal/Hydraulic Inputs Used for Test LACE LA4	7
2.4	Average Aerosol Injection Inputs for Test LACE LA4	8
4.2.1	PostTest Aerosol Locations - Final Reference Calculation Results . . .	29
5.2.1	PostTest Aerosol Locations - Time Step Sensitivity Study	40
6.1.1	PostTest Aerosol Locations - Aerosol "Washdown" Sensitivity Study .	42
6.2.1	PostTest Aerosol Locations - Multi-Component Sensitivity Study . . .	48
6.3.1	PostTest Aerosol Locations - Aerosol Size Distribution Resolution Sen- sitivity Study	50
6.4.1	PostTest Aerosol Locations - Shape Factors Sensitivity Study	57
7.1.1	PostTest Aerosol Locations - Pool Condensation Sensitivity Study . . .	62
7.3.1	PostTest Aerosol Locations - HS Radiation Sensitivity Study	72
7.4.1	PostTest Aerosol Locations - Insulation Thermal Conductivity Sensi- tivity Study	80

Acknowledgements

The author would like to acknowledge a number of individuals who contributed significantly to this report. Randy Cole and Russ Smith of the MELCOR development team helped with the thermal/hydraulic and aerosol portions of the problem, respectively; Russ in particular added a number of new output and plot variables which greatly aided the interpretation of the results. Sam Thompson provided input processing enhancements, the code on various platforms on demand, and friendly plot programs. Ken Washington, Ken Murata, Fred Gelbard and Jack Tills of the CONTAIN development program at Sandia provided the CONTAIN input and results used and the experimental data reports, as well as reviewing drafts of this report. Steve Webb, Ken Murata and Fred Gelbard helped interpret the aerosol results. Randy Summers and Steve Webb provided the final, formal review.

•
•

•
•

1 Introduction

MELCOR [1] is a fully-integrated, engineering-level computer code, being developed at Sandia National Laboratories for the U. S. Nuclear Regulatory Commission (USNRC), that models the progression of severe accidents in light water reactor nuclear power plants. The entire spectrum of severe accident phenomena, including reactor coolant system and containment thermal/hydraulic response, core heatup, degradation and relocation, and fission product release and transport, is treated in MELCOR in a unified framework for both boiling water reactors and pressurized water reactors. The MELCOR computer code has been developed to the point that it is now being successfully applied in severe accident analyses. Some limited technical assessment activities have been performed to date [2]; however, there is now a need to undertake a systematic program of verification and validation. To this end, a number of assessment calculations are being done as part of a quality control and technical assessment program, including some repeats of analyses done in the earlier assessment effort. One of the new assessment calculations specified was test LACE LA4, with results documented in this report.

The LWR Aerosol Containment Experiments (LACE) program [3] is a cooperative effort to investigate inherent aerosol behavior for postulated high consequence accident situations where the existing database is inadequate and which are not being addressed by other source term test projects. Accident situations being considered are those for which high consequences are presently calculated in risk assessment studies because either the containment is bypassed altogether, the containment function is impaired early in the accident, or delayed containment failure occurs simultaneously with a large fission-product release. A series of six large-scale experiments has been conducted at the Containment Systems Test Facility (CSTF) at Hanford Engineering Development Laboratory (HEDL).

The MELCOR code has been used to simulate LACE experiment LA4 [4,5,6]. The objective of test LA4 was to perform an integral aerosol behavior test simulating late containment failure with overlapping aerosol injection periods. In this test, the behavior of single- and double-component, hygroscopic and nonhygroscopic, aerosols in a condensing environment was monitored.

MELCOR version 1.81N was used for all the calculations whose results are shown in this report, although earlier calculations for this assessment exercise were done with MELCOR versions starting at 1.80O. MELCOR version 1.81N is the version that was released as MELCOR 1.8.1 in July 1991.

We have compared MELCOR results to experimental data, and to CONTAIN 7 calculations (see LACE LA4 [8]). Our MELCOR calculations were done as an open port to the data, with both the experimental data and the CONTAIN results available to provide guidance and feedback. The MELCOR LA4 analysis included all the models of three-step effects, wall and pool condensation, radiation heat transfer, and transport of aerosol components and reaction. Impact of non-default values of

shape factors and diameter limits in the aerosol input, and the degree to which plated aerosols adhere to the walls or are washed off by draining liquid condensate films.

•

•

•

•

2 Facility and Test Description

The experimental set-up for test LA4 is illustrated in Figure 2.1. The CSTF containment vessel is a 852m³ carbon steel vessel installed in a concrete pit. All interior surfaces are coated with a 0.51mm-thick modified phenolic paint layer, with a normal total emissivity of 0.9; exterior surfaces are covered with a 2.5cm-thick layer of fiberglass insulation with an outer aluminum vapor barrier. Additional details of the containment vessel are provided in Table 2.1. The initial containment conditions are summarized in Table 2.2.

The operation of the experiment was characterized by seven periods, as indicated in Table 2.3. (The steam injections specified in that table were saturated at the cited temperatures.) During the heatup portion of the test, steam was directed into the vessel in order to increase the vessel atmospheric temperature by $\sim 70\text{K}$. Following the heatup period, the first aerosol injected was CsOH, which is hygroscopic (water soluble). An insoluble aerosol, MnO, was injected with the CsOH for a portion of the aerosol injection period and continued to be injected after the CsOH injection was terminated. A quasi-steady-state period followed the aerosol injections. The vessel was then vented to the environment and allowed to cool down.

The containment vessel schematic in Figure 2.1 shows the various injection lines and the vent near the upper portion of the vessel. The lower steam line was used for injecting steam during vessel heatup and to provide a continuing source of steam (at a much slower injection rate) to maintain quasi-steady-state operation during periods 2 through 5. The injection line for the aerosols was located near the midplane of the vessel; steam and nitrogen were used as the carrier gas for the injected aerosols. Table 2.4 gives the average aerosol injection rates, together with the aerodynamic mass median diameter (AMMD) and geometric standard deviation (GSD) to be used for each injection species and period.

In addition to the sources summarized in Tables 2.3 and 2.4, additional heating of 2.00kW was provided to the vessel throughout most of the test, from -50 to 1707min. Also, a disconnected instrument water cooling line leaked 0.0243g/s of 15C water into the vessel between 450 and 1240min.

For general practice in the LACF project documentation to provide time stamps when displaying thermal/hydraulic data, and in seconds for the aerosol data, this same time stamp practice will be followed in this report to allow for direct comparison of LACF test results and data-code comparisons. (4.5.6.8)

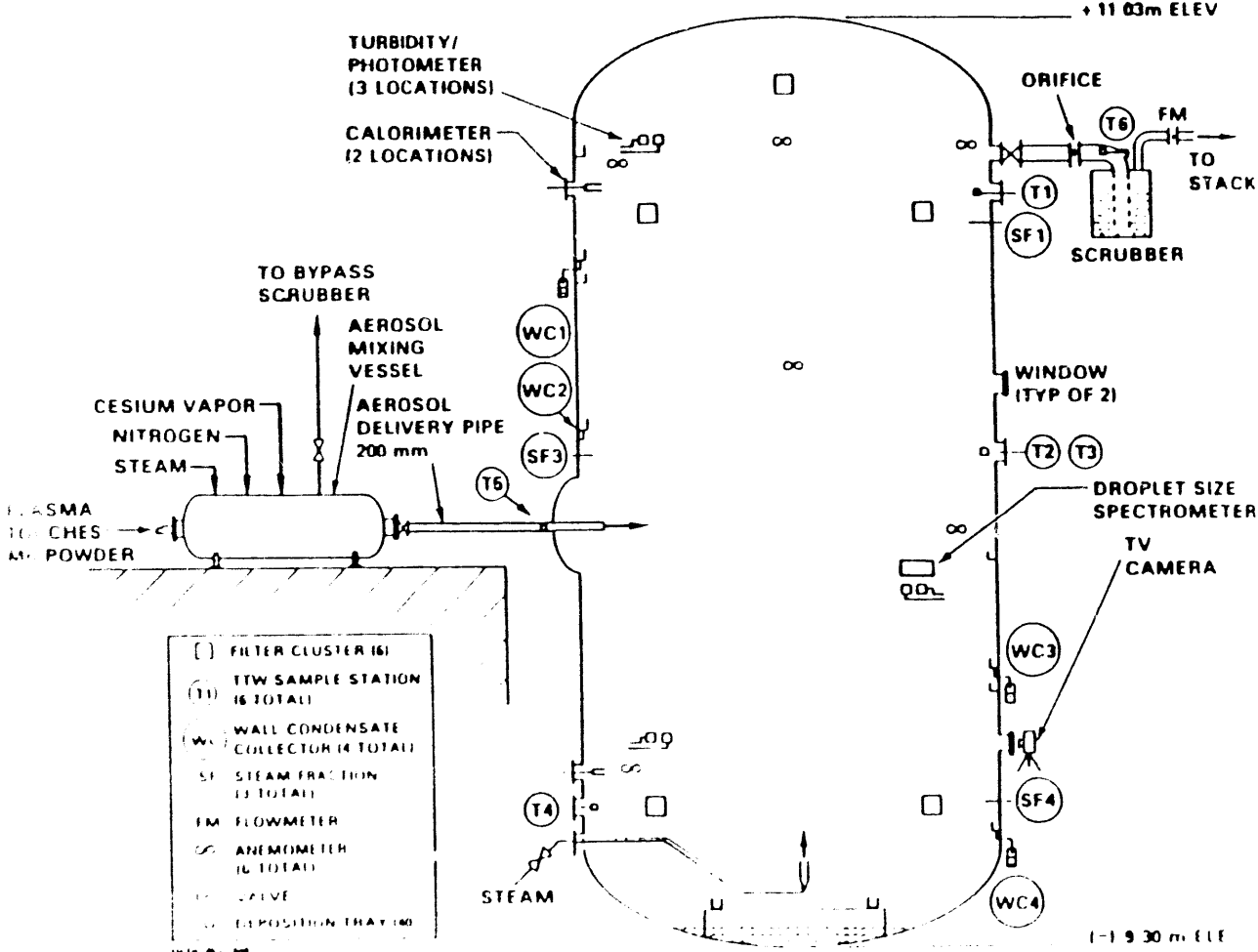


Figure 2.1. Schematic Diagram of the LACE OSTF Test Facility

Table 2.1. CSTF Containment Vessel Properties for Test LACE LA4

Dimensions	
Inside Diameter	7.62m
Total Height	20.3m
Cylinder Height	16.5m
Weight	
Top and Bottom Heads	9340kg each
Cylinder	51257kg
Penetrations and Plates	1720kg
Internals	14020kg
Heat Transfer Surface Areas	
Top and Bottom Heads	63m ² each
Cylinder	394m ²
Internals	221m ²
Total to Environment	520m ²
Heat Transfer Thicknesses	
Top and Bottom Heads	1.93cm each
Cylinder	1.69cm
Internals	0.825cm
Insulation	
Thermal Conductivity	0.0467W/m-K
Specific Heat Capacity	753J/kg-K
Density	96kg/m ³
Aerosol Settling Surface Areas	
Bottom Head	45.5m ²
Internals	42.3m ²
Aerosol Plating Surface Areas	
Vessel Shell	520m ²
Internals	221m ²
Vent Leak Path	
Orifice Diameter	3.40cm
Height above Vessel Bottom	16.5m
Secondary Flow Resistance	8kPa

Table 2.2. CSTF Containment Initial Conditions for Test LACE LA4

Parameter (at t=-50min)	
Pressure	107.0kPa
Average Gas Temperature	42.5C
Average Wall Temperature	42.5C
Average Water Temperature	41.9C
Sump Water Mass	950kg
Gas Composition	normal air
Volumetric Steam Fraction	0.0730
Aerosol Concentration	0
CV Lighting Power	2.69kW
Ambient Air Temperature	31.8C

Table 2.3. Thermal/Hydraulic Inputs Used for Test LACE LA4

Period	T_{start} (min)	T_{end} (min)	Material	Sources	
				Rate (g/s)	Temperature (C)
1 - Heatup	-50	0	steam	0.451	161
			nitrogen	0.0027	160
			nitrogen	0.0014	28
2 - CsOH Only	0	30.5	steam	0.029	167
			steam	0.019	237
			nitrogen	0.067	237
			helium	0.00059	237
			argon	0.00084	237
			nitrogen	0.0016	28
3 - CsOH+MnO	30.5	50.5	steam	0.029	167
			steam	0.019	253
			nitrogen	0.066	253
			helium	0.00059	253
			argon	0.00084	253
			nitrogen	0.0018	28
4 - MnO Only	50.5	80.2	steam	0.029	167
			steam	0.019	262
			nitrogen	0.067	262
			helium	0.00059	262
			argon	0.00084	262
			nitrogen	0.0020	28
5 - Steady State	80.2	280.0	steam	0.029	167
			nitrogen	0.0037	190
			nitrogen	0.0020	28
6 - Vent	280.0	600.0	steam	0.029	167
			nitrogen	0.0026	165
			nitrogen	0.0014	28
7 - Cool down	600.0	5700.0	nitrogen	0.0022	125
			nitrogen	0.0012	28

Table 2.4. Average Aerosol Injection Inputs for Test LACE LA4

Period	T_{start} (s)	T_{end} (s)	Aerosol	Sources		
				Rate (g s)	AMMD (μm)	GSD
2 - CsOH Only	0	1830	CsOH	0.949	1.35	1.81
3 - CsOH + MnO	1830	3030	CsOH	0.949	2.22	1.80
			MnO	0.757	2.43	1.70
4 - MnO Only	3030	4812	MnO	0.757	1.82	2.56

3 MELCOR Computer Model

Three control volumes (two representing environment), two flow paths and six heat structures (two sets of three representing the roof, cylinder and floor of the vessel and roof, vertical, and floor internals, respectively) are specified in the MELCOR model.

There is only one fully active control volume, representing the test vessel. Its volume-altitude table uses five entries to approximate the change in cross-sectional area with elevation in the elliptical lower head; this detail was needed to more correctly represent the sump pool liquid surface area as a function of pool depth or volume (important for steam condensation from the atmosphere, as discussed in Section 7.1).

A number of mass and/or energy sources are used to prescribe the steam, water and nitrogen injections into the test vessel, as well as the lighting. The argon and helium injections are neglected, because they are so small relative to the steam and nitrogen injections and to the vessel volume, and because neither was readily available as a built-in noncondensable gas with all required properties already in MELCOR. Because of the limitations on the total number of sources into a control volume in MELCOR (~35), those injections at different rates but at constant temperatures during several periods were sometimes combined into single mass/energy sources.

The two control volumes representing the environment, one used as the sink for the leak path opened during the vent period and as the heat structure boundary volume for the outside of the vessel, and the other used as the low-pressure boundary on the outside of the manual vent valve opened during the cooldown period, are both specified to be time-independent volumes, remaining constant at the initial thermal hydraulic conditions input. These time-specified volumes were initially set to very small volumes, which uncovered a MELCOR code error; the code reduced the heat transfer coefficient from the outside heat structures to the boundary volume to dampen expected temperature oscillations due to a small inertia, as would be done for a regular control volume. The problem was initially solved by increasing the volumes of the time-specified control volumes; since then, the code itself has been corrected.

Two flow paths are specified. One represents the leak path, and is a valve which simply opens and closes at specified times. The other models the manual vent valve, which opens when the test vessel pressure drops below the specified value and then remains open. Flow path length, area, and loss coefficients were taken from the CONTAIN input deck (9) when not available in the test reports at hand (5,6).

The six heat structures modelled can be divided into sets of three: one set represents the vessel shell while the other set represents internal structures. The vessel cylinder is modelled as a vertical cylinder with 14 nodes in the inner steel and 8 more in the surrounding fiberglass insulation. The elliptical upper and lower heads are modelled as flat, horizontal, rectangular structures with 7 nodes in the steel and 6 more in the fiberglass insulation. Six nodes were used in the all-steel "internal" heat structure. Most of the heat structure input data (*e.g.*, surface area, number and location of nodes, etc.) were taken from the CONTAIN input model (9).

The properties needed to model the fiberglass insulation were specified in the MELCOR deck. The density and specific heat were set to the published values. The cited thermal conductivity (given in Table 2.3) was increased to 0.10W/m-K to represent degradation of the insulation, as done in the CONTAIN analysis [8,9]. The effect of increasing that thermal conductivity is discussed in Section 7.4.

The three heat structures representing internals were specified to be adiabatic on one side, representing a symmetry condition. For all other boundary surfaces, "external" heat transfer coefficient correlations were used, with characteristic lengths set to either the height (for the walls) or the diameter of the cylinder (for the floor and roof). The critical pool and atmosphere fractions were set equal, to 1.0 for the roof and wall structures, and to 0.0 for the floor structures.

Radiation heat transfer between structure and control volume atmosphere was specified on all non-adiabatic surfaces, using the gray-gas model with an emissivity set to 0.9 and a radiation path length of 4.15m (both equal to corresponding input used in the CONTAIN model [9]). The importance of including radiation heat transfer was evaluated in Section 7.3.

The "floor" heat structures were input with $\cos\alpha = -1.0E-07$ to insure the proper structure orientation (180°), because we wanted to keep the left boundary as the inside boundary, adjacent to the test vessel, for all cases, and the left boundary by default ($\cos\alpha = 0$) is the "lowest" boundary for a rectangular, horizontal heat structure.

In the reference model, the temperatures in all steel heat structure nodes in the vessel cylinder were set equal to the initial inside wall temperature, and the temperatures in all the fiberglass insulation heat structure nodes were set equal to the initial outside wall temperature. The heat structures representing internal structure were specified to self-initialize. A sensitivity study is described in Section 7.2 in which the steady state initialization option was used for the temperature distributions in all heat structures.

The reference calculation discussed in detail in Section 4 used two aerosol components, one for the water and the other for the two injected aerosol species, with twenty sections or size bins in the aerosol mass distribution. Sections 6.2 and 6.3 present results obtained using different RMI package input. One variation tried direct single aerosol component for both the water and both injected aerosols (the MELCOR default), or three separate aerosol components, one each for H_2O , COH and MnO . Another study reduced the number of sections to 10 and then to 5 (the default).

The minimum and maximum diameters for the size distribution were 0.1 and 250 μm , respectively, values taken from the CONTAIN input [9]. One sensitivity study calculation was run in which the default MELCOR values of 1 and 50 μm were used (as given in Section 6.1). Using those default limits precluded using 20 size sections because of the default MAEROS requirement that the ratio of the upper to lower diameters, for each section, be ≤ 2 , so 10 sections were used in this study.

The aerosol particle density was specified as 2195kg/m^3 and the dynamic shape factor to be 1.85, both from the CONTAIN input. The agglomeration shape factor was set to 2.25, from the MELCOR and CONTAIN ABCOVE input [2]. A sensitivity study was done in which either or both the dynamic and agglomeration shape factors were reset to their default value in MELCOR of 1.0, with results also discussed in Section 6.4. The pressures and temperatures for the aerosol coefficient calculation were reset to better represent the experimental conditions. All other RN1 aerosol input was left as default, except that all the extra, optional RN1 printed output (giving additional component, section and class information on deposited, gas and liquid aerosol masses) was activated.

The aerosol sources were modelled by specifying average, lognormal source rates into the vessel control volume as indicated in Table 2.4. Two sources were used for each injected species, one during its “solo” injection and another during the combined injection period, to allow input of the different aerodynamic mass median diameters (AMMDs) and geometric standard deviations (GSDs) specified during those periods. (The CONTAIN model [9] used the actual aerosol sources; using those sources in this MELCOR analysis would have required manually processing and inputting input tables with hundreds of points, because the data was not available to us in a convenient electronic form.)

A special code mod was used with version 1.8HN to add the AMMD and GSD of each aerosol component, together with composite “dry” and “wet” values, to the plot file. These extra plot variables will be added to the production code soon.

The reference analysis was run with a maximum time step of 60s (1min) during the heatup, aerosol injections and steady-state periods, and a maximum time step of 600s (10min) during the cooldown period, with an intermediate maximum time step of 150s (2.5min) during the vent period. The code ran at the maximum allowed time step throughout. The results of a time step sensitivity study are given in Section 5.

A copy of the MELGEN MELCOR input used for the the reference calculation is given in the appendix, for reference.

•
•

,

•
•

4 Final Reference Calculation Results

The MELCOR LACE LA4 assessment analysis was done as open post-test calculations, with both the experimental data and results from previous CONTAIN analyses available for reference. The MELCOR results discussed in detail in this section represent our final, best, calculation, taking full advantage of experience and insight gained from the sensitivity studies reported in Sections 6 and 7, and from the CONTAIN analyses.

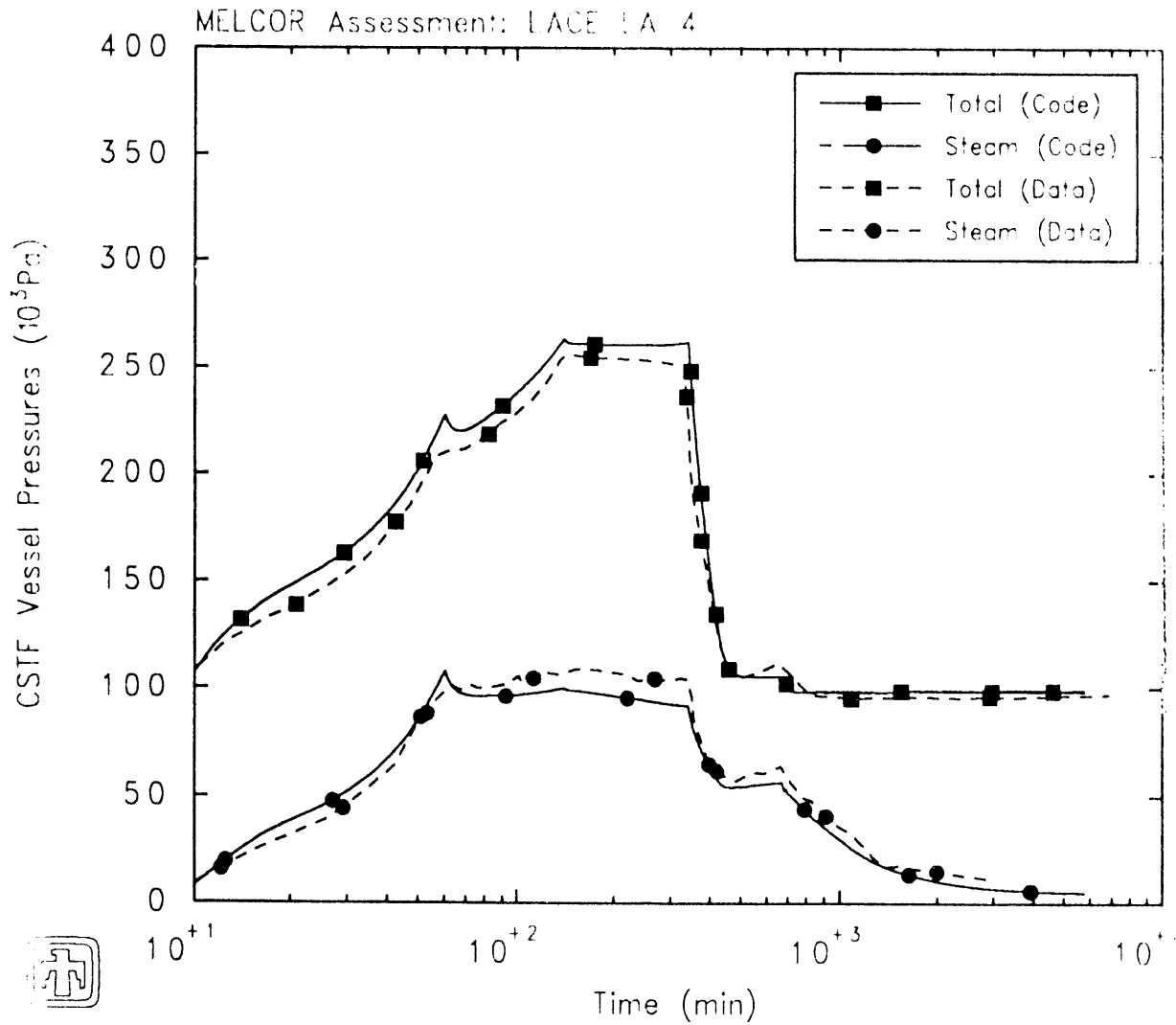
As mentioned at the end of Section 2, it is general practice in the LACE project documentation to present time in minutes when displaying thermal hydraulic data, and in seconds for the aerosol data. This (nonstandard) practice will be followed in this report to allow easy referral to other published LACE test results and data-code comparisons [4,5,6,8]. For the thermal hydraulic results plots, the time domain is transformed further by adding 60min to the test reference times (used in Tables 2.3 and 2.4) so that all time points can be displayed on a single logarithmic scale. In this time domain, the first (heatup) period begins at 10min and the aerosol injection periods occur from 60min to 140.2min.

4.1 Thermal/Hydraulic Response

Comparison of measured and calculated total and steam pressures in the building atmosphere are presented in Figure 4.1.1. The total pressure measured is considered accurate to $\pm 2\%$; the observed steam pressure given is a volumetric average of measurements at three locations, and has an expected accuracy of $\pm 10\%$ [5].

A significant pressurization was both predicted and observed to occur during the heatup and aerosol injection periods, with the predicted peak pressure of 260kPa slightly higher than the measured peak of 250kPa. The calculated pressures show a local peak and subsequent dip at ~ 50 -60min, not seen in the test data, although the observed change in pressurization rate is predicted correctly. The analysis is in excellent agreement with data during the venting and cooldown periods.

While the total pressure in the containment vessel is overpredicted during the heatup, aerosol injection and steady-state periods, the steam pressure is underpredicted during the steady-state period (110-340min), by amounts similar in magnitude to the quoted data uncertainty. The steam pressure depends on the steam injection and leak rates, and on the condensation and evaporation processes involving the building structures, pool and bulk vapor region (discussed in more detail below). Because of these multiple dependencies, it is difficult to determine exactly why the calculated steady-state steam pressure is dropping slightly below the test data. Uncertainty and misprediction of the steam pressure is important in this and similar situations because of the dependence of aerosol behavior on steam concentrations.



CE LA-4 (2-component)
 BJRZ 30JUL91 09:52:58 MELCOR

Figure 4.1.1. Total and Steam Partial Pressures - Final Reference Results

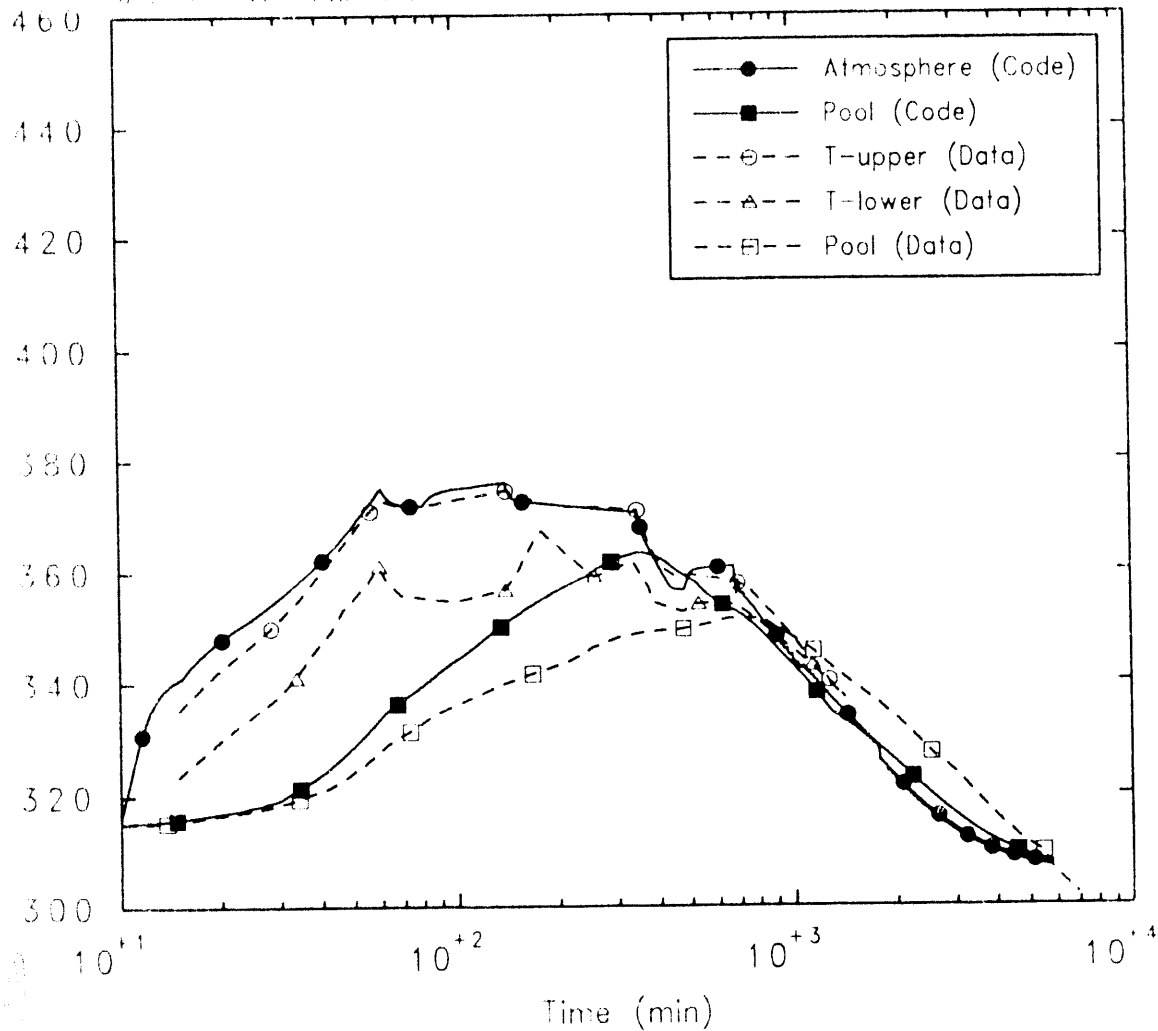
Figure 4.1.2 gives comparisons of measured and calculated bulk (atmosphere) and pool temperatures in the containment vessel. Two distinct regions, or convection cells, were observed in this experiment. The upper region or cell was characterized by relatively uniform temperatures and included all the volume above the elevation of the steam outlet pipe, or about 95% of the total volume; the lower region, 5% of the total volume, was characterized by temperatures that decreased nearly linearly from the upper region temperature to the temperature of the pool in the bottom. Measured temperatures representative of both the lower and upper regions are shown, which are based on volume-weighted averages of multiple thermocouples, with expected accuracies of $<1\text{K}$. The pool was circulated with an external pump to minimize spatial pool temperature variations, so the expected accuracy of the thermocouples in the pool was cited as $<2\text{K}$.

While measured temperatures representative of both atmosphere regions are shown, the single-control-volume MELCOR model should be compared to the observed upper-region bulk temperature. Because most of the calculation is at or near saturation, the same quantitative and qualitative features are expected to occur in both the steam pressure and the bulk temperature comparisons. The calculated pool temperatures are in very good agreement with data during the early (heatup) and late (cooldown) periods, but the pool temperature is significantly higher than observed during the aerosol injection and steady-state periods. This overprediction is most likely due to the pool in this single-volume model being in direct contact with the bulk temperature characteristic of the upper convection cell rather than the $\sim 10\text{K}$ lower bulk temperature actually observed just above the pool in the containment vessel.

A comparison of calculated and measured total liquid mass in the pool (sump) is shown in Figure 4.1.3. Instrumentation problems and unexpected water leakage from an instrument cooling line required adjusting and smoothing of the pool mass data which might degrade the expected accuracy of $\pm 5\%$. Agreement between code and experiment is very good in all time periods. Before about 500min, the increase in pool mass is solely due to condensation on the pool surface and to condensation on and draining off structures; the leakage accounts for most of the increase in pool mass after that time, until about 1300min, after which the pool mass remains nearly constant. The apparent time delay in predicted initial increase in pool mass represents the time needed to build up a film on structures before condensate begins to run off into the pool (discussed more in Section 6.2).

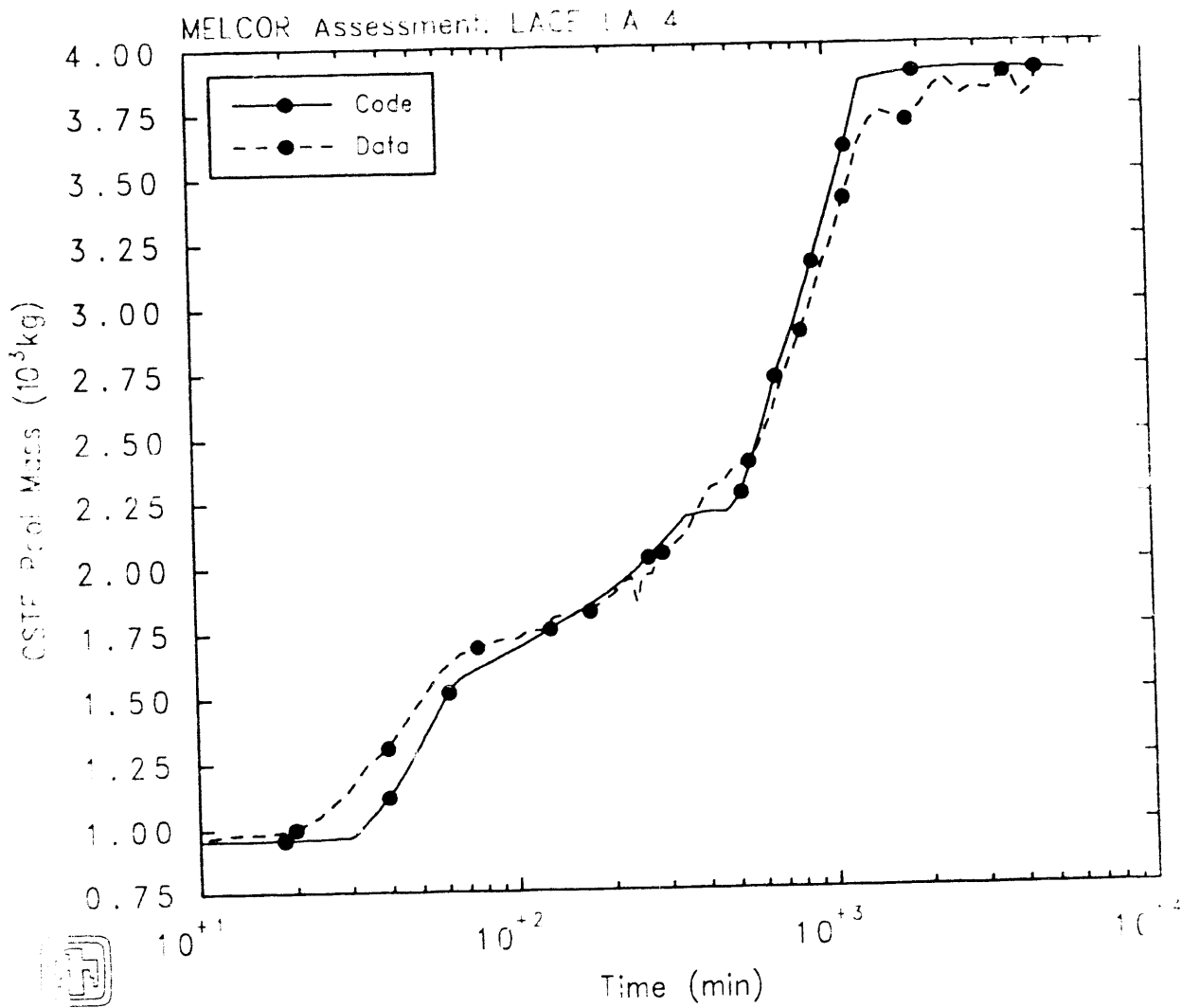
Figure 4.1.4 shows a comparison of the measured and calculated condensation mass fluxes on the vessel walls. Experimental data were taken from condensate collectors at four locations, with a quoted data accuracy of $\pm 20\%$. Calculated results are shown for both the inside surface of the containment vessel and for the surfaces of the internal structures modelled; substantial condensation mass fluxes are seen only on the vessel walls after the initial heatup and early aerosol injection period. The qualitative agreement of MELCOR with data is excellent, and the quantitative agreement is quite good, given that the data measured localized condensation rates

4.1.1.0% Assessment: IAG-1A-4



4.1.1.0% (2 component)
REF: 5001.91 03.52.58 MICOR

Figure 4.1.2. Atmosphere and Pool Temperature - Final Reference Results



DE LA-4 (2-component)

PERZ 30 JUL 91 09:52:58 MELCOR

Figure 4.1.3. Pool Masses - Final Reference Results

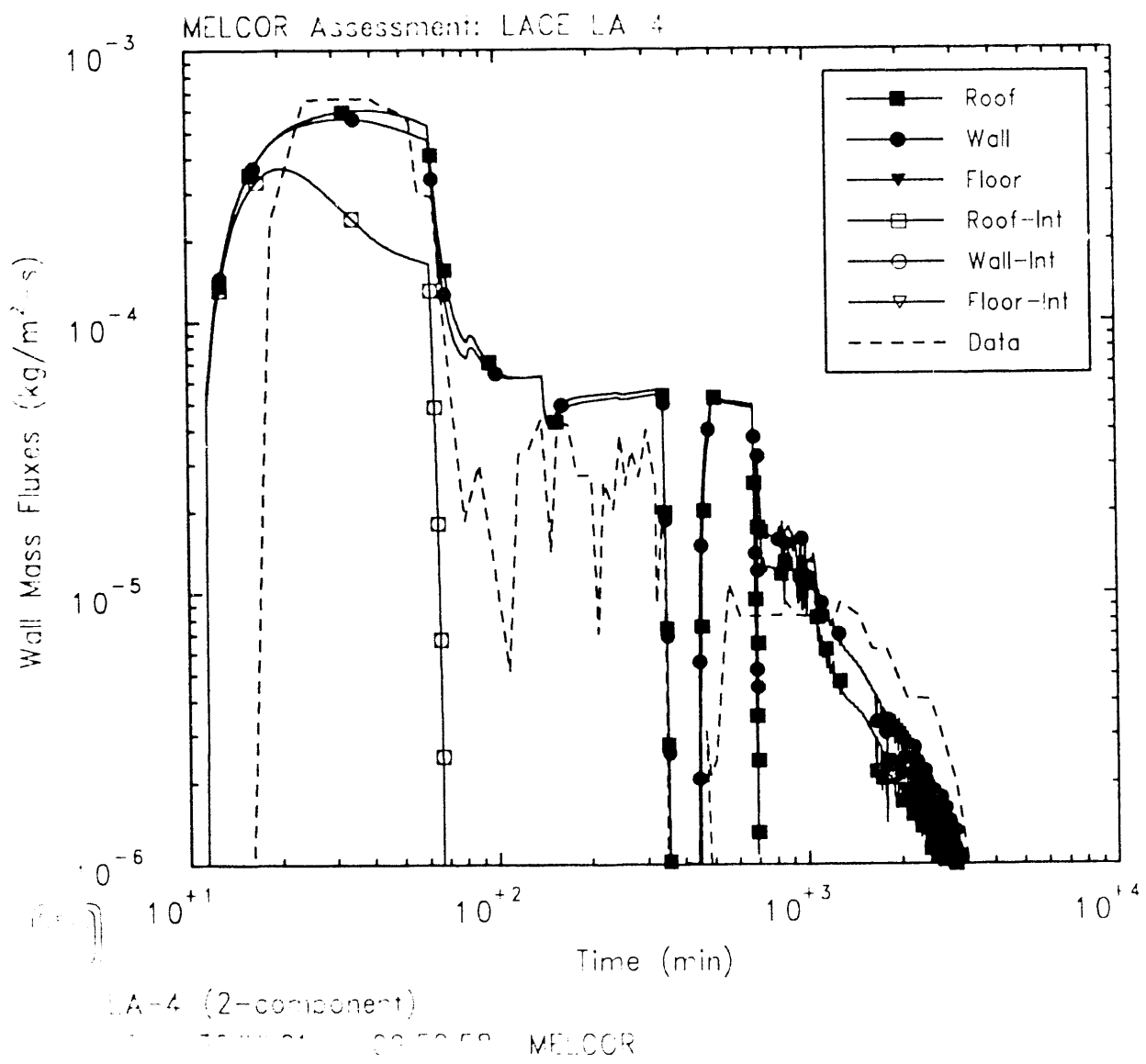


Figure 4.1.4. Condensation Mass Fluxes - Final Reference Results

while the code result represents a surface average. The substantial decrease in condensation from the walls during the venting period is correctly predicted, followed by increased condensation following depressurization of the containment vessel.

Comparisons of calculated and measured wall temperatures are illustrated in Figure 4.1.5, for the inside wall surface (top plot), the “middle” interface or the outside of the steel shell but inside the vessel thermal insulation (middle plot), and the outside insulation surface (bottom plot). The expected experimental accuracy in all cases is better than $\pm 3\text{K}$. Calculated results are given for all the heat structures modelled, although the data are for locations in the upper vessel.

The temperatures of the vessel roof and sides (the heat structures in contact with the atmosphere) on both sides of the steel shell are in excellent agreement with the test data; because of the high thermal conductivity of steel, the outside surface temperatures of the steel shell were very similar in magnitude to the inside surface temperature of the steel. Thus, the energy predicted to be stored in the steel vessel structure should be in excellent agreement with experiment.

Because of the large thermal resistance of the insulation on the vessel, the outside insulation surface temperature is largely dependent on the heat transfer between the insulation and the air outside the containment vessel, and does not have significant influence on the behavior inside the containment. MELCOR overpredicts the outside surface temperature by as much as 10K throughout most of the problem time, greatest during the steady-state period. The laminar natural circulation used in MELCOR could be too low for this situation; however, the discrepancy could just as likely be due to large uncertainties in the condition and modelling of the insulation, instead.

Figure 4.1.6 compares observed and predicted leak flows. The measured leak flows were based on ΔP measurements across a flow limiting orifice in the leak path, with an expected accuracy of $\pm 5\%$. The calculated leak mass flow is generally consistent with data in both magnitude and trend.

4.2 Aerosol Behavior

Calculated and experimental aerosol concentrations in the containment vessel are plotted in Figures 4.2.1 and 4.2.2, crossplotted for both aerosols injected and for each aerosol species (CsOH and MnO) separately, respectively. (The cited experimental uncertainties, different at different times, are shown as error bars on the data curve.) The individual aerosol species concentrations in Figure 4.2.2 have been plotted on a scale selected to highlight the behavior during the injection, steady-state and venting periods, which is of more interest than the very late-time, cooldown period, response; Figure 4.2.1 uses an ordinate scale that shows the predicted and measured concentrations throughout the experiment.

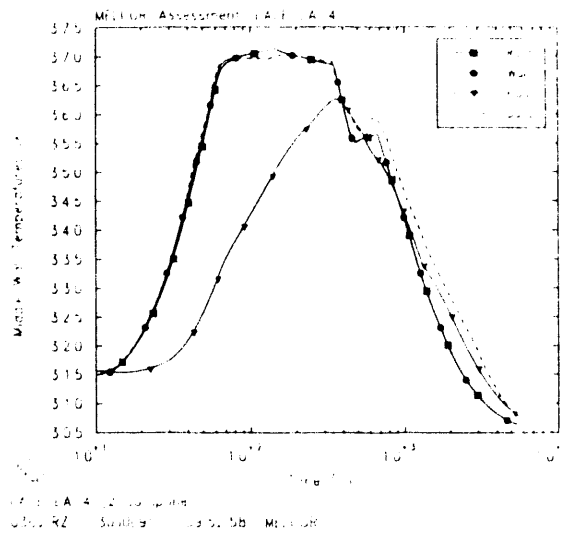
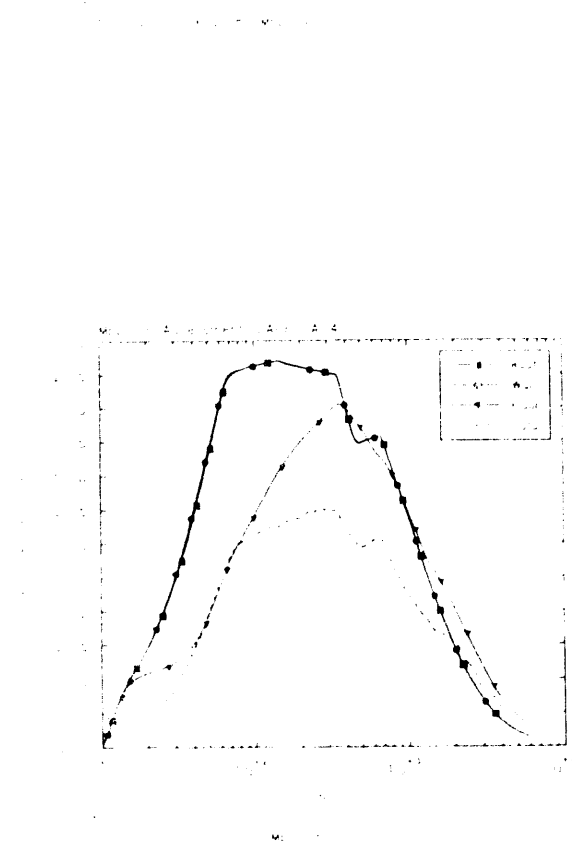
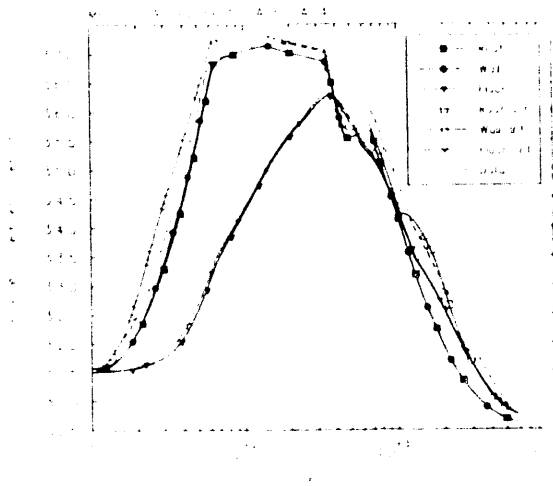


Figure 4.1.5 Inside (top), Interface (middle) and Outside (bottom) Wall Temperature - Final Reference Result

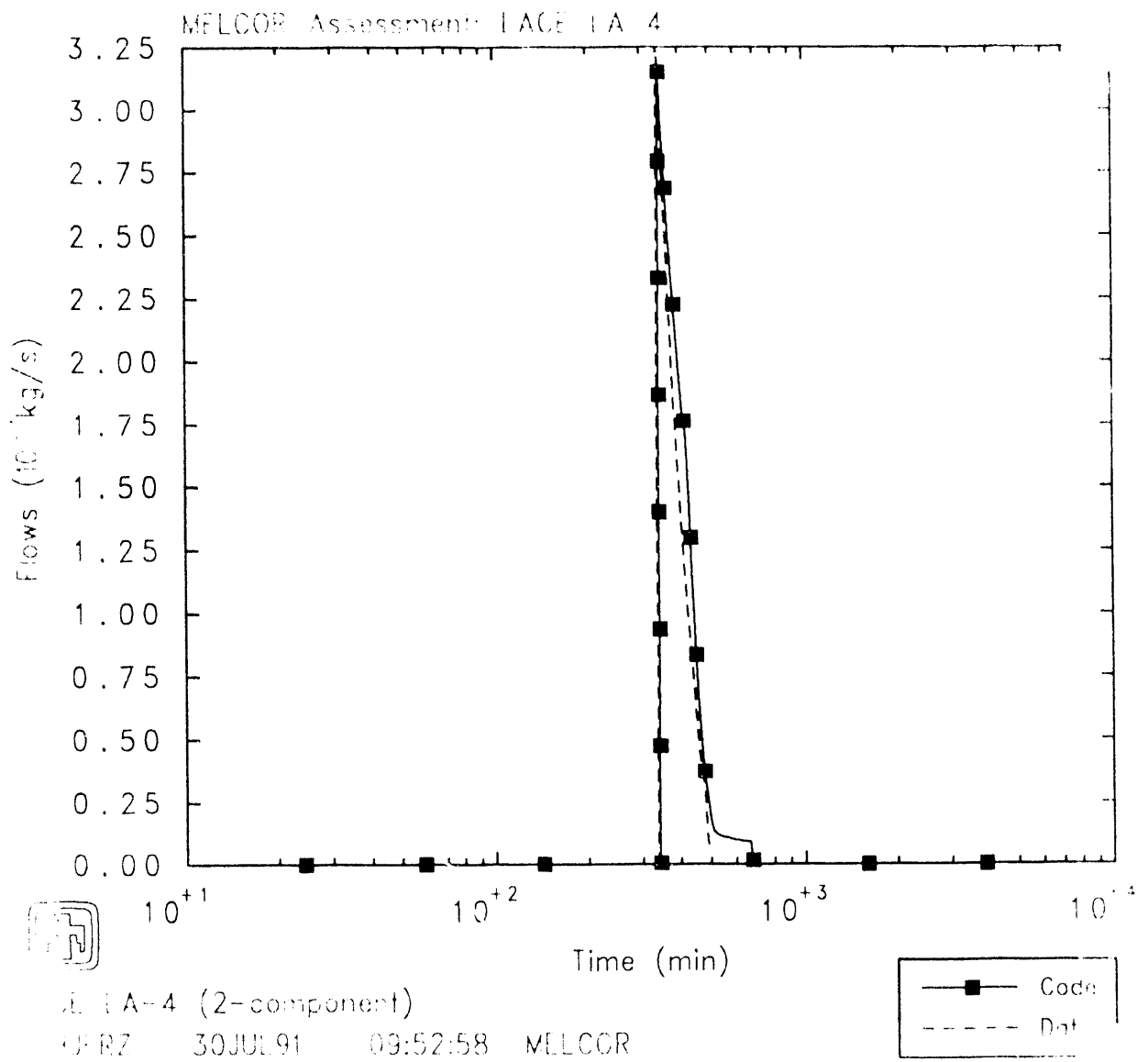
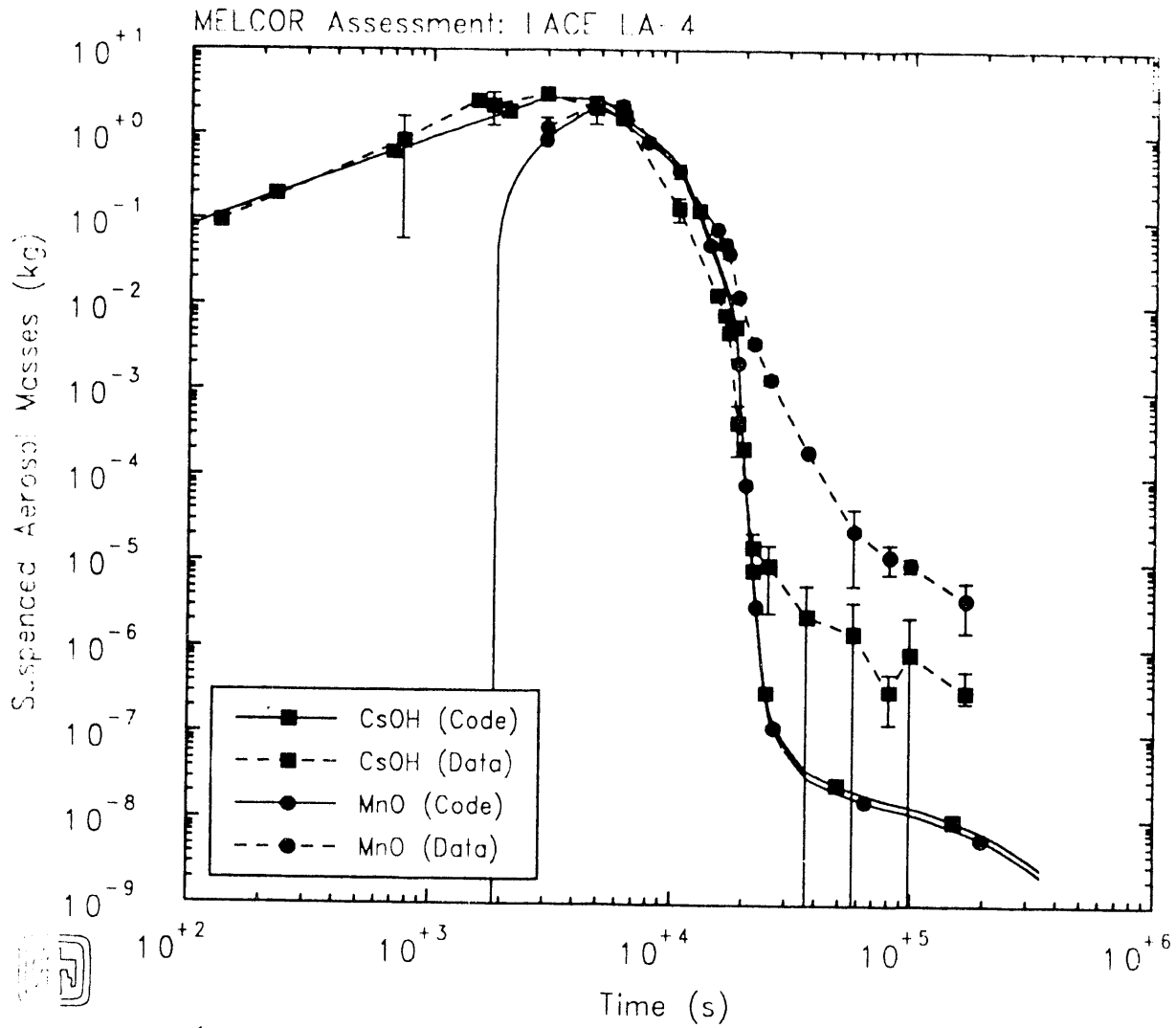


Figure 4.1.6. Leakage Mass Flow Rates - Final Reference Results



E LA-4 (2-component)

ERZ 30JUL91 09:52:58 MELCOR

Figure 4.2.1. Suspended Aerosol Masses Final Reference Results

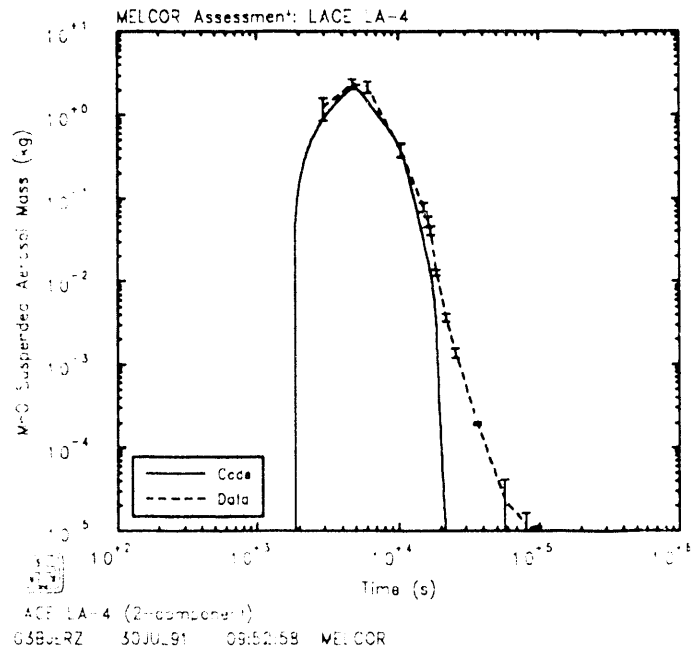
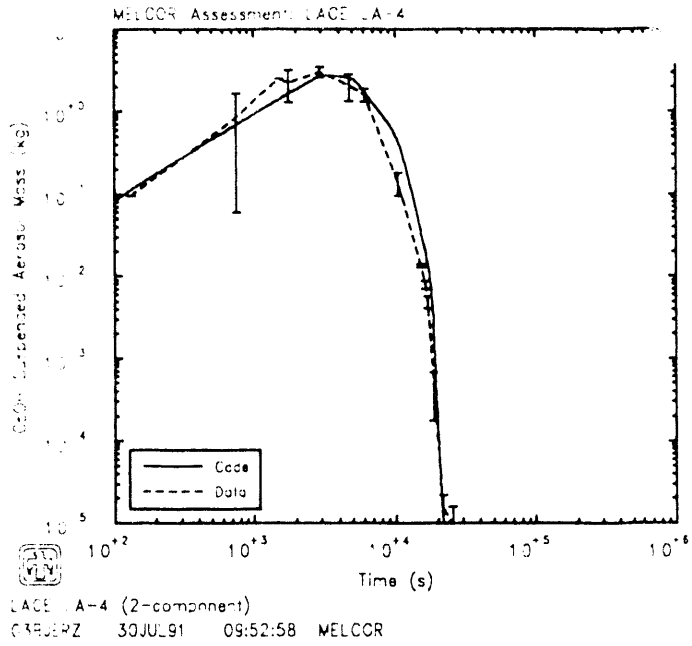


Figure 4.2.2. CsOH (top) and MnO (bottom) Suspended Aerosol Masses - Final Reference Results

For each aerosol species and for the combined aerosols, the agreement between measurement and calculation is very good during the aerosol source periods (to 1812s); after all aerosol injection terminates, MELCOR slightly overpredicts the CsOH suspended aerosol concentration and slightly underpredicts the MnO concentration during the steady-state period, and then underpredicts the suspended aerosol concentrations by several orders of magnitude during the late vent and cooldown periods (especially for the CsOH).

There is no significant variation between the predicted behaviors of the two aerosol species in this calculation (or any of our calculations, even when the CsOH and MnO are modelled as separate aerosol components, as will be shown in sensitivity study results in Section 6.2). This is qualitatively different from the test data where the suspended mass of the nonhygroscopic MnO is greater than the suspended mass of the hygroscopic CsOH during the later steady-state, vent and cooldown periods. This qualitative difference between analysis and test data reflects the lack of any hygroscopic effects in the MELCOR aerosol treatment.

Figure 4.2.3 presents the calculated saturation ratio, *i.e.*, the ratio of the partial pressure of water vapor in the atmosphere to the saturation pressure of water vapor at the atmosphere temperature, and the water aerosol mass suspended in the test vessel atmosphere. (During the course of this calculation, we checked and verified that the suspended water aerosol mass in the RN1 package was identically equal to the water droplet or “fog” mass in the control volume atmosphere in the CVH package.) Note that the amount of liquid water aerosol in the atmosphere, at about 1-10kg, is quite small compared to the amount of liquid water condensing on the sump pool surface and on the containment vessel walls (about 1000kg).

When the atmosphere is fully saturated, *i.e.*, a saturation ratio of 1, as during the steady-state period and the first part of the vent period, the suspended aerosol particles are growing as water condenses onto them; the larger aerosol particles then tend to settle out more quickly. The calculated suspended aerosol masses for both CsOH and MnO in Figures 4.2.1 and 4.2.2 peak when the atmosphere first shifts from subsaturated to saturated conditions, at ~5000s, and then decline while the atmosphere remains saturated, until about 25000s. In contrast, when the atmosphere is subsaturated, *i.e.*, a saturation ratio < 1, the aerosol particles will tend to dry out as water is pulled off them back into the atmosphere, reducing the size of the suspended aerosol particles and enabling them to remain suspended longer. Thus, when the atmosphere becomes subsaturated again, at about 25000s, the suspended aerosol masses in Figure 4.2.2 level out as the settling-out rate slows.

The aerodynamic mass median diameter AMMD (*i.e.*, the diameter below which 50% of the mass of the particle size distribution lies), and the geometric standard deviation GSD (*i.e.*, most simply, assuming a lognormal distribution, the ratio of the diameter at 84.13% cumulative mass to the mass median diameter) predicted in this calculation are compared to values derived from experimental observations (6 in Figure 4.2.4). Note that the time scale used has been restricted to highlight the behavior

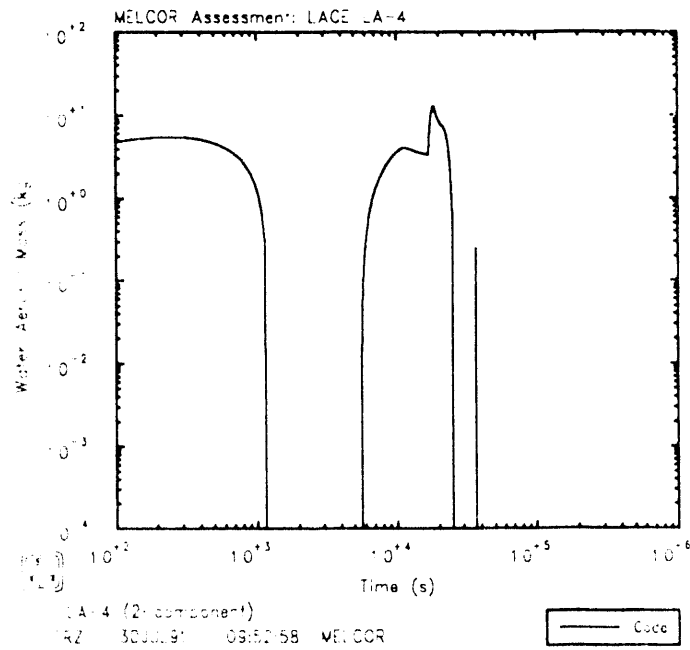
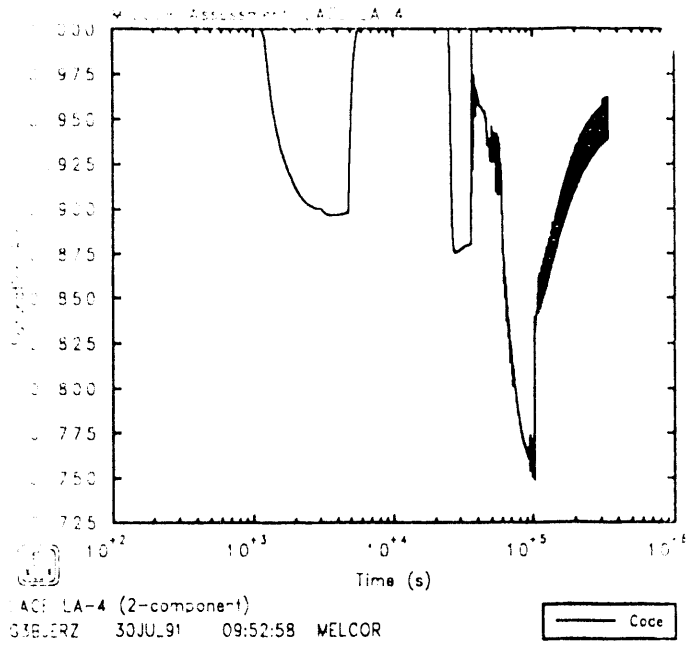


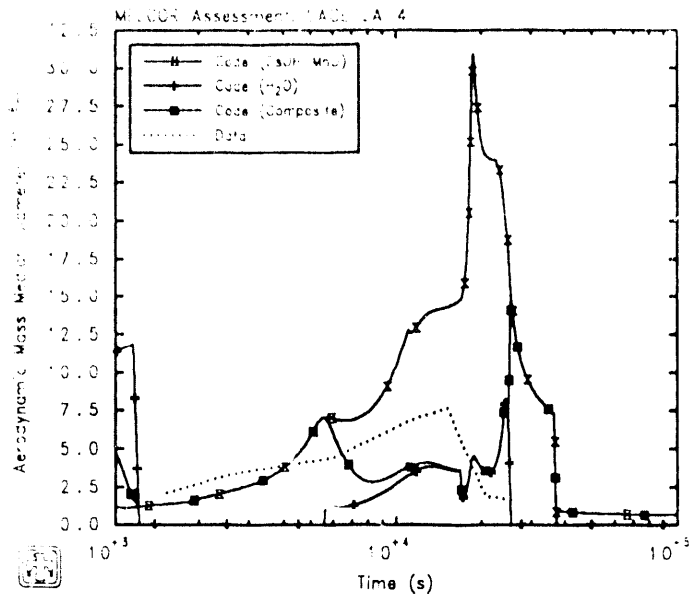
Figure 4.2.3. Saturation Ratio (top) and Water Aerosol Mass (bottom) for Suspended Aerosols – Final Reference Results

predicted during the steady-state and vent periods. Code results are given separately for each of the two aerosol component size distributions (one for the two injected aerosol species and the other for any water present) as well as for a composite distribution; for the two-component aerosol model used, whenever no water is present, that composite distribution simply reduces identically to the injected-aerosols distribution. The predicted AMMD is somewhat larger in general than measured, but peaks at about the same time; the GSD from the calculation indicates an aerosol size mass distribution similar to data.

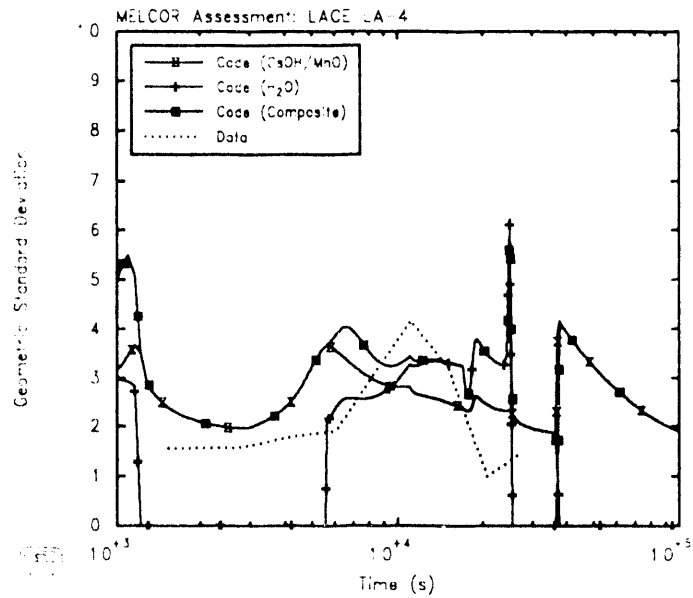
Figure 4.2.5 shows the aerosol masses in each of the twenty sections used in this calculation, at two different times. The total aerosol particle mass in each section, or size class, is given by the uppermost horizontal line over the particle diameter range of that section, while the relative fractions of the shaded regions represent the relative mass concentrations of the three aerosol species (CsOH, MnO and H₂O). The upper figure shows the suspended aerosol size distribution at ~4400s, near the end of the aerosol injection period and near the time of peak suspended aerosol mass. The atmosphere is subsaturated at this time, as discussed above, and no water is present in the aerosol. Later, at ~11000s in the lower figure, when the atmosphere is saturated, water condenses onto the aerosol particles and that water vapor condensation results in a shift of the CsOH and MnO to larger particle sizes (which, as mentioned already, increases the rate of aerosol removal by settling). Condensation onto aerosols is rate-limited in MELCOR and any excess water aerosol particles are assumed to be put initially into the smallest size bin, shifting the water aerosol component size distribution in this two-component aerosol model to smaller sizes.

The final disposition of the injected aerosols is presented, with corresponding test data, in Table 4.2.1, for each aerosol species and for the total. The code correctly predicts that the majority of the aerosol injection remains in the vessel, settled to the floor. In the experiment, the settled aerosols are observed on the bottom of the vessel some time after the end of the transient, when the vessel is opened for inspection. In the calculation, the settled aerosols are suspended in the sump water pool at the end of the transient, rather than deposited on the horizontal, "floor", heat structures; it is assumed in MELCOR, however, that when pool liquid finally disappears the suspended aerosols in the liquid settle down.

The total aerosol mass leaked to containment is much smaller than that measured, and the difference in relative amounts of the two species leaked is not predicted. The greater amount of MnO aerosol leaked in the experiment is likely due to the greater amount of MnO aerosol suspended in the vessel atmosphere later in the problem, during the venting and cooldown periods; the lower than measured, approximately equal, amounts of aerosols predicted to be leaked in the analysis would then be due to the lower, approximately equal, amounts of both aerosols calculated to be suspended in the vessel atmosphere during those late problem periods.



LACE LA-4 (2-component)
G3B:ERZ 30JUL91 09:52:58 MELCOR



LACE LA-4 (2-component)
G3B:ERZ 30JUL91 09:52:58 MELCOR

Figure 4.2.4. Aerodynamic Mass Median Diameter (top) and Geometric Standard Deviation (bottom) for Suspended Aerosols – Final Reference Results

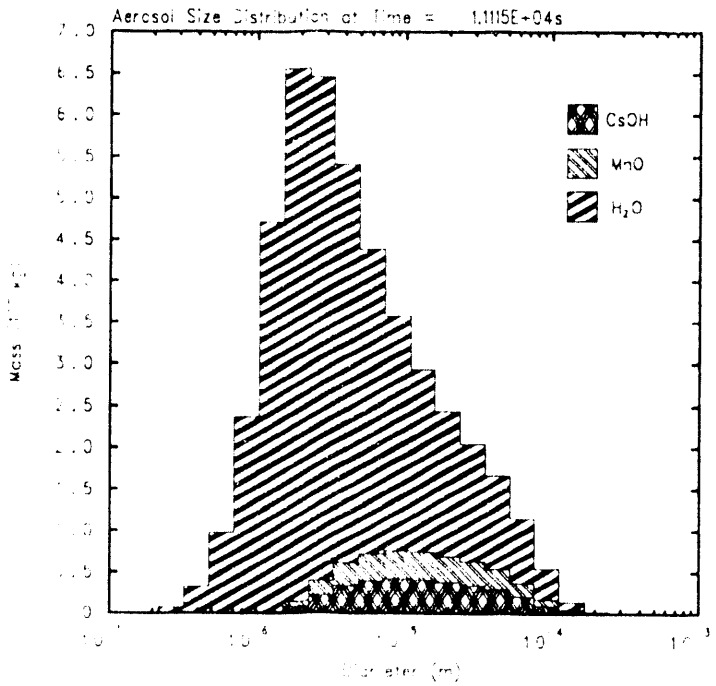
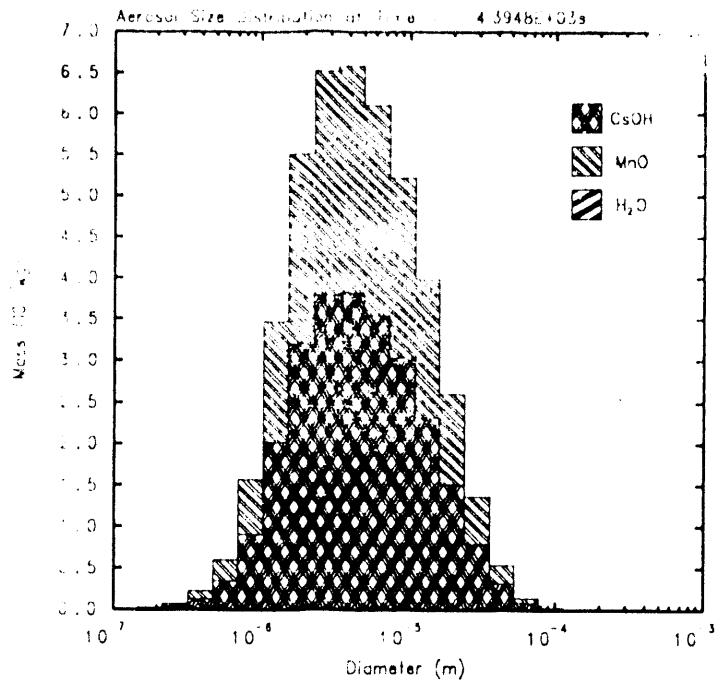


Figure 4.2.5. Size Distributions at ~1100 (top) and ~11000s (bottom) for Suspended Aerosols – Final Reference Results

Table 4.2.1. PostTest Aerosol Locations - Final Reference Calculation Results

Aerosol Species	Location	Test Data (kg)	Code (kg)
CsOH	Settled	2.563	2.615
	Plated	0.304	0.230
	Leaked	0.007	0.002
MnO	Settled	1.927	2.153
	Plated	0.228	0.117
	Leaked	0.101	0.001
Sum	Settled	4.490	4.768
	Plated	0.532	0.347
	Leaked	0.108	0.003

MELCOR also underpredicts the plated aerosol masses, both individual and total. The CsOH and MnO plated masses in this calculation are 24% and 48% lower than test data, respectively. As discussed in Section 6.1, the agreement between measured and calculated plated masses is much worse with the “normal”, default, code, which assumes that plated aerosols are washed off the horizontal “roof” and vertical “wall” heat structures with thick condensation films draining down into the liquid pool. In this reference, best, calculation we suppressed such aerosol “washing-off” by draining water films through a new sensitivity coefficient.

•

•

•

•

5 Time Step Effects and Machine Dependency

There has been a lot of discussion recently on numeric effects seen in some MELCOR calculations, producing either differences in results for the same input on different machines or differences in results when the time step used is varied. Several calculations were done to identify whether any such effects could be observed in our LACE LA4 assessment analyses.

5.1 Machine Dependencies

The calculation discussed in detail in Section 4 was run on a SUN Sparc2 workstation, on a VAX 8650, and on a CRAY XMP-24. The results from the three machines (for the three otherwise-identical runs) were different in some significant digits in the printed output, but when crossplotted all curves examined overlay well enough that no differences were visible.

Figure 5.1.1 shows the total vessel pressures and steam partial pressures for the same calculations on the three different machines, together with the test data. There are no visible differences in results. (Crossplots for the atmosphere and pool temperatures and for the pool liquid mass (not shown here) show the same degree of agreement.)

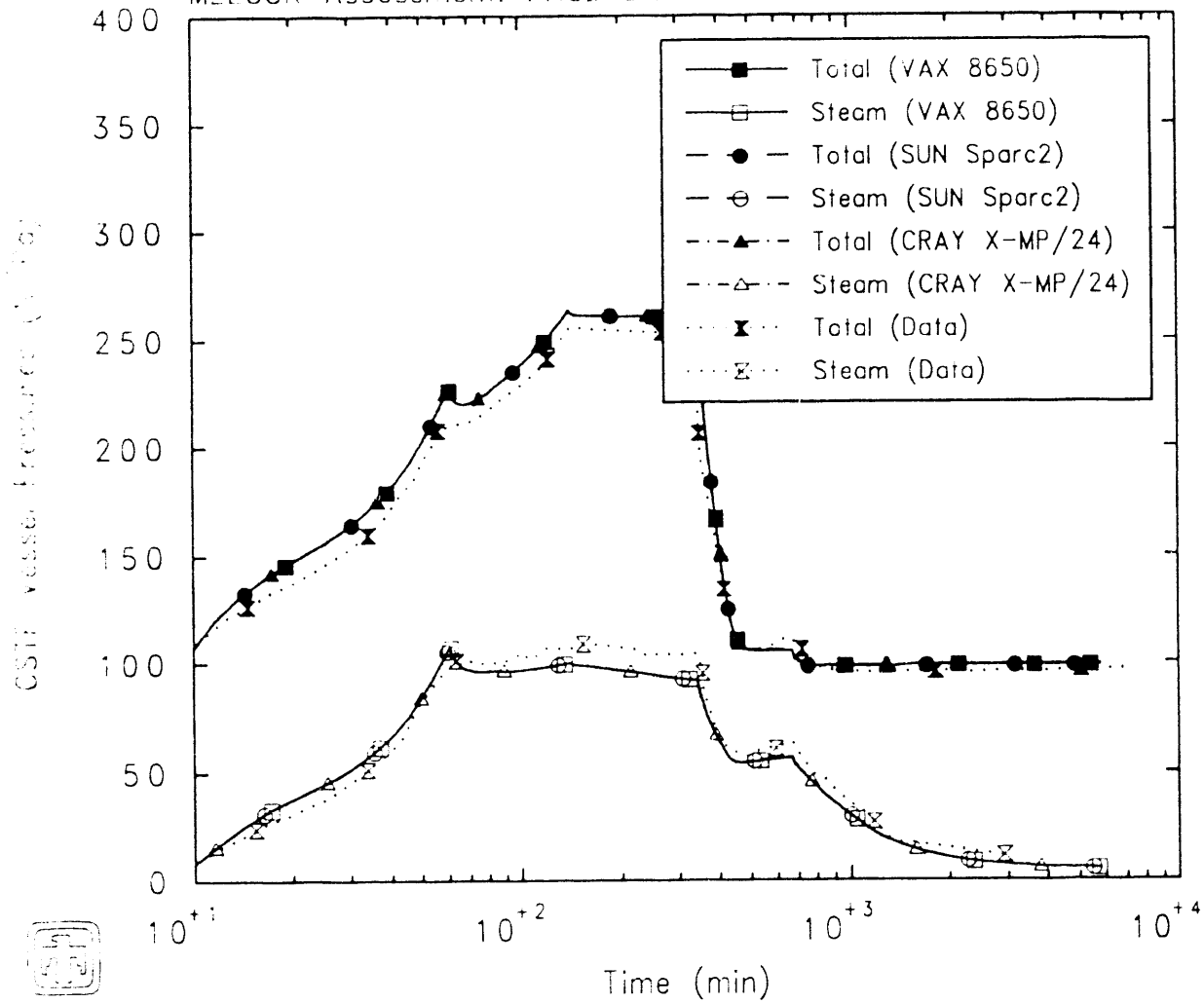
The suspended aerosol masses calculated on these three machines are compared to each other, and to measurements, in Figure 5.1.2. There is a small difference visible late in the cooldown period, when the aerosol masses are very small, but in general there are no significant machine-to-machine differences. (The final aerosol dispositions were identical in all digits shown in Table 4.2.1 on these two machines.)

Figure 5.1.3 shows the total run times for the reference calculation on the three machines (in the upper plot), together with the run times required by the different MELCOR packages active in this problem (in the lower plot, for the VAX 8650. The fraction of time taken by the individual packages is the same on all three machines; the results for the individual packages are not crossplotted in this case, because there would be too many curves for legibility. The run times on any of the machines are directly related to the maximum time step allowed, as discussed in the next section, and the effect of increasing the maximum allowed time step (used throughout) is clearly visible later in the problem time. This problem ran somewhat slower on the VAX than on the SUN, but the 25-30% difference in run time is not very significant; the CRAY was faster, but by a factor of 10, because MELCOR is not vectorized.

5.2 Time Step Effects

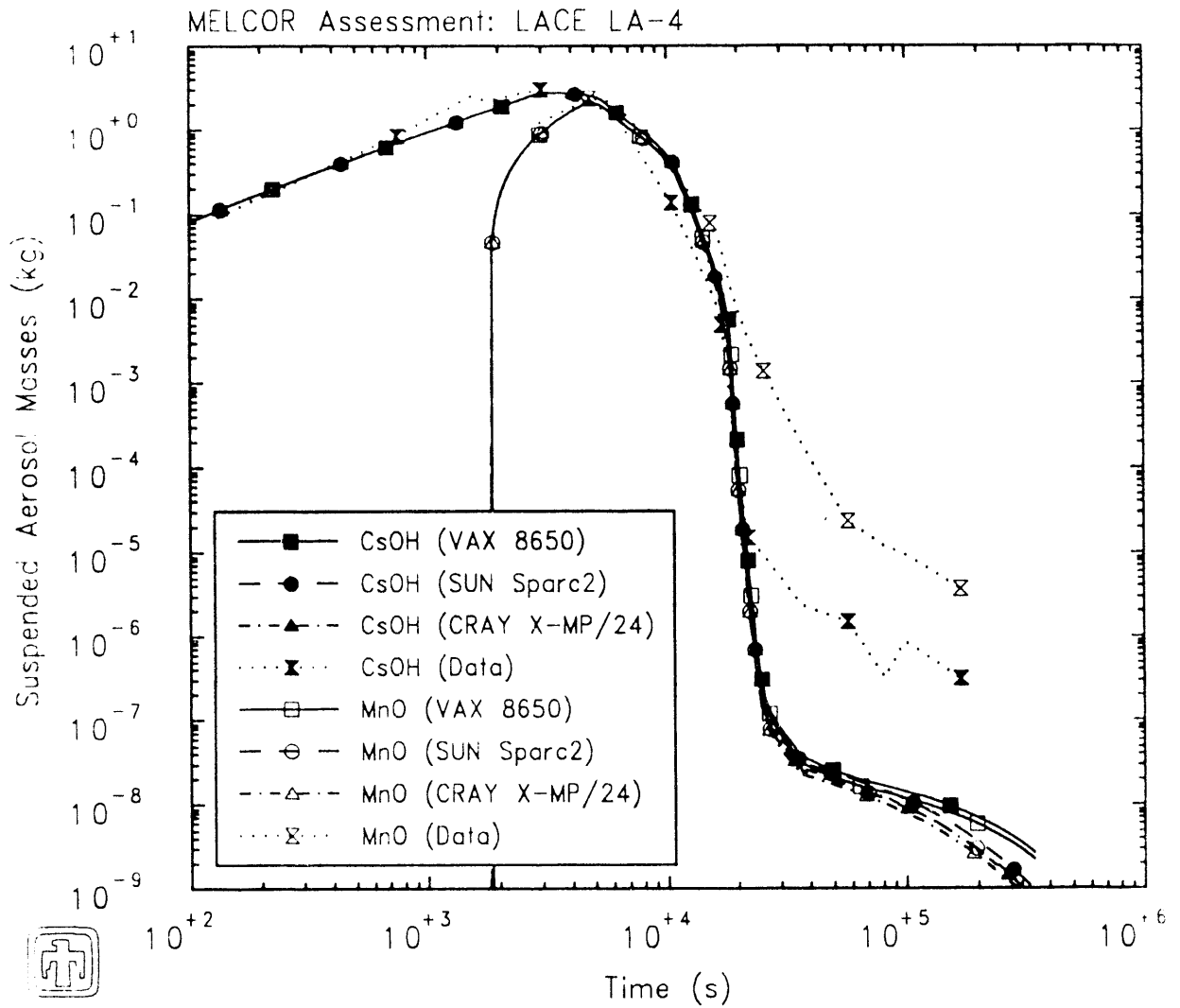
The reference calculation, whose results were described in detail in the previous section, was run with a maximum time step of 60s (1min) during the heatup, aerosol

MELCOR Assessment: IACE LA-4



IACE LA-4 (2-component)
 SBBJERZ 30JUL91 09:52:58 MELCOR

Figure 5.1.1. Total and Steam Partial Pressures - Machine Dependency
 Sensitivity Study



LACE LA-4 (2-component)
 3BJERZ 30JUL91 09:52:58 MELCOR

Figure 5.1.2. Suspended Aerosol Masses - Machine Dependency Sensitivity Study

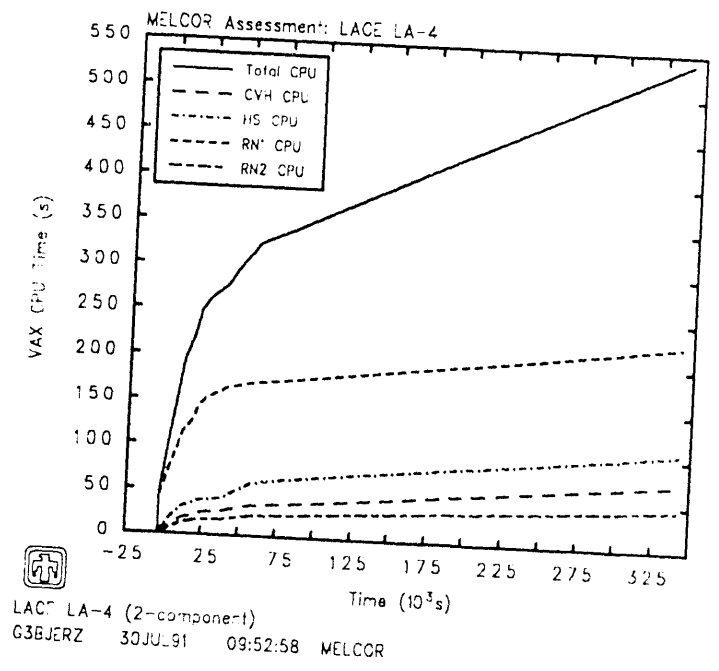
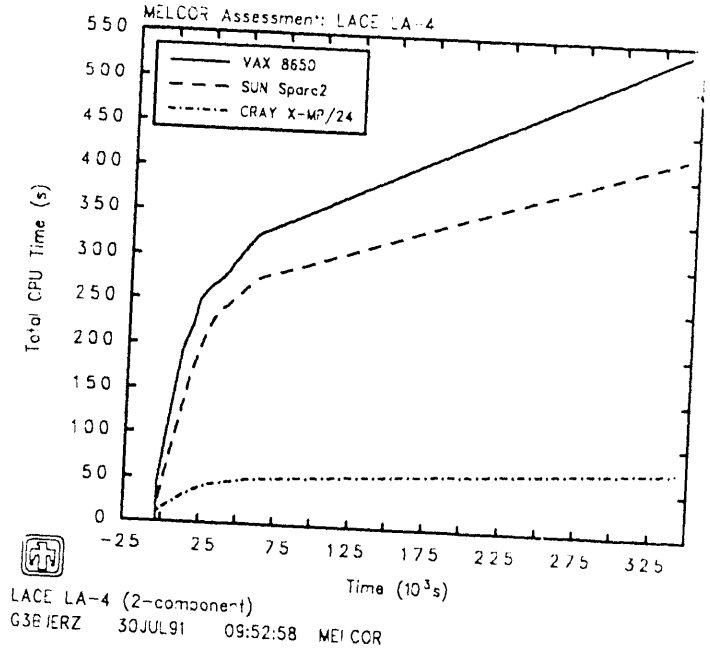


Figure 5.1.3. Total CPU Run Times (top) and VAX Package Run Times Machine Dependency Sensitivity Study

injections and steady-state periods, and a maximum time step of 600s (10min) during the cooldown period, with an intermediate maximum time step of 150s (2.5min) during the vent period. The code ran at the maximum allowed time step throughout.

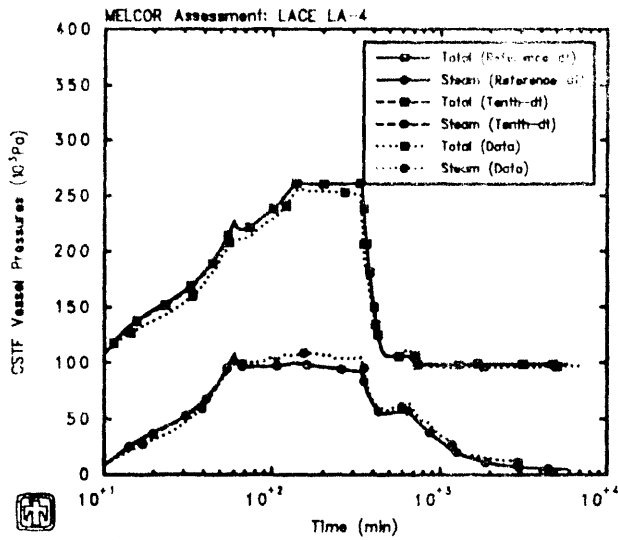
A sensitivity study was done in which this maximum time step was halved and doubled, or increased and decreased by an order of magnitude. Again, the code always ran at the maximum allowed time step throughout for each of these four cases. Figure 5.2.1 compares the measured total and steam partial pressures in the containment vessel to MELCOR results predicted using the base time step, and the four variations described above. Similarly, the test data for atmosphere and pool temperatures are shown in Figure 5.2.2 with results from the same five MELCOR calculations.

Reducing the time step by a factor of two or ten did not change the predicted results. Doubling the time step does not change the results except late in the transient, during the cooldown period, when the time step is 20min (compared to 2min earlier). Increasing the time step by a factor of ten (to 10min during heatup, injection and steady-state, increasing to 100min during cooldown) changes the predicted behavior throughout the problem, with substantial oscillations visible. The oscillations visible in the temperatures and pressures at the end of the problem for the largest time step used are related to code warnings about condensation mass transfer wanting to remove more than and actually scaled to remove only all of the steam volume present in the vessel.

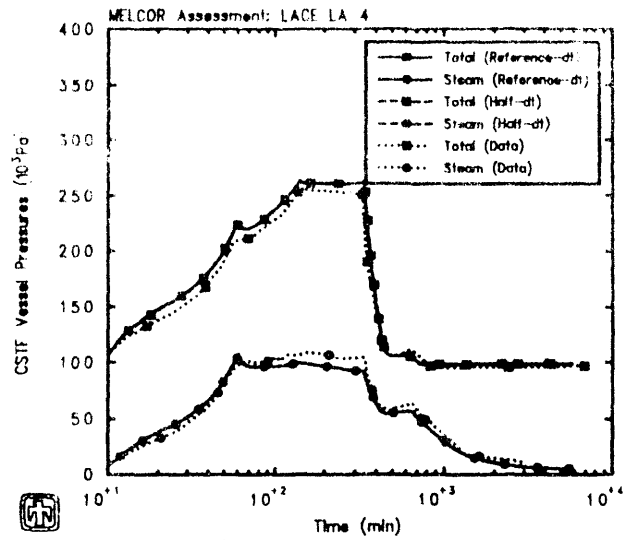
The suspended masses calculated for the two aerosol species in our reference analysis and in the four time-step studies done are presented in Figure 5.2.3, together with the test data. As with the thermal hydraulic response, very small changes are visible at late times when the time step is doubled, and small changes are visible throughout when the time step is increased by a factor of ten (especially dramatic at the end of the cooldown period).

Table 5.2.1 summarizes the post-test aerosol locations observed with those predicted in these five calculations. There are some quantitative differences among the predicted results obtained using the different time steps (especially for the largest time step used), but those differences are not significant enough to change the qualitative comparison of analysis to observation, or to provide substantial improvement in accuracy by any particular case.

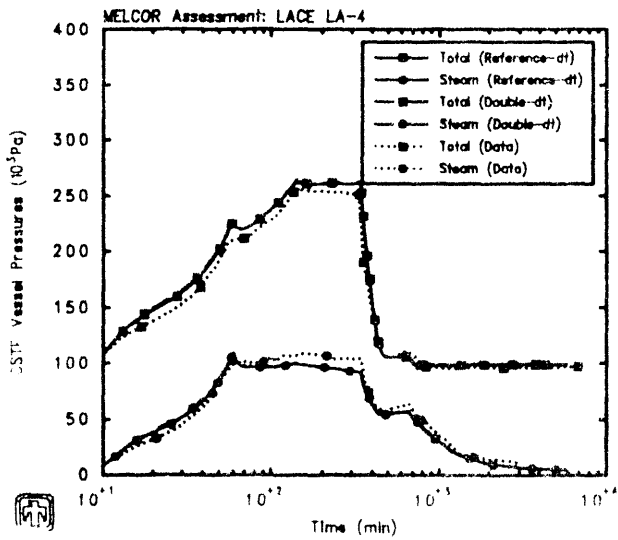
The total run time required (on a SUN Sparc2) for the reference analysis and for each of the four time-step studies done are compared in Figure 5.2.4.



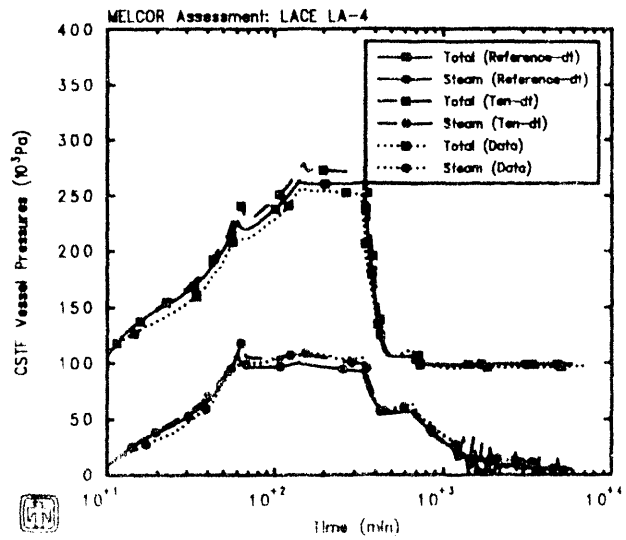
LACE LA-4 (2-component)
G2BKBN 7/29/91 10:14:33 MELCOR



LACE LA-4 (2-component)
G2BKBN 7/29/91 10:14:33 MELCOR



LACE LA-4 (2-component)
G2BKBN 7/29/91 10:14:33 MELCOR



LACE LA-4 (2-component)
G2BKBN 7/29/91 10:14:33 MELCOR

Figure 5.2.1. Total and Steam Partial Pressure - Time Step Sensitivity Study

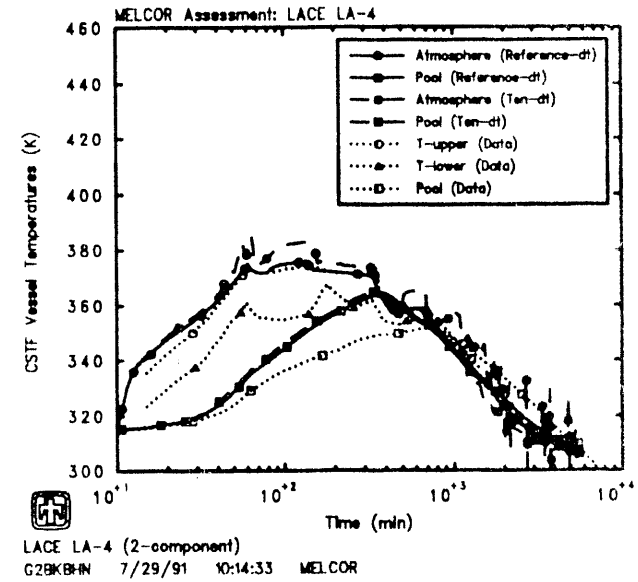
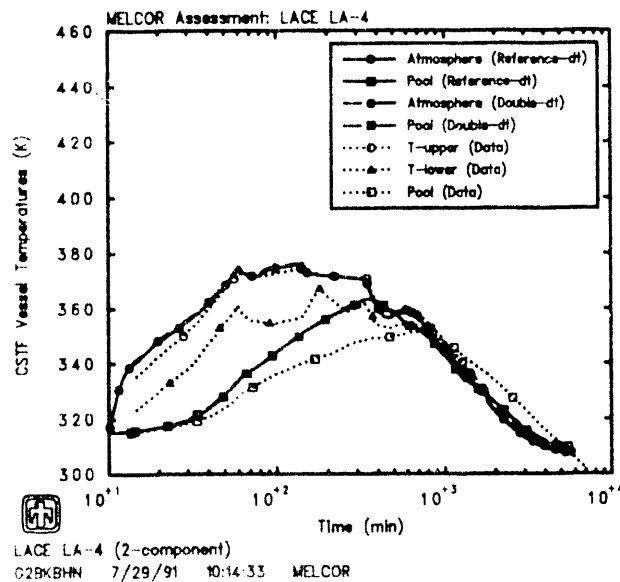
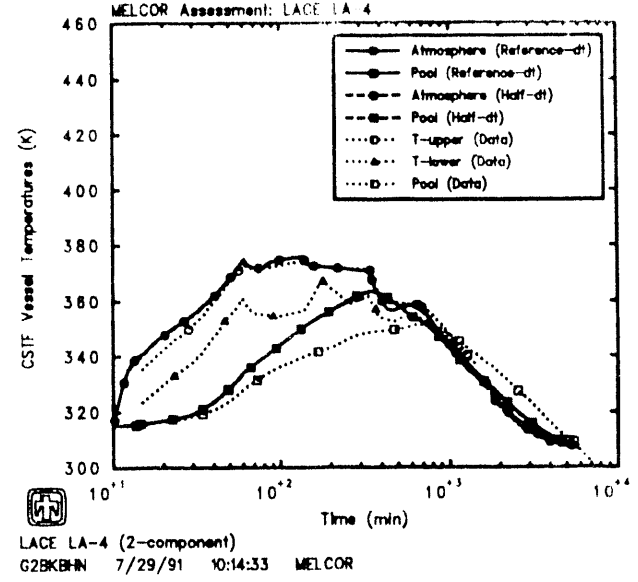
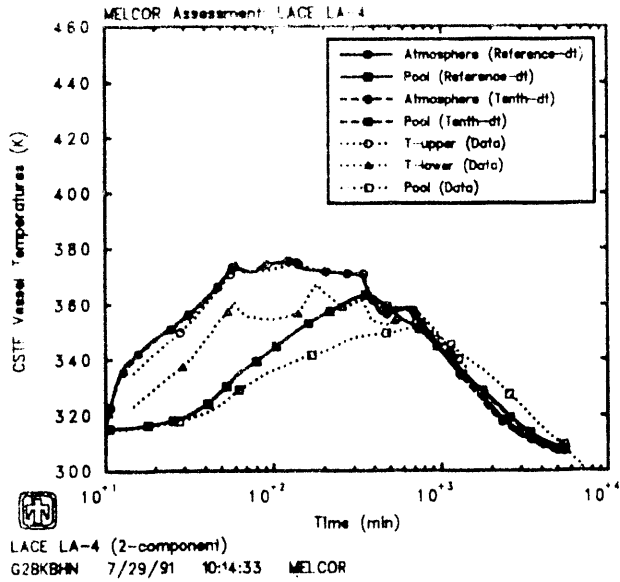


Figure 5.2.2. Atmosphere and Pool Temperatures - Time Step Sensitivity Study

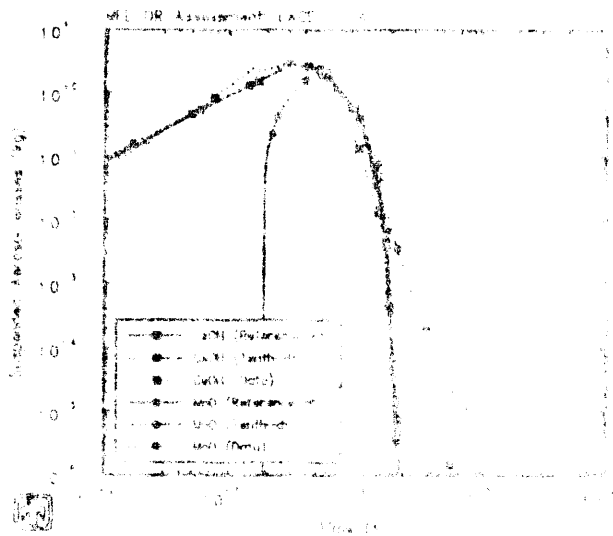


Figure 1: IR Assessment Plot 1. X-axis: Wavenumber (cm⁻¹), Y-axis: Absorbance. Legend includes CO₂ (Reference), CO₂ (Data), H₂O (Reference), H₂O (Data), and H₂O (Double-dt).

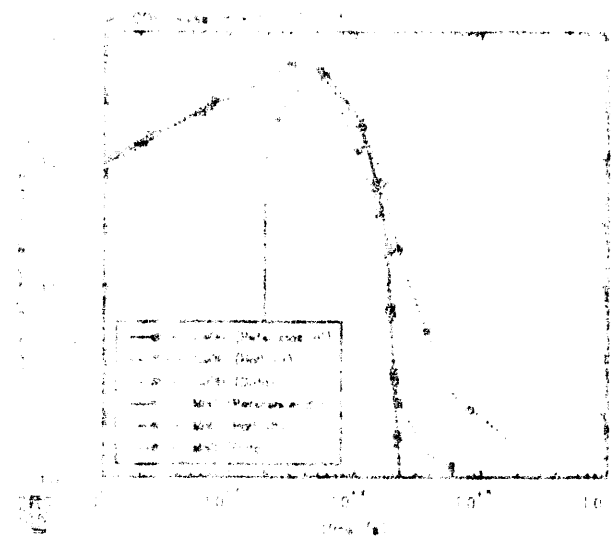


Figure 2: IR Assessment Plot 2. X-axis: Wavenumber (cm⁻¹), Y-axis: Absorbance. Legend includes CO₂ (Reference), CO₂ (Data), H₂O (Reference), H₂O (Data), and H₂O (Double-dt).

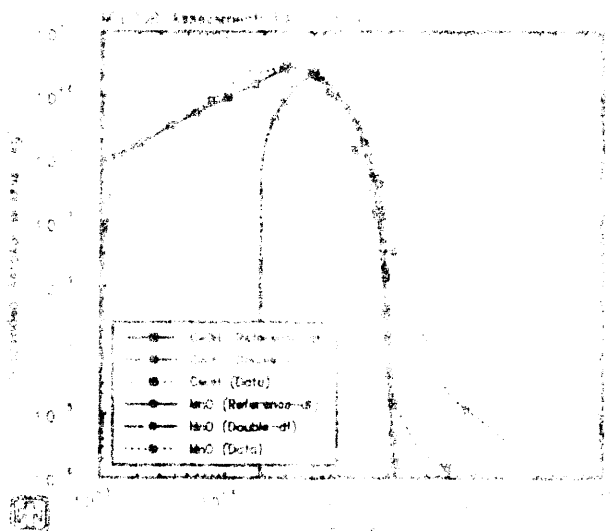


Figure 3: IR Assessment Plot 3. X-axis: Wavenumber (cm⁻¹), Y-axis: Absorbance. Legend includes CO₂ (Reference), CO₂ (Data), H₂O (Reference), H₂O (Data), and H₂O (Double-dt).

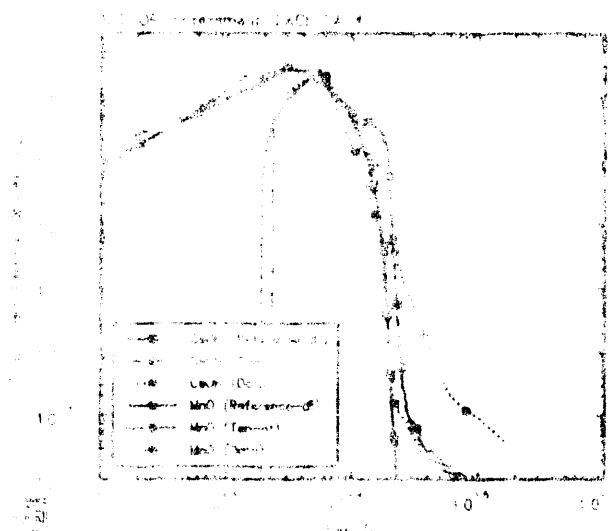
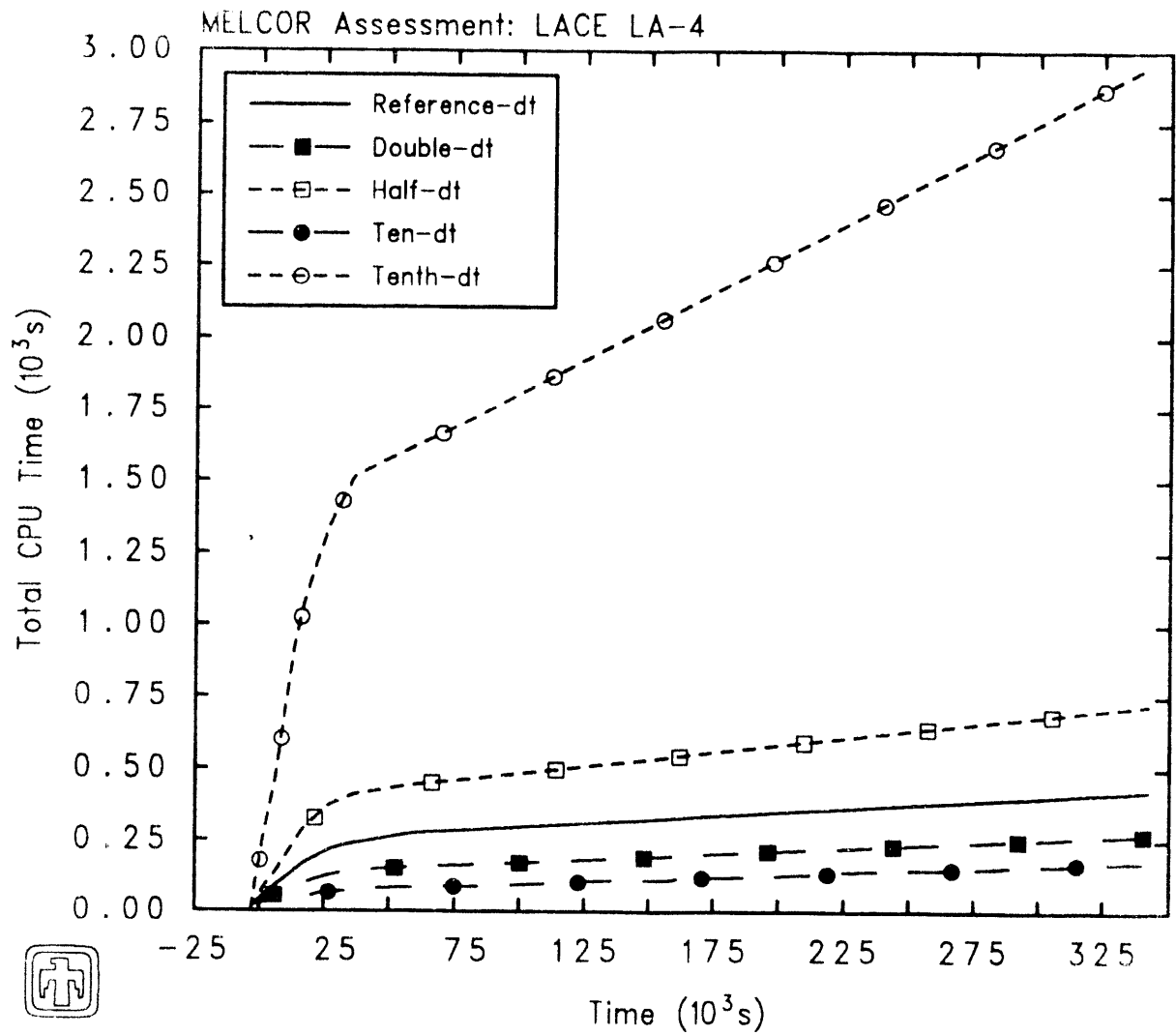


Figure 4: IR Assessment Plot 4. X-axis: Wavenumber (cm⁻¹), Y-axis: Absorbance. Legend includes CO₂ (Reference), CO₂ (Data), H₂O (Reference), H₂O (Data), and H₂O (Double-dt).



LACE LA-4 (2-component)
 G2BKBHN 7/29/91 10:14:33 MELCOR

Figure 5.2.4. Total CPU Time - Time Step Sensitivity Study

Table 5.2.1. Post Test Verification of Control - Fluorescence Sensitivity Study

Analyzed Species	Direction	Test Data			Code Data		
		Flow	Temp	Time	Case No	Location	Value
CSOH	Settled	2.563	2.640	2.611	2.615	2.603	2.471
	Partial	3.154	3.232	3.202	3.230	3.211	3.230
	Disturb	3.157	3.237	3.207	3.232	3.213	3.079
XnO	Settled	1.127	1.177	1.153	1.153	1.145	1.147
	Partial	1.128	1.177	1.157	1.147	1.133	1.157
	Disturb	1.131	1.181	1.157	1.154	1.147	1.096
Sump	Settled	1.518	1.578	1.553	1.548	1.548	1.518
	Partial	1.518	1.578	1.553	1.547	1.534	1.517
	Disturb	1.518	1.578	1.553	1.547	1.534	1.445

6 Aerosol Sensitivity Studies

In addition to the machine dependency and time step sensitivity studies described in the last section, a number of other modelling and/or code studies have been done. These can be divided into studies on parameters, models or variables which directly affect the thermal/hydraulic response (with the aerosol response affected only indirectly) and others which directly affect the aerosol behavior predicted. The former will be addressed in the next section; in this section, the results of varying such aerosol variables as aerosol transport with condensate films, volatility, the number of MAEROS components and sections, and nondefault values of aerosol-component size-distribution diameter ranges and dynamic and agglomeration shape factors are described.

6.1 Aerosol “Washdown”

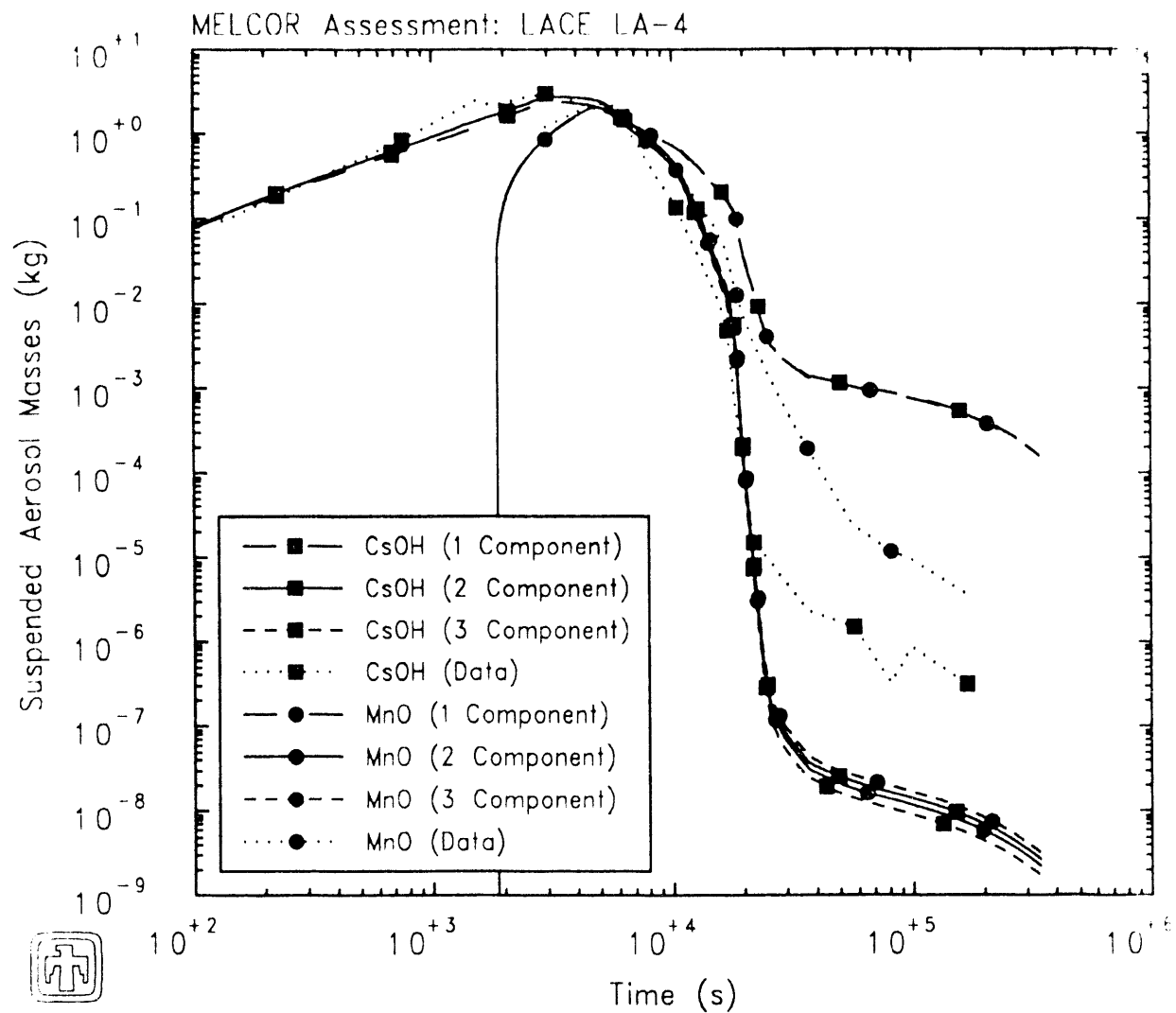
In MELCOR, a maximum allowed film thickness (of 0.5mm) is assumed for liquid condensate; any additional steam condensing onto the heat structure which would create a thicker film instead causes just enough drainage to the liquid pool in the corresponding control volume to maintain the maximum liquid condensate film thickness. Any aerosols (and fission product vapors) on the heat structure surface are assumed uniformly distributed in the film so that, when some fraction of the film (that liquid greater than the allowed maximum thickness) drains, a corresponding fraction of the plated aerosols are carried with the draining film into the liquid pool. And, as discussed in Sections 4.1, 7.1 and 7.2, there is significant condensation in this process.

A washdown coefficient has recently been added to MELCOR, for the analysis in which the degree to which aerosols drain with the liquid film can be adjusted. Set to 1.0, the general MELCOR treatment discussed above is maintained. Set to 0.0, no aerosol is assumed removed by draining film. The latter allows the effect of aerosol “washdown” on the discrepancy between the predicted and measured plated aerosol masses to be quantified.

A comparison of the predicted post-test aerosol locations for these two modeling extremes is given in Table 6.1, together with the test data. With the default MELCOR option of a washdown coefficient of 1.0, the plated aerosols can be seen to be concentrated in the upper part of the vessel, in the region of the core where temperatures are above 250°C. The aerosol distribution is similar to that shown in Section 4.1, and is in good agreement with the test data. The aerosol distribution for a washdown coefficient of 0.0 is shown in Table 6.1, and is in poor agreement with the test data.

6.2 Number of MAEROS Aerosol Components

The number of aerosol components in the MAEROS model is set to 4000 by default, and is assumed to be constant throughout the simulation. The MAEROS aerosol model



LACE LA-4 (1-component)

G3BJCYF 30JUL91 09:33:09 MELCOR

Figure 6.2.4. Suspended Aerosol Masses - Aerosol Component Sensitivity Study

large difference in the one- and multi-component aerosol model results is a difference in suspended aerosol particle size, illustrated in Figures 6.2.2 and 6.2.3.

The aerodynamic mass median diameters and the geometric standard deviations predicted using the single- and multi-component models are compared in Figure 6.2.2, together with the values derived from experimental observations; for the multi-component aerosol calculations, the values for the component(s) containing the injected aerosols are shown. With the two injected aerosols in a single component by themselves, the calculated results are in much better qualitative agreement with data, but substantially overpredicted in magnitude, especially around the peak. For three individual components, the calculated values for each of the two individual injected aerosol components are very similar to each other, and to the injected aerosol component results from the two-component model.

Figure 6.2.3 shows the aerosol masses in each of the twenty sections used in the one-component and three-component calculations (with the corresponding two-component plot given in the lower half of Figure 4.2.5), at ≥ 11000 s when the aerosol particles are settling out during the steady-state period. As in Figure 4.2.5, the total aerosol particle mass in each section (or size class) is given by the uppermost horizontal line over the particle diameter range of that section, while the relative fractions of the shaded regions represent the relative mass concentrations of the three aerosol species (CsOH, MnO and H₂O). With the one-component model, the water particles and the injected CsOH and MnO particles (which are smaller and larger, respectively, in the multi-component analyses) are forced into a single, averaged, size distribution; because of the much larger mass of (small) water particles present at this time, the shift in CsOH and MnO distributions to smaller particle sizes relative to the two- and three-component distributions is easily visible.

The final locations of the injected aerosols for each of these three cases, with corresponding test data, are given in Table 6.2.1 for each aerosol species and for the total. All three calculations correctly predict that the majority of the aerosol injection remains in the vessel, settled to the floor. The low plated masses predicted are seen in all three cases. The total aerosol mass leaked to containment for the two multi-component analyses is much less than either measured or predicted by the basecase, 1-component, calculation. The difference in amount of aerosols leaked in the multi-component vs. single-component sensitivity studies is probably directly related to the difference in suspended aerosol concentrations.

Using multiple aerosol components can sometimes require some additional cpu time, primarily by the RNI package, as shown by the run time comparisons in Figure 6.2.4, but the better agreement with data is probably worth it. In fact, at late times the one-component model takes more cpu time than either multi-component calculation, perhaps because the time needed to converge in the RNI iteration schemes depends somewhat on absolute magnitude of aerosol present, and the one-component calculation has significantly more suspended aerosols present late in time (as shown in Figure 6.2.1).

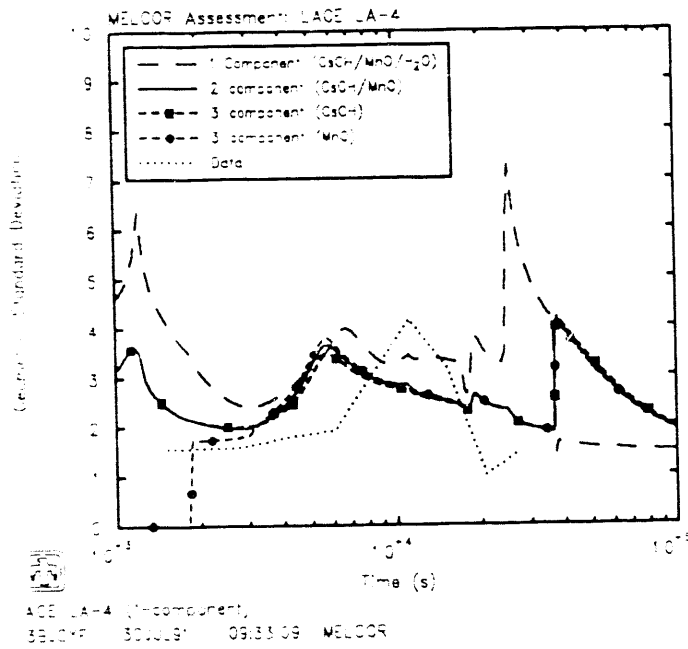
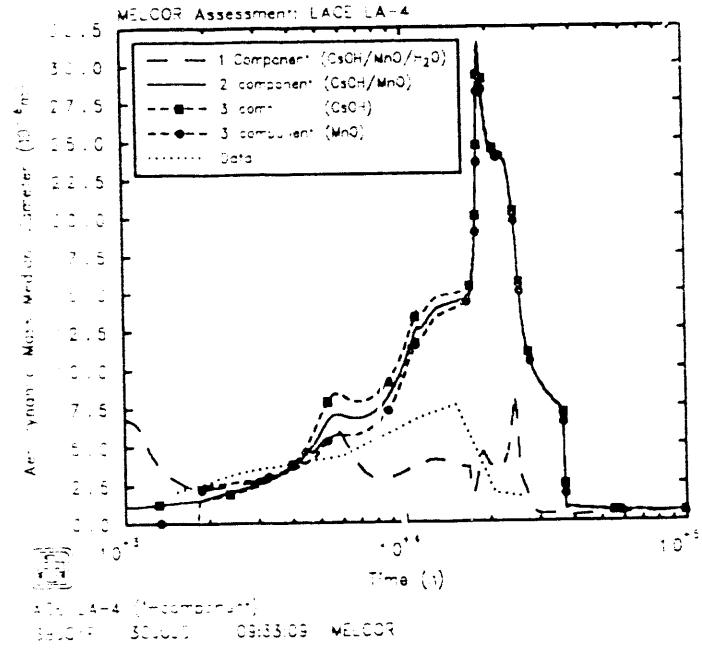


Figure 6.2.2. Aerodynamic Mass Median Diameter (top) and Geometric Standard Deviation (bottom) for Suspended Aerosols - Atomic Environment Sensitivity Study

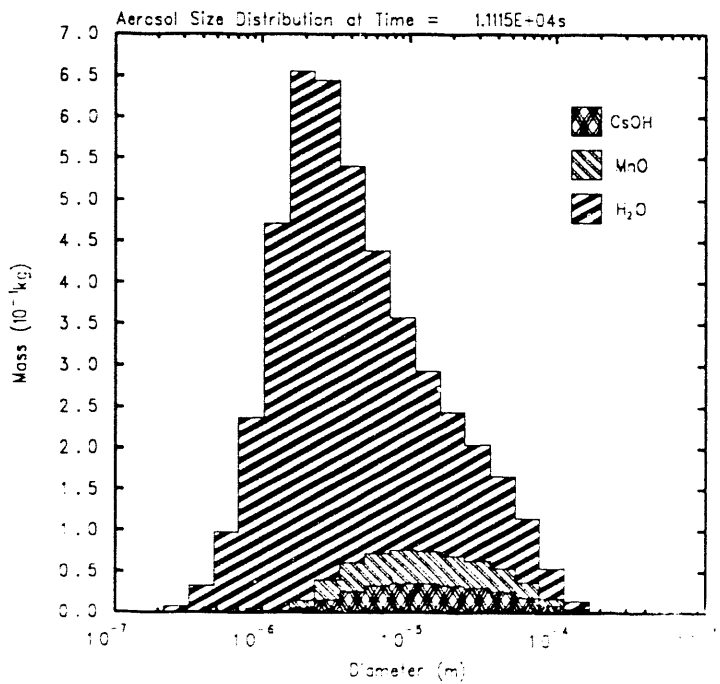
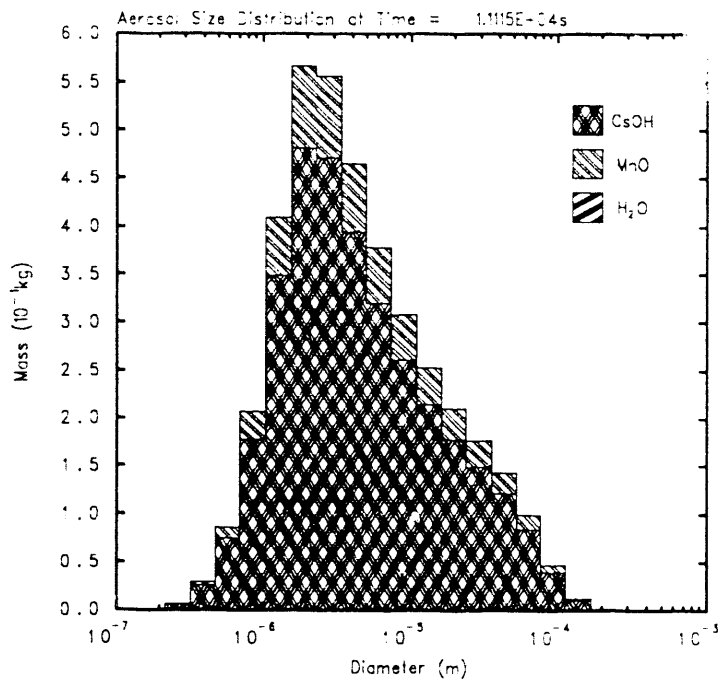
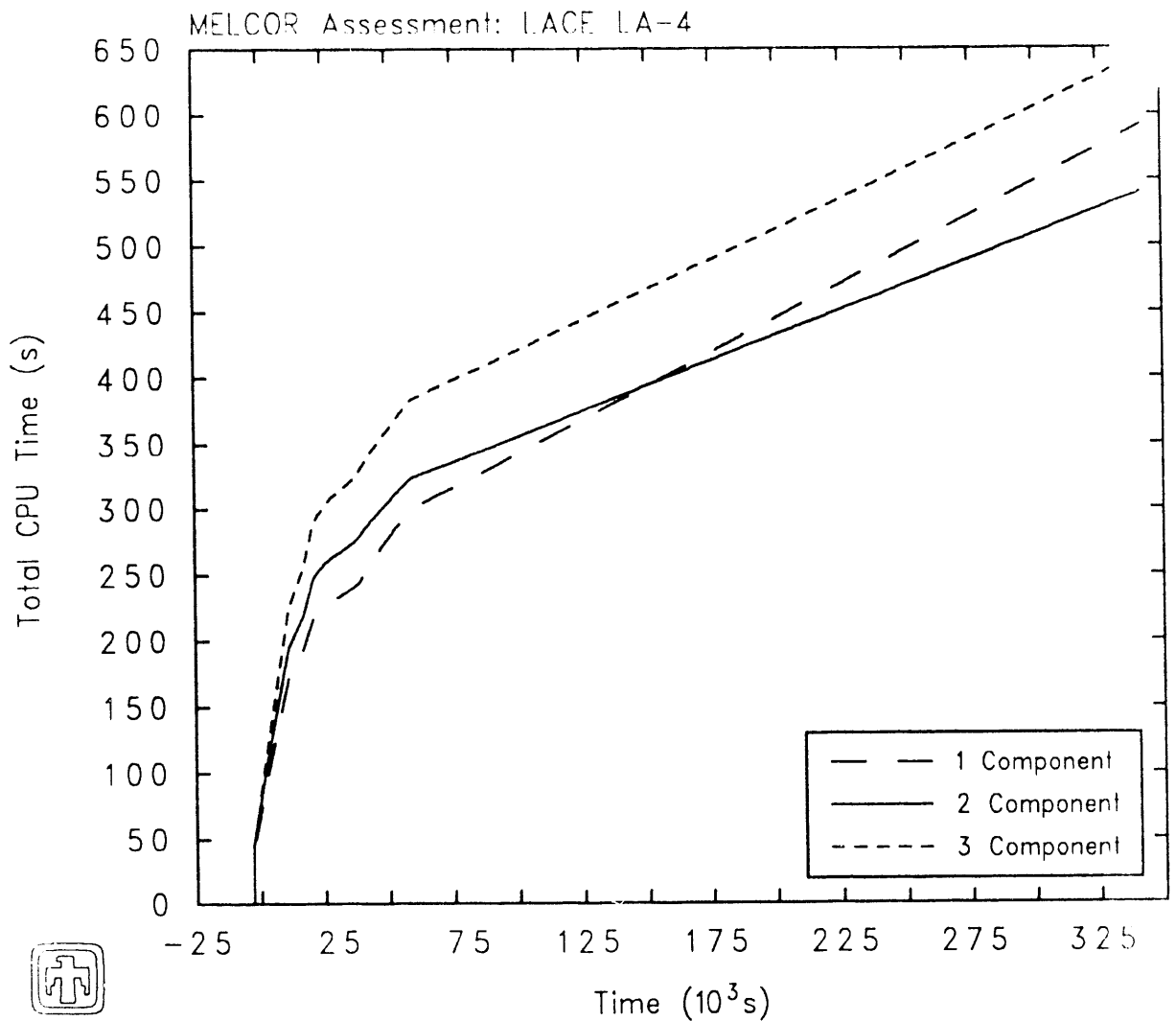


Figure 6.2.3. Size Distributions at $t=11000$ for One-Component (top) and Three-Components (bottom) for Suspended Aerosols - Aerosol Component Sensitivity Study.





 LACE LA-4 (1-component)
 BJCYF 30JUL91 09:33:09 MELCOR

Figure 6.2.4. Total CPU Run Times - Aerosol Component Sensitivity Study

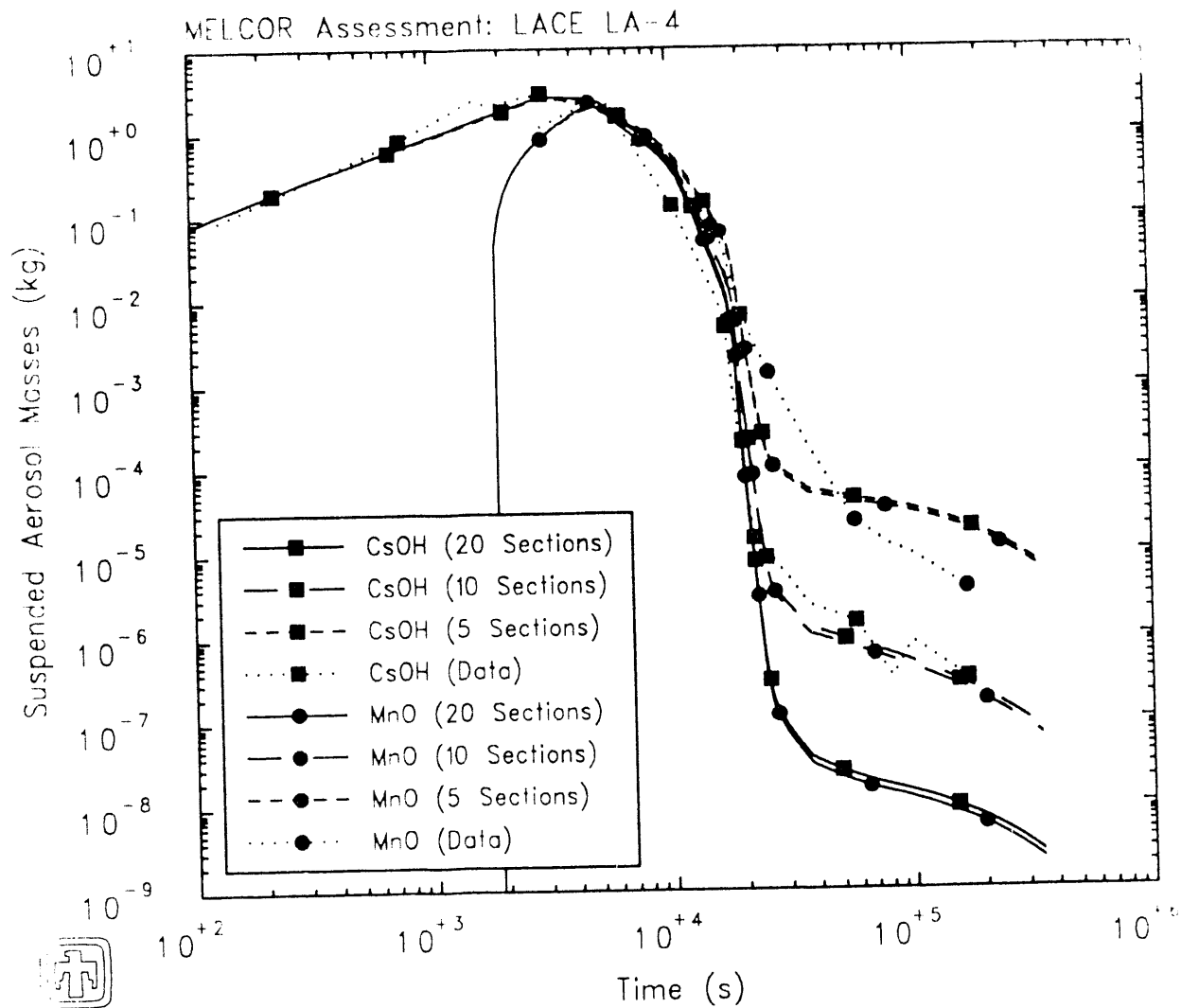
Table 6.2.1. PostTest Aerosol Locations - Multi-Component Sensitivity Study

Aerosol Species	Location	Test Data (kg)	Code (kg)		
			1-Component	2-Component	3-Component
CsOH	Settled	2.563	2.541	2.615	2.621
	Plated	0.304	0.238	0.230	0.224
	Leaked	0.007	0.068	0.002	0.002
MnO	Settled	1.927	2.055	2.153	2.144
	Plated	0.228	0.150	0.117	0.124
	Leaked	0.101	0.065	0.001	0.003
Sum	Settled	4.490	4.596	4.768	4.765
	Plated	0.532	0.388	0.347	0.348
	Leaked	0.108	0.133	0.003	0.005

6.3 Number of MAEROS (Size) Sections

The reference analysis discussed in Section 4 and the sensitivity studies discussed above all used twenty sections, or size bins, in the RNI aerosol calculations. This value was chosen because it was the input used in the CONTAIN calculation for LA4-9, and using the same value facilitates comparing results (as done in Section 8). However, the default number of sections used in MELCOR is only 5. Therefore, two sensitivity studies were done, in which either 5 or 10 sections were specified. The minimum and maximum diameters of the size distributions were left unchanged, so only the width of the bins was altered.

The test vessel suspended masses for the individual injected aerosol species calculated using these different size distribution resolutions are compared to each other and to test data in Figure 6.3.1. The agreement between measurement and prediction for all three sensitivity studies is very similar during the aerosol source periods, but the agreement becomes visibly and progressively degraded with coarser size distributions during the steady-state and early vent periods (~6000-20000s). The coarser size distribution resolutions also result in more suspended aerosol masses at late times, during the cooldown (~30000s). As with using different numbers of aerosol components, there are no visible differences in the thermal/hydraulic conditions being calculated using the different numbers of aerosol size distribution sections. Again, the principal reason for the difference in results*1) is a difference in aerosol particle



LACE LA-4 (2-component)
 BRJERZ 30JUL91 09:52:58 MELCOR

Figure 6.3.1. Suspended Aerosol Masses - Aerosol Sections Sensitivity Study

Table 6.3.1. PostTest Aerosol Locations – Aerosol Size Distribution Resolution Sensitivity Study

Aerosol Species	Location	Test Data (kg)	Code (kg)		
			20-section	10-section	5-section
CsOH	Settled	2.563	2.615	2.608	2.593
	Plated	0.304	0.230	0.234	0.239
	Leaked	0.007	0.002	0.005	0.015
MnO	Settled	1.927	2.153	2.145	2.124
	Plated	0.228	0.117	0.122	0.133
	Leaked	0.101	0.001	0.004	0.014
Sum	Settled	4.490	4.768	4.753	4.717
	Plated	0.532	0.347	0.356	0.372
	Leaked	0.108	0.003	0.009	0.029

Figure 6.3.2 presents the aerodynamic mass median diameters and the geometric standard deviations predicted using the three different numbers of sections, together with values derived from experimental observations. The aerosol mass distributions in the ten-section and five-section calculations at ≥ 11000 s are given in Figure 6.3.3 (with the corresponding twenty-section plot given in the lower half of Figure 4.2.5). This time is of particular interest because the aerosol particles are settling out during the steady-state period. The comparisons in both figures indicate that the suspended aerosol particles are settling out more slowly in the calculations with fewer sections because the particles are somewhat smaller on average at any given time with the coarser distribution resolution. However, predicted average particle sizes similar to given experimental values ($\approx 10\mu\text{m}$ at about 20000s) result in less settling out and higher suspended aerosol masses in MELCOR than observed in the experiment.

The final locations of the injected aerosols for each of these three cases, with corresponding test data, are given in Table 6.3.1 for each aerosol species and for the total. Again, all three calculations correctly predict that the majority of the aerosol injection remains in the vessel, settled to the floor. As seen in other sensitivity studies, the total aerosol mass leaked to containment increases as the suspended aerosol mass in the vessel increases.

Using more sections in the aerosol size distribution to increase resolution always requires additional cpu time, primarily by the RNI package, as shown by the run

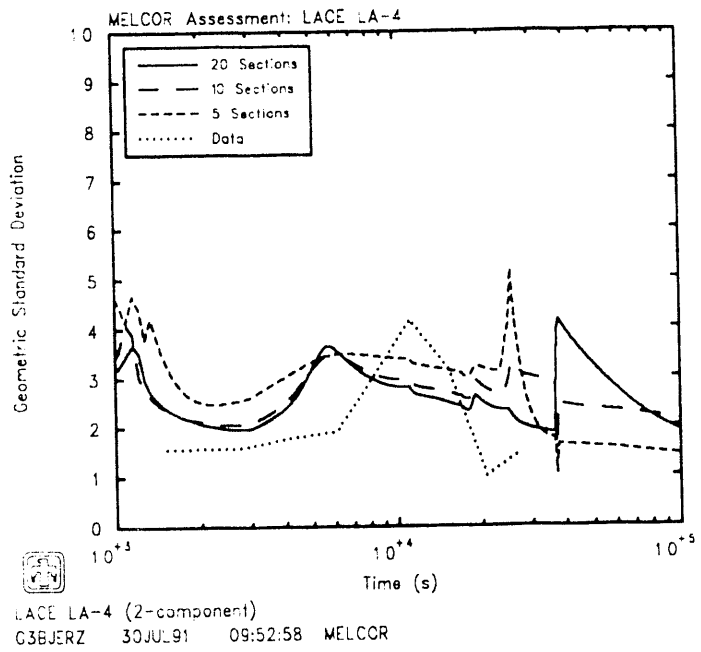
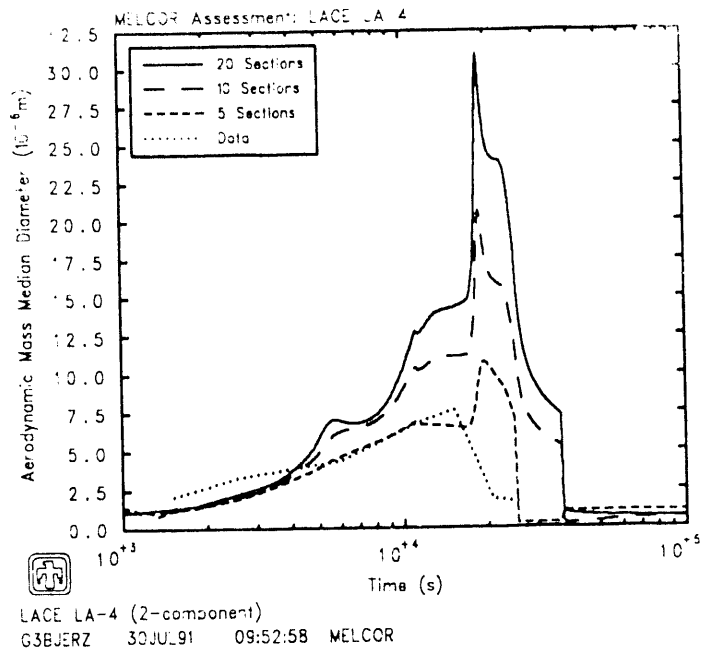


Figure 6.3.2. Aerodynamic Mass Median Diameter (top) and Geometric Standard Deviation (bottom) for Suspended Aerosols - Aerosol Sections Sensitivity Study

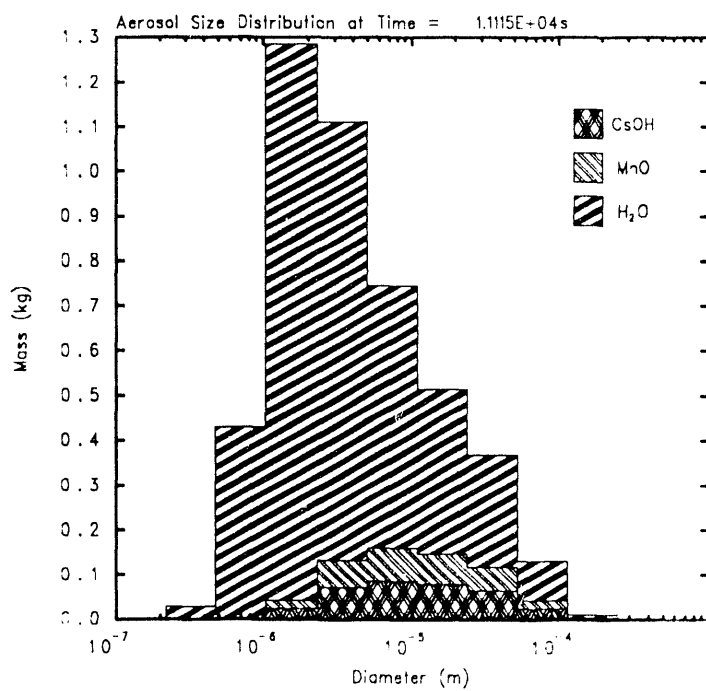
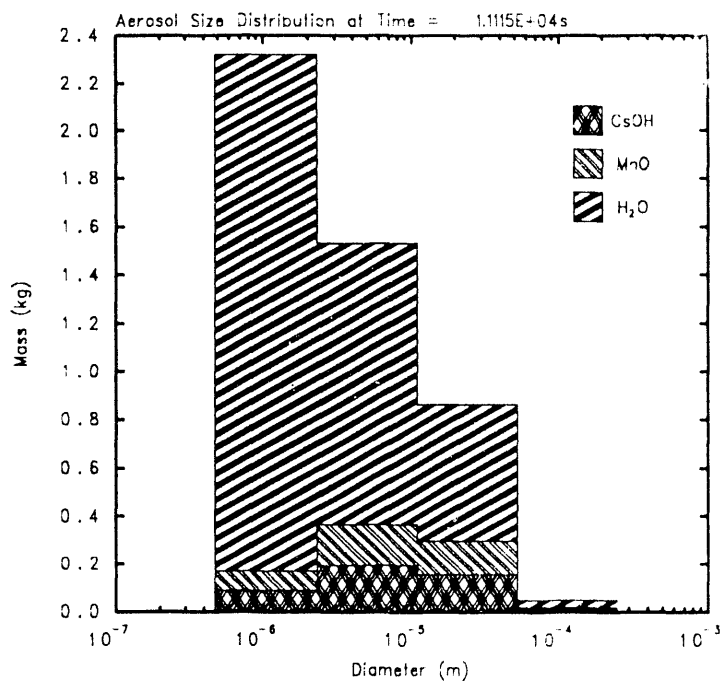


Figure 6.3.3. Size Distributions at ~11000s for 5- (top) and 10- (bottom) sections for Suspended Aerosols - Aerosol Sections Sensitivity Study

time comparisons in Figure 6.3.4.

6.4 Use of (Non)Default RN Parameters

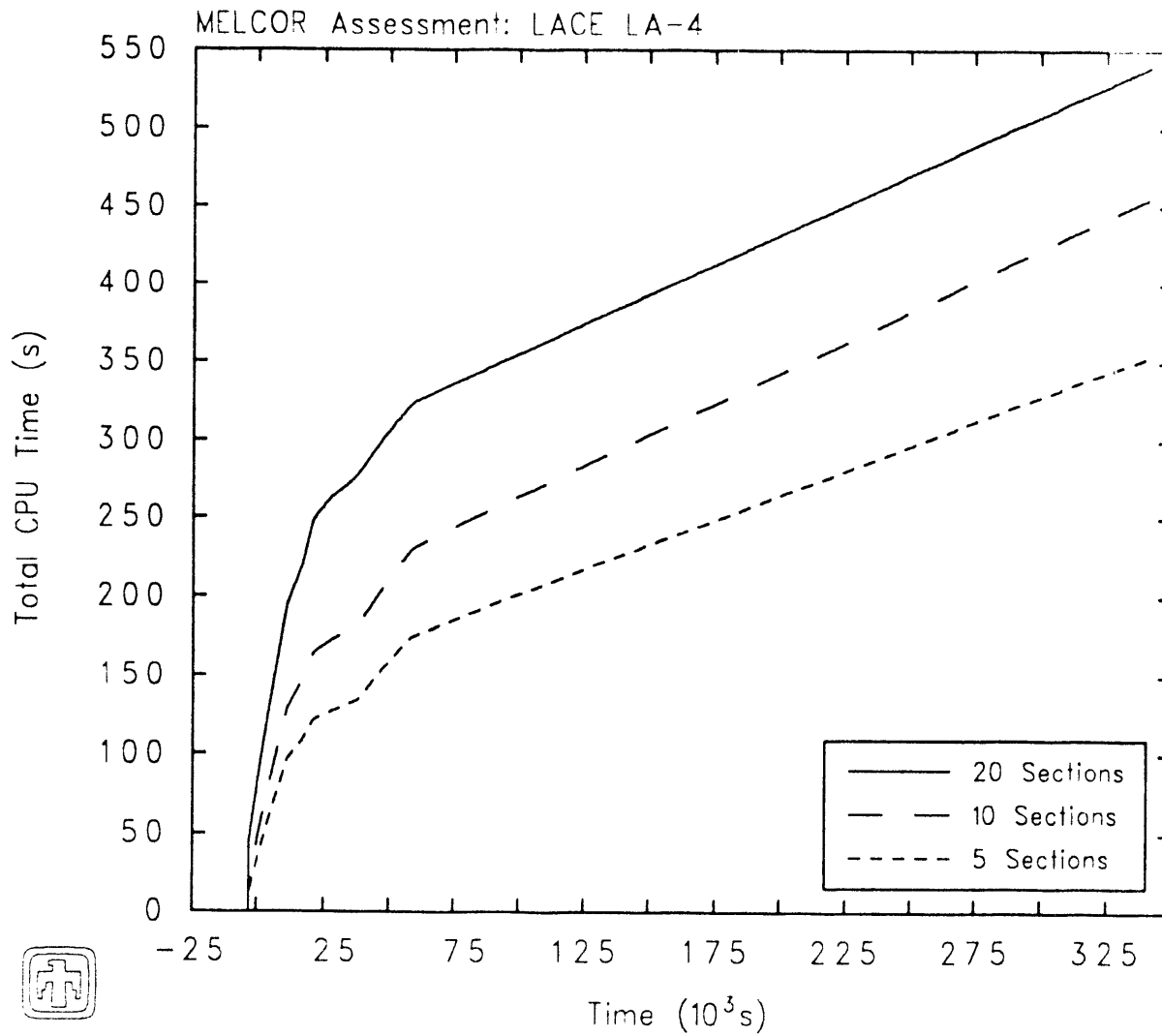
The reference analysis discussed in Section 4 used non-default maximum and minimum diameters for the MAEROS aerosol component size distributions, taken from the CONTAIN input deck [9] to be 0.1 and 250 μm , respectively, rather than the default 1 and 50 μm MELCOR values. A sensitivity calculation was run in which the default diameter ranges were used. That calculation could not use 20 size bins, like the reference calculation, because of an enforced assumption in MAEROS that the ratio of the upper to lower mass boundary for each section or size bin is ≥ 2 . Instead, 10 sections were used, and the results were compared to the results from the 10-section analysis in the number-of-sections sensitivity study (discussed already in the last subsection). There were no visible differences in results using the narrower, default, diameter range than using the greater range assumed in the reference input.

Other nondefault values used in the RN package input were 1.85 for the dynamic shape factor (DSF), taken from the CONTAIN input [9], and 2.25 for the agglomeration shape factor (ASF), taken from the CONTAIN and MELCOR ABCOVE analyses [2], both default to 1.0 in MELCOR. As another sensitivity study, three calculations were done, in which one and/or the other were reset to their default values.

Figure 6.4.1 shows each of the two individual species suspended aerosol masses in the vessel for the reference analysis, and predicted using other combinations of default/nondefault shape factor values, compared to test data; the two injected aerosols are shown separately to allow clear distinction between curves and line types. An agglomeration shape factor of 2.25 always produces better agreement with the data than the default value of 1.0, whatever the dynamic shape factor, especially during the steady-state period at 6000-20000s. A dynamic shape factor of 1.85 results in slightly higher suspended aerosol masses than using its default value of 1.0, in the steady-state, vent and cooldown periods.

The aerodynamic mass median diameters and the geometric standard deviations predicted using the default and/or nondefault shape factors are compared in Figure 6.4.2, together with the values derived from experimental observations; in all these cases (which all use the two-component reference model), the values for the component containing the injected aerosols are shown. An agglomeration shape factor set to 2.25 results in larger aerosol particles on average than with the default value of 1.0, regardless of the value of the dynamic shape factor. Larger aerosol particles settle out faster, so these comparisons are consistent with the relative amounts of suspended aerosol given in Figure 6.4.1.

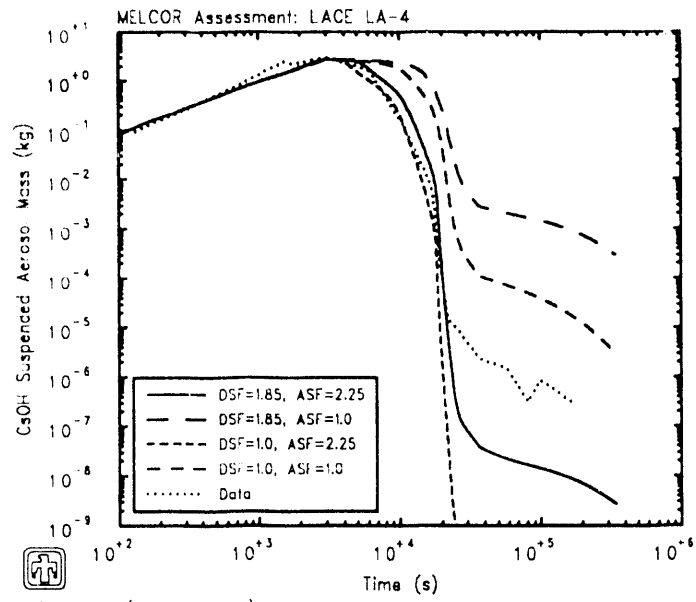
Figure 6.4.3 shows the aerosol masses in each of the twenty sections used in the various shape factor calculations (with the reference analysis plot given in the upper left), at 11000s when the aerosol particles are settling out during the steady-state



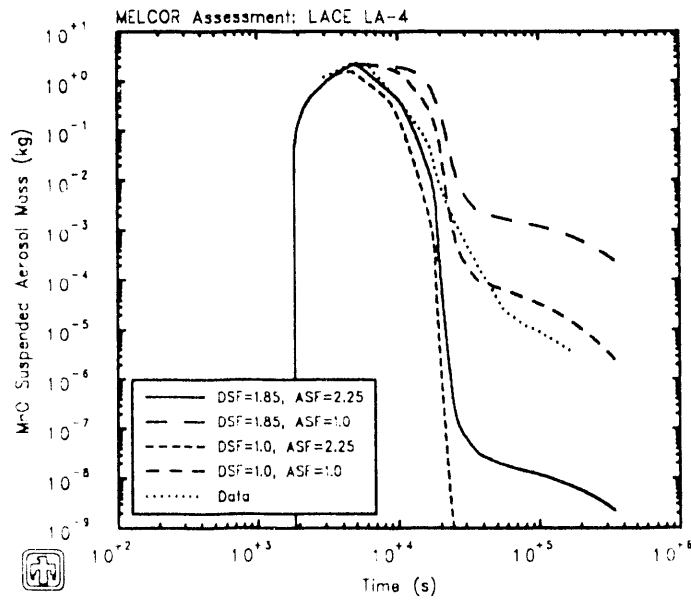
LACE LA-4 (2-component)

G3BJERZ 30JUL91 09:52:58 MELCOR

Figure 6.3.4. Total CPU Run Times - Aerosol Sections Sensitivity Study



LACE LA-4 (2-component)
 G3BJERZ 30JUL91 09:52:58 MELCOR



LACE LA-4 (2-component)
 G3BJERZ 30JUL91 09:52:58 MELCOR

Figure 6.4.1. CaOH (top) and MnO (bottom) Suspended Aerosol Masses Shape Factors Sensitivity Study

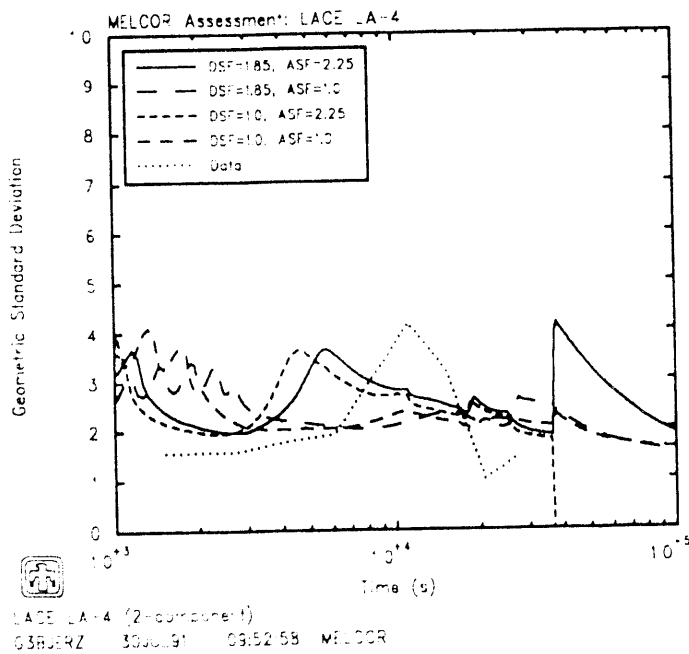
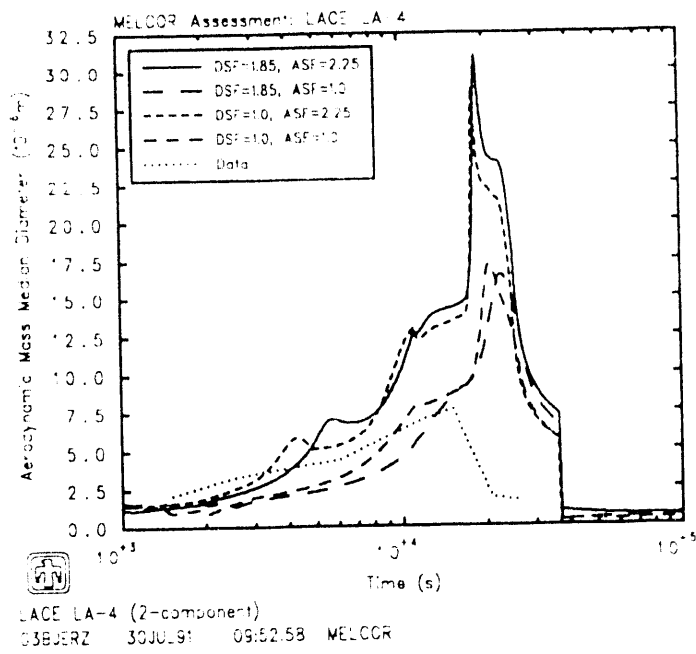


Figure 6.4.2. Aerodynamic Mass Median Diameter (top) and Geometric Standard Deviation (bottom) for Suspended Aerosols - Shape Factor Sensitivity Study

Table 6.4.1. PostTest Aerosol Locations – Shape Factors Sensitivity Study

Aerosol Species	Location	Test Data (kg)	Code (kg)			
			DSF=1.85 ASF=2.25	DSF=1.85 ASF=1.0	DSF=1.0 ASF=2.25	DSF=1.0 ASF=1.0
CsOH	Settled	2.563	2.615	2.048	2.651	2.398
	Plated	0.304	0.230	0.445	0.196	0.366
	Leaked	0.007	0.002	0.353	2×10^{-4}	0.083
MnO	Settled	1.927	2.153	1.687	2.181	1.970
	Plated	0.228	0.117	0.288	0.090	0.229
	Leaked	0.101	0.001	0.296	2×10^{-4}	0.072
Sum	Settled	4.490	4.768	3.735	4.832	4.368
	Plated	0.532	0.347	0.733	0.286	0.595
	Leaked	0.108	0.003	0.649	4×10^{-4}	0.155

period. As in Figure 4.2.5, the total aerosol particle mass in each section (or size class) is given by the uppermost horizontal line over the particle diameter range of that section, while the relative fractions of the shaded regions represent the relative mass concentrations of the three aerosol species (CsOH, MnO and H₂O). For both calculations with an agglomeration shape factor of 2.25 (in the upper half of the figure), less injected aerosols and less water aerosols are present and the injected aerosol size distribution peaks at larger diameters than with a default agglomeration shape factor of 1.0 (in the lower half of the figure). Figure 6.4.1 showed that the dynamic shape factor did not have a strong effect on the results at this time. However, some differences are visible between the two calculations done with a dynamic shape factor of 1.85 (in the left half of the figure) and the two calculations done with a default dynamic shape factor of 1.0 (in the right half of the figure); in particular, the default dynamic shape factor results in somewhat broader size distributions for the injected aerosol component.

The final locations of the injected aerosols for each of these three sensitivity study cases and the reference calculation, with corresponding test data, are given in Table 6.4.1 for each aerosol species and for the total. All calculations correctly predict that the majority of the aerosol injection remains in the vessel, settled to the floor. The relative amounts of predicted plated mass and of total aerosol mass leaked to containment in the different sensitivity study calculations appear directly proportional to the differences seen in the suspended aerosol masses in the various calculations in Figure 6.4.1.

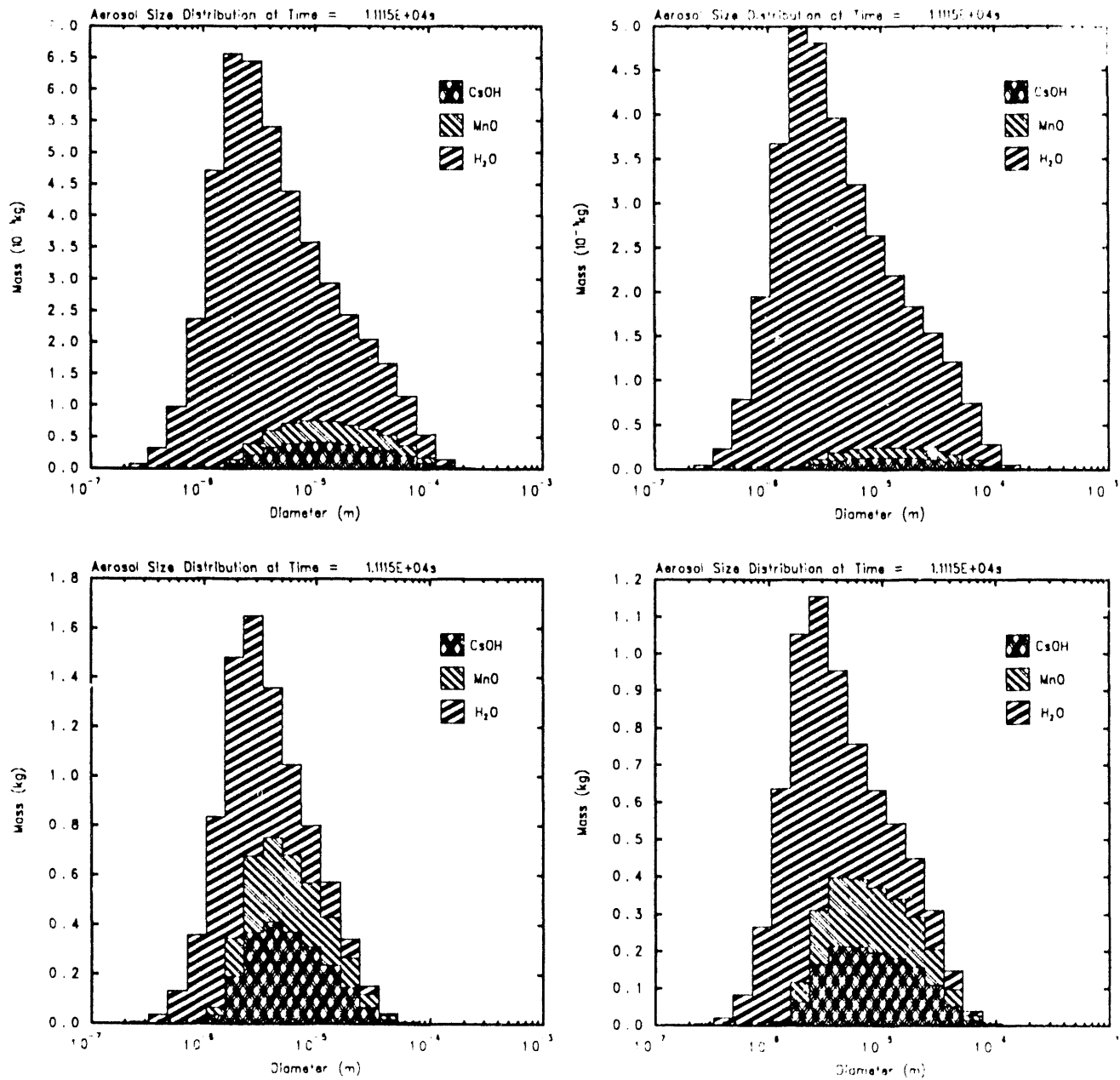


Figure 6.4.3. Size Distributions for Suspended Aerosols at ~ 11000 s for Reference Calculation (upper left), Nondefault Agglomeration Shape Factor (upper right), Nondefault Dynamic Shape Factor (lower left), and Default Shape Factors (lower right) – Shape Factors Sensitivity Study

7 Thermal/Hydraulic Sensitivity Studies

Another set of sensitivity studies have been done on parameters, models or variables which directly affect the thermal/hydraulic response (with the aerosol response affected only indirectly). In this section, the results of varying such thermal/hydraulic variables as condensation, radiation heat transfer and insulation thermal conductivity are described.

7.1 Condensation on Pool Surface

The reference analysis included a detailed volume-altitude table in the lower region of the containment vessel. This was not our first attempt at modelling the CSTF vessel. Our original control-volume model consisted of a simple straight cylinder, with diameter equal to that of the test vessel and height set to give the correct total volume: this would be the typical input model that we believe most users would define in similar problems. We found that that simple model had to be refined in order to obtain better agreement with test data. As a sensitivity study, a calculation using that original, straight-cylinder, model was redone.

The basic phenomenon under evaluation is the condensation of steam from the vessel atmosphere onto the pool surface, a function both of the temperature differences and of the pool surface area. In the straight-cylinder model, the pool surface area is always at its maximum (the cylinder cross-sectional area), while the more detailed volume-altitude table reflects the increase in cross-sectional area with increasing elevation in the elliptical lower head. For small amounts of pool, the surface area is substantially reduced from the maximum, straight-cylinder, value, effectively decreasing the area over which condensation occurs.

The upper plot in Figure 7.1.1 shows the total and steam partial pressures predicted in the containment vessel for the two different input models (differing only in the volume-altitude tables used for the vessel control volume), together with the corresponding test data: the bulk atmosphere and pool temperatures for these two calculations are compared in the lower plot in Figure 7.1.1. The most visible difference is in the pool temperature, which was as much as 20K higher than the already overpredicted pool temperature, and perhaps 40K greater than observed, during the startup, aerosol injection and steady-state periods. This higher pool temperature results in slightly lower total and steam partial pressures, and bulk atmosphere temperature, during the same time periods. Figure 7.1.2 presents a comparison of the suspended masses predicted for the two aerosols in these two calculations, with experimental data. The suspended aerosol masses appear unaffected even during those earlier periods when the pressures and temperatures are different for the two calculations.

The measured post-test aerosol locations are compared with those predicted by

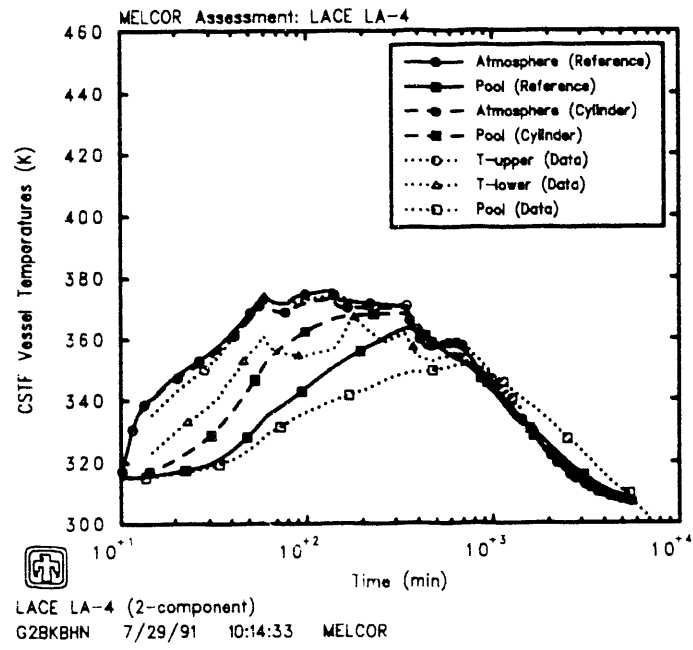
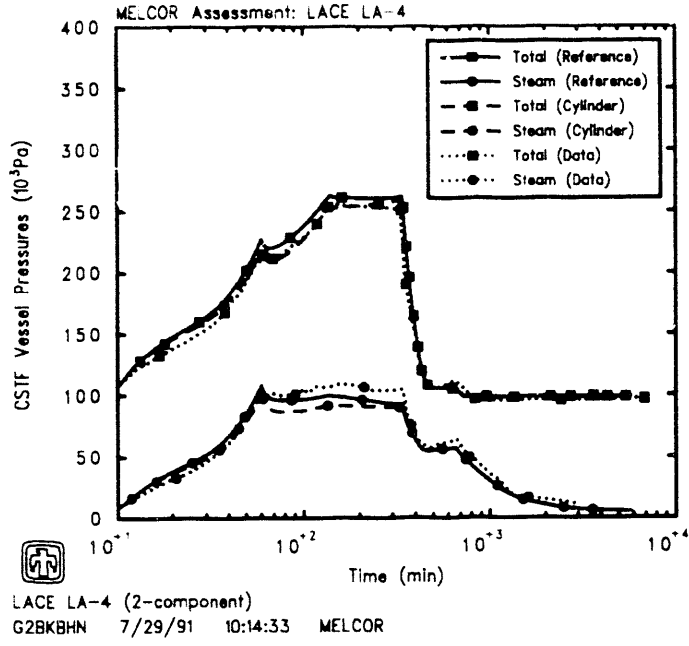


Figure 7.1.1. Total and Steam Partial Pressures (top) and Atmosphere and Pool Temperatures (bottom) - Pool Condensation Sensitivity Study

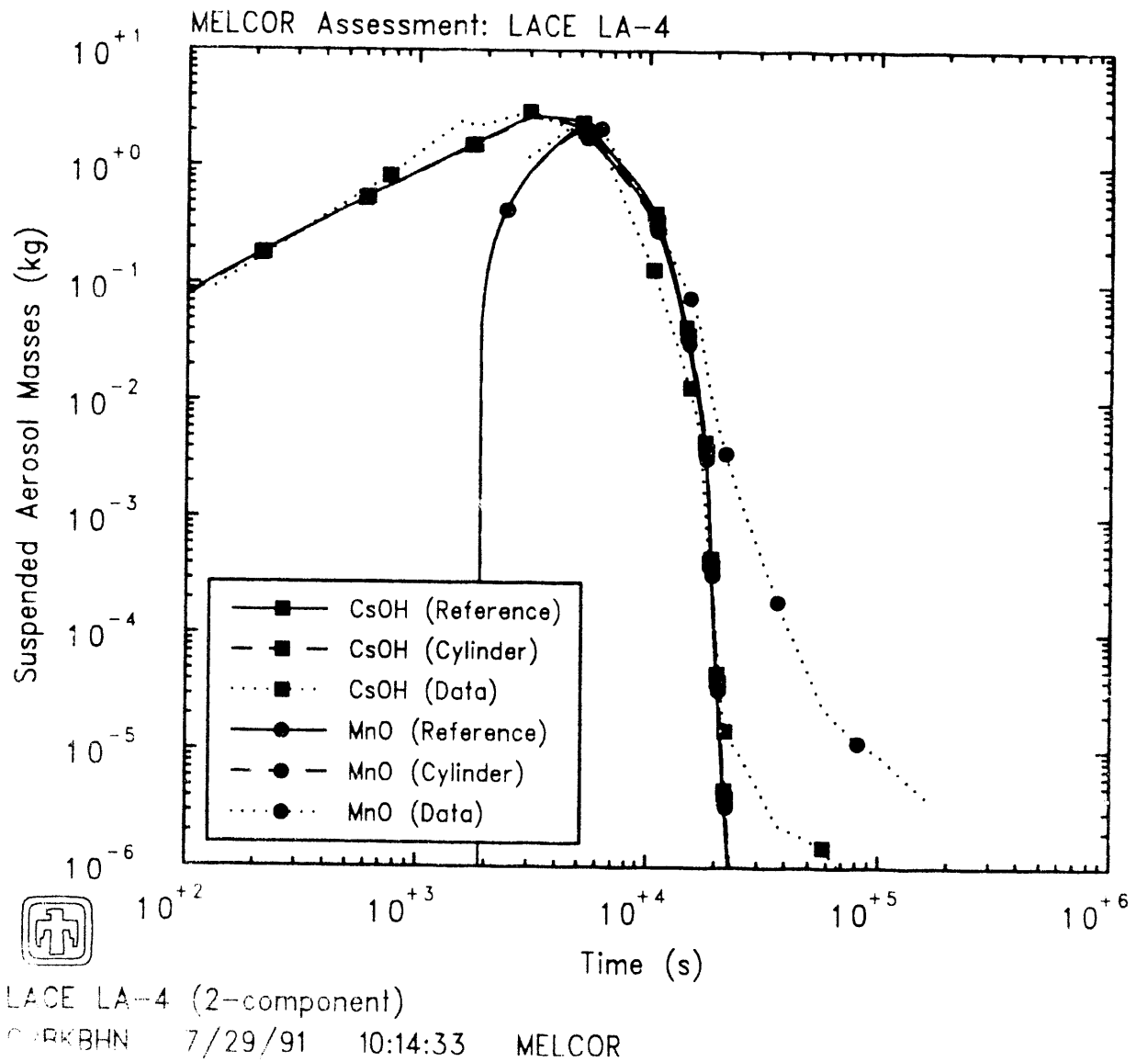


Figure 4-12. Suspended Aerosol Masses - Pool Condensation Sensitivity Study

Table 7.1.1. Post-Test Area of Locations - Pool Condensation Sensitivity Study

Aerosol Species	Location	Test Data (ppm)	Codebook Reference (ppm/der)	Codebook Reference (ppm/der)
COH	Sealed	2.001	2.043	2.049
	Placed	0.004	0.006	0.027
	Leaked	0.007	0.002	0.002
MnO	Sealed	1.027	1.153	2.148
	Placed	0.218	0.117	0.121
	Leaked	0.207	0.001	0.002
Spt	Sealed	1.100	1.163	1.767
	Placed	0.801	0.147	2.148
	Leaked	2.108	0.001	0.004

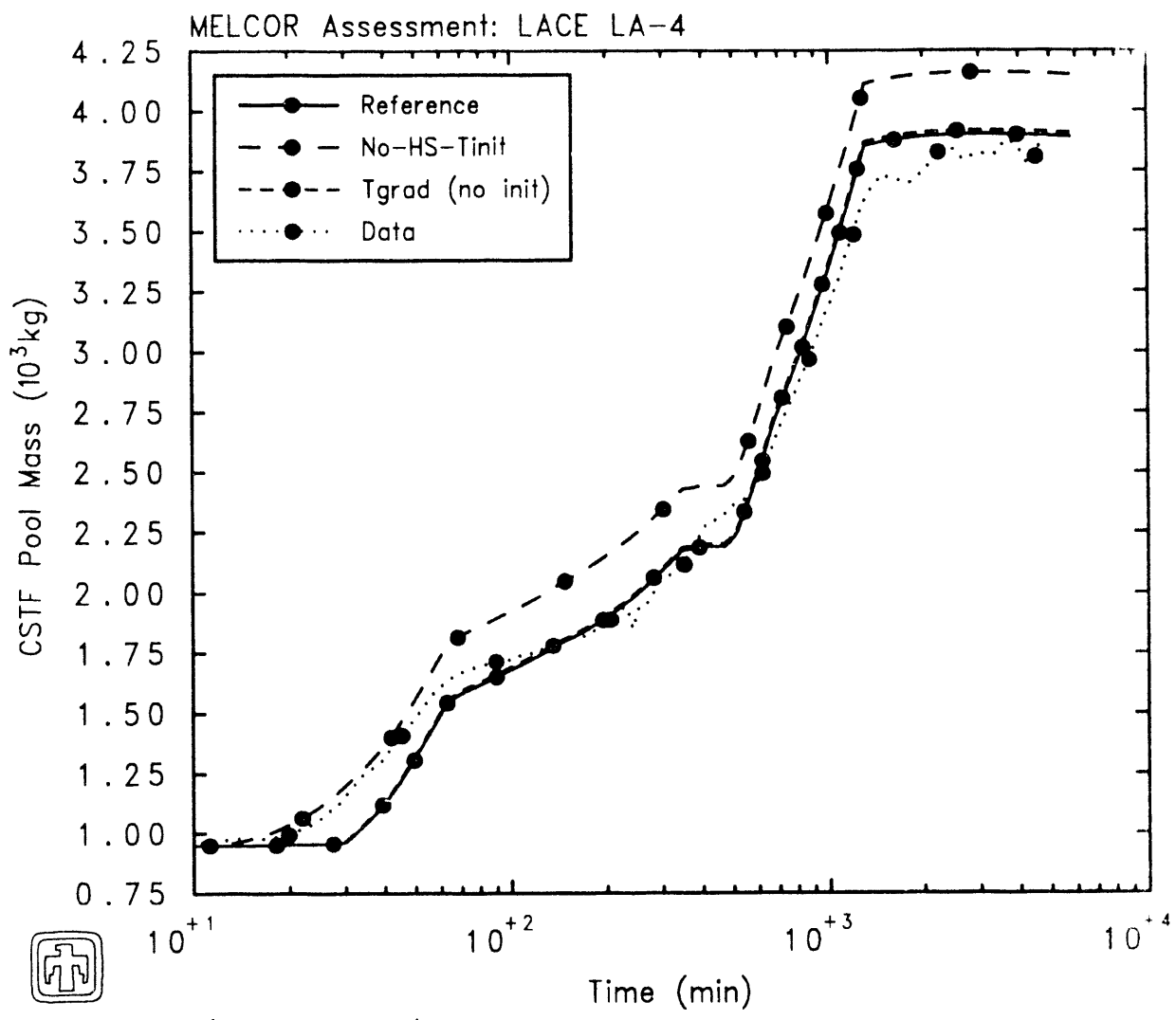
ppm/der is the reference value. Note: all test conditions were in the between 1000 and 10000 ppm/der range. The codebook is a straight extrapolation.

7.2 Condensation on Walls

It is important to note that the significant increase in significant condensation of steam on the walls of the test chamber, subsequent draining of the accumulating liquid down into the liquid pool. Most of the increase in pool liquid mass comes from the condensation of the steam on the walls. Areas of the liquid pool increase due to water's expansion as it warms from the liquid to the steam phase.

The condensation of steam on the walls of the test chamber is a significant factor in the increase in pool liquid mass. The condensation of steam on the walls of the test chamber is a significant factor in the increase in pool liquid mass. The condensation of steam on the walls of the test chamber is a significant factor in the increase in pool liquid mass. The condensation of steam on the walls of the test chamber is a significant factor in the increase in pool liquid mass.

The condensation of steam on the walls of the test chamber is a significant factor in the increase in pool liquid mass. The condensation of steam on the walls of the test chamber is a significant factor in the increase in pool liquid mass. The condensation of steam on the walls of the test chamber is a significant factor in the increase in pool liquid mass.





 LACE LA-4 (2-component)
 G2BKBHN 7/29/91 10:14:33 MELCOR

Figure 7.2.1. Pool Masses - HS Wall Initialization - Condensation Sensitivity Study

es measured pool liquid mass throughout most of the problem. The initial film liquid inventory is not caused simply by a $\Delta T(t=0) \neq 0$, but is due to some quirk in the temperature initialization, because the initial film inventory and subsequent offset in later-time pool liquid mass is not calculated if the MELGEN initialization scheme is bypassed but the initial heat structure temperature gradient calculated by the MELGEN heat structure temperature initialization input manually, as shown in Figure 7.2.1.

There is very little, if any, visible difference in any of the other predicted variables using the different initial heat structure temperatures.

7.3 Radiation Heat Transfer

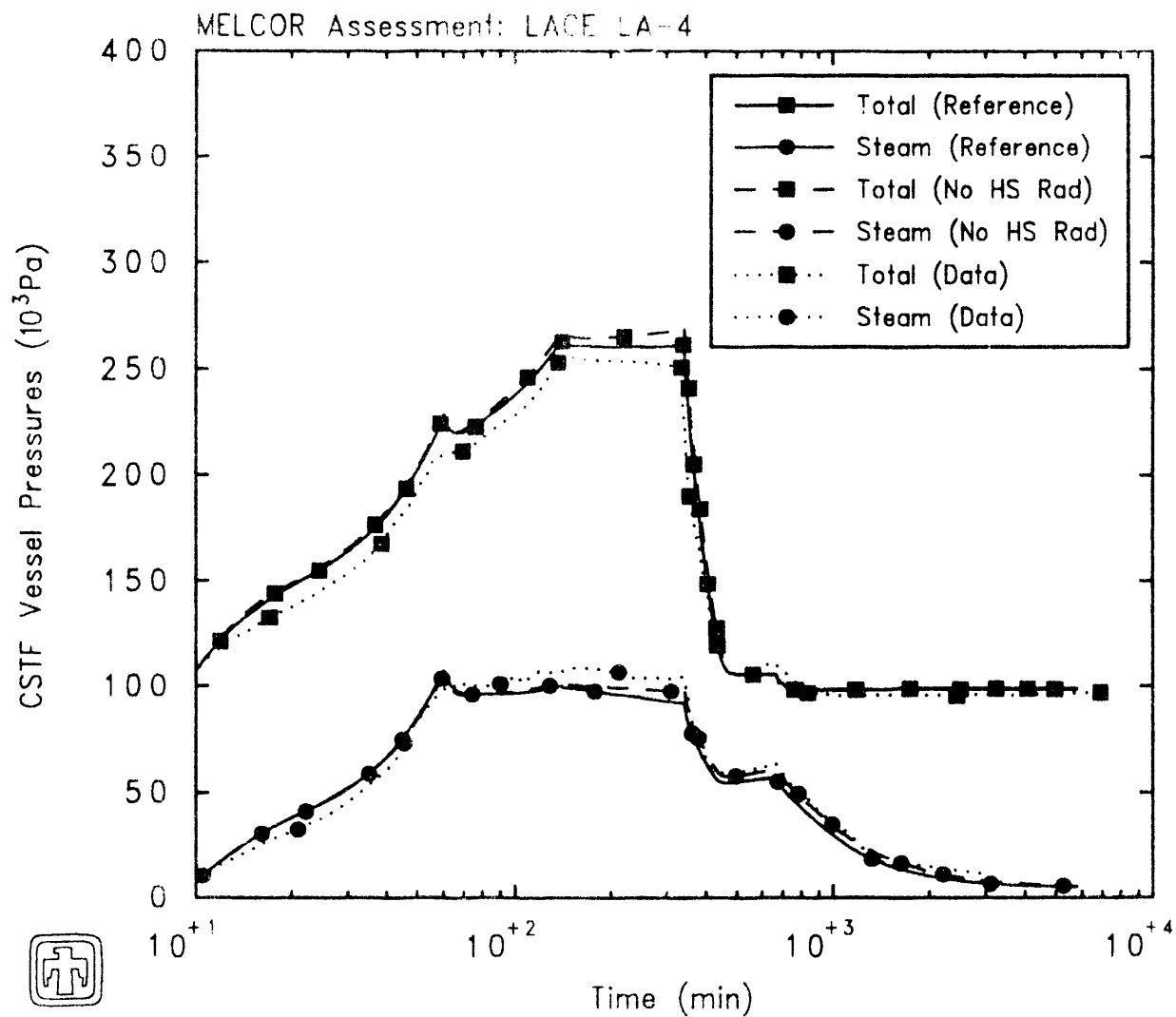
The reference analysis included radiative heat transfer between heat structure surfaces and adjacent control volume atmospheres, with a specified emissivity of 0.9. Radiation was included in most of our MELCOR calculations because the CONTAIN calculations had shown that it has a significant effect on any water droplets suspended in the atmosphere. Normally, at the relatively low temperatures in this experiment, we would assume that radiation was not an important phenomenon and would not include it.

The CONTAIN calculations used an emissivity of 0.85 [9]. The MELCOR calculations used an emissivity of 0.9 instead, because it was quoted in the test data report [5] as the “normal total emissivity of paint”. A calculation was run with the CONTAIN value of 0.85, instead, with no visible differences in predicted results.

(MELCOR does not model structure-to-structure radiative heat transfer in general, only within the COR package, which was not used in these calculations. CONTAIN can include structure-to-structure radiation [7], but that model was not activated in their calculations [9].)

A sensitivity study was done in which no radiative heat transfer was considered. Figure 7.3.1 shows the total and steam partial pressures predicted in the containment vessel with and without radiation heat transfer (together with the corresponding test data); the bulk atmosphere and pool temperatures for these two calculations are compared in Figure 7.3.2. The most visible difference is in the atmosphere temperature, which is as much as 5-10K higher during most of the problem time in the absence of any structure-atmosphere radiative heat transfer. This higher temperature results in a slightly higher total pressure during the steady-state period, but there is very little change in the pool temperature or the steam partial pressure. Wall temperatures in the steel shell increased by 1-2K, while the outside insulation surface temperature was 5-8K higher with no radiation heat transfer allowed; the final pool liquid mass was 70-75kg (~1%) greater when radiative heat transfer was not allowed.

Figure 7.3.3 presents a comparison of the computed masses predicted for the two cases, including the two-component aerosol input model from the reference calculation




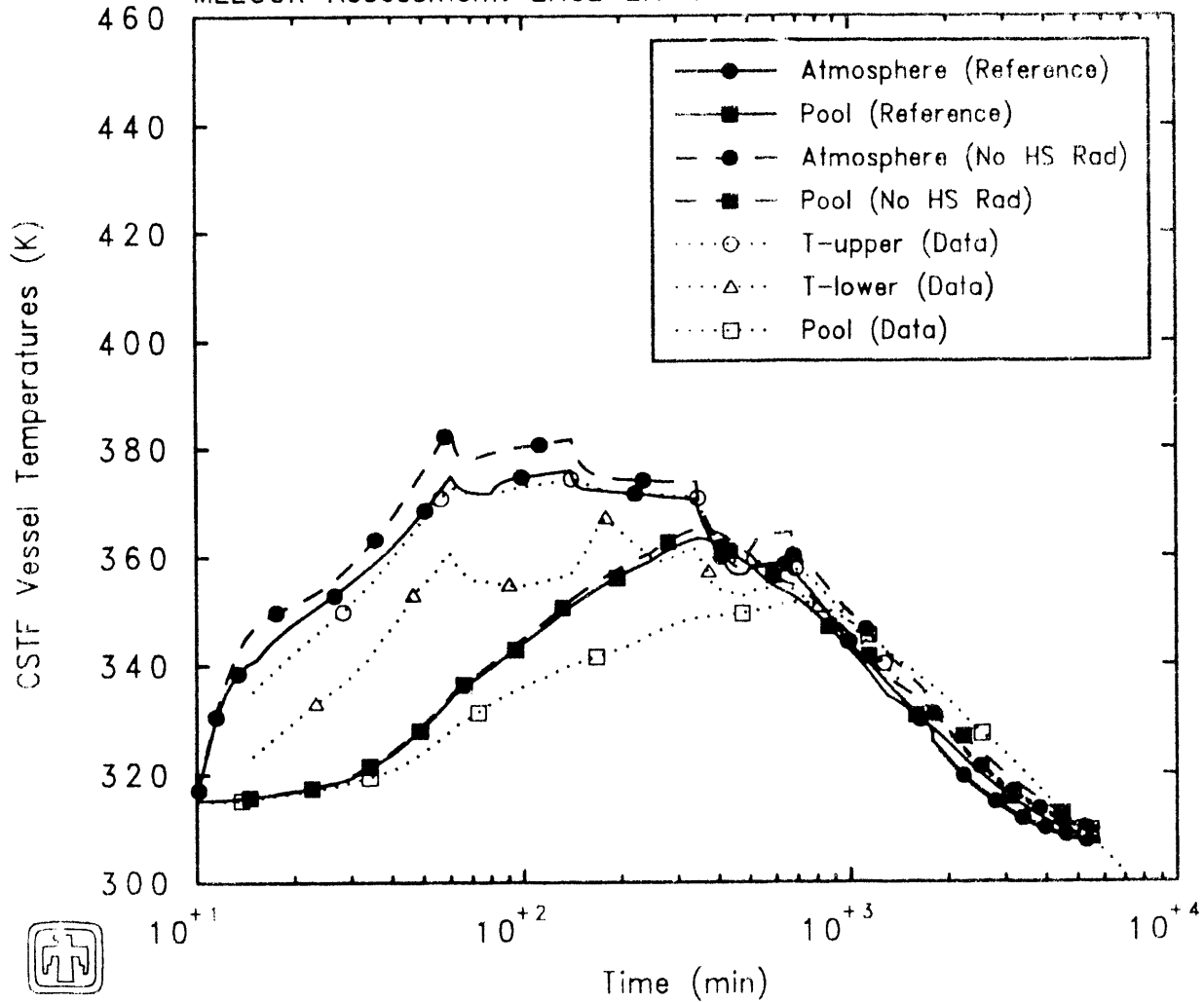

 LACE LA-4 (2-component)
 02BKBHN 7/29/91 10:14:33 MELCOR

Figure 7.3.1. Total and Steam Partial Pressure - HS Radiation Sensitivity Study

MELCOR Assessment: LACE LA-4



LACE LA-4 (2-component)

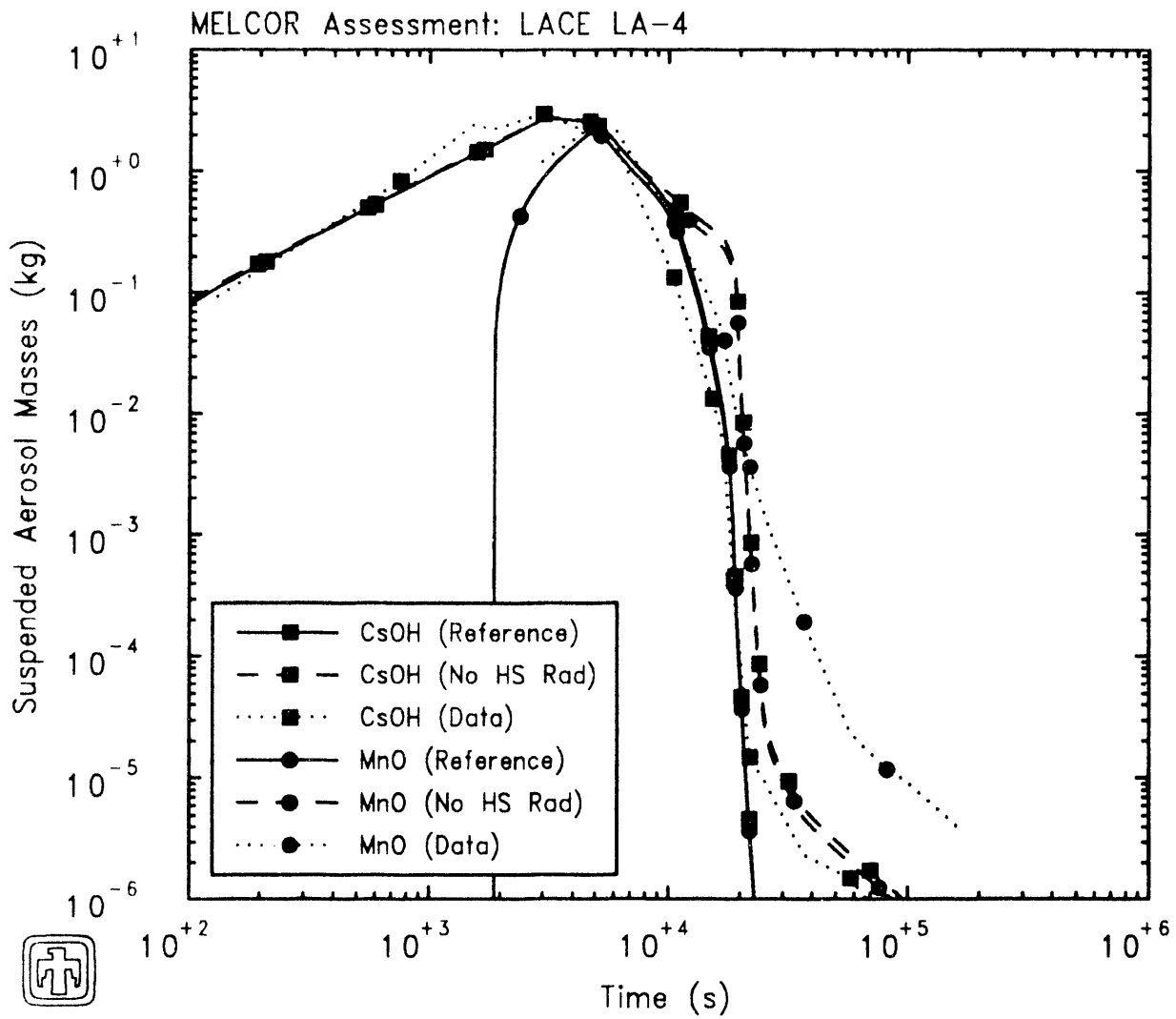
G2BKBHN 7/29/91 10:14:33 MELCOR

with and without radiation, with experimental data. Neglecting radiative heat transfer increased the suspended aerosol masses dramatically, during the steady-state and vent periods (~ 10000 - 20000 s) as well as late in the cooldown period (>30000 s). Figure 7.3.4 shows that the change in suspended aerosol masses is due to very different saturation ratios being calculated with and without atmosphere-structure radiation heat transfer, with corresponding differences in the water aerosol masses. During the steady-state period from ≤ 6000 s to <30000 s, the test vessel atmosphere in the reference calculation with radiative heat transfer is fully saturated, while the sensitivity study with no radiation heat transfer remains subsaturated until ~ 20000 s. That extra period of time when the sensitivity-study calculation remains subsaturated, and when no water aerosol is present, corresponds exactly to the time when the predicted aerosol suspended masses in the sensitivity-study calculation decline much more slowly than seen either in the test data or in the reference calculation; once the calculation with no radiative heat transfer predicts fully saturated conditions, at ~ 20000 s, the suspended aerosol masses drop as rapidly as earlier in the reference calculation.

The aerodynamic mass median diameters and the geometric standard deviations predicted in this sensitivity analysis are compared to the reference calculation results and to values derived from experimental observations in Figure 7.3.5, while the mass distributions of the three aerosol species at ≥ 11000 s (when the calculations with and without atmosphere-structure radiation heat transfer give very different results) are compared in Figure 7.3.6. These two figures show that the prolonged subsaturated atmosphere conditions predicted in the absence of radiative heat transfer, during the ~ 6000 - 20000 s period, result in no water aerosol particles being present and, therefore, no condensation onto and subsequent rapid growth of the injected aerosol species particles; this results in generally smaller aerosol particles which settle out of the atmosphere more slowly.

Table 7.3.1 summarizes the measured post-test aerosol locations and the corresponding predictions from these two calculations. There is much more aerosol leakage with no radiation assumed, because of the larger suspended aerosol masses predicted during the late, cooldown, period in that calculation. There is not much qualitative change in deposited or plated masses predicted with and without radiation, and only minor quantitative differences.

Finally, it should be noted that the inclusion or neglect of atmosphere-structure radiation heat transfer only produced the expected difference in the predicted aerosol response in those calculations where the water was modelled as a separate aerosol component. When water was included in the same, single, aerosol component as the two injected aerosol species, the same differences in thermal hydraulic response were present but no differences were seen in the predicted aerosol response because the growth of CsOH-MnO particles due to water condensation cannot be correctly modelled with only one aerosol component in any case (as discussed in Section 6.2).



LACE LA-4 (2-component)

G2BKBHN 7/29/91 10:14:33 MELCOR

Figure 7.3.3. Suspended Aerosol Masses - HS Radiation Sensitivity Study

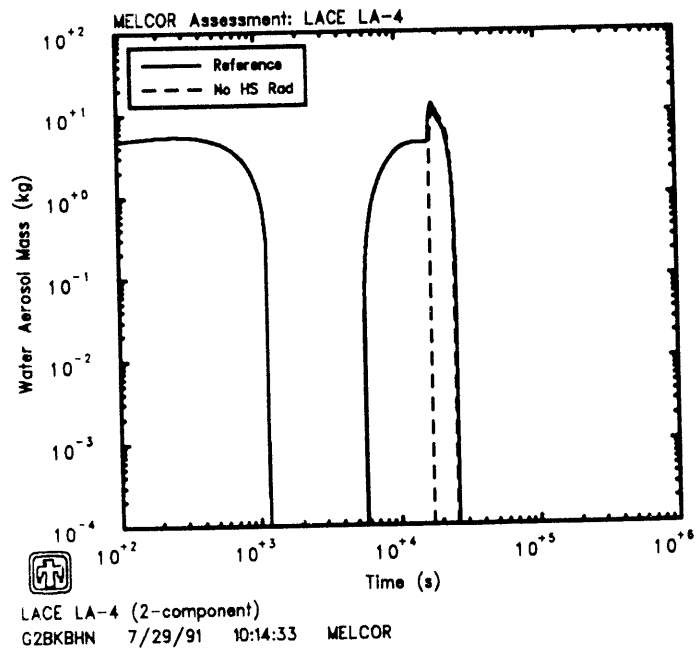
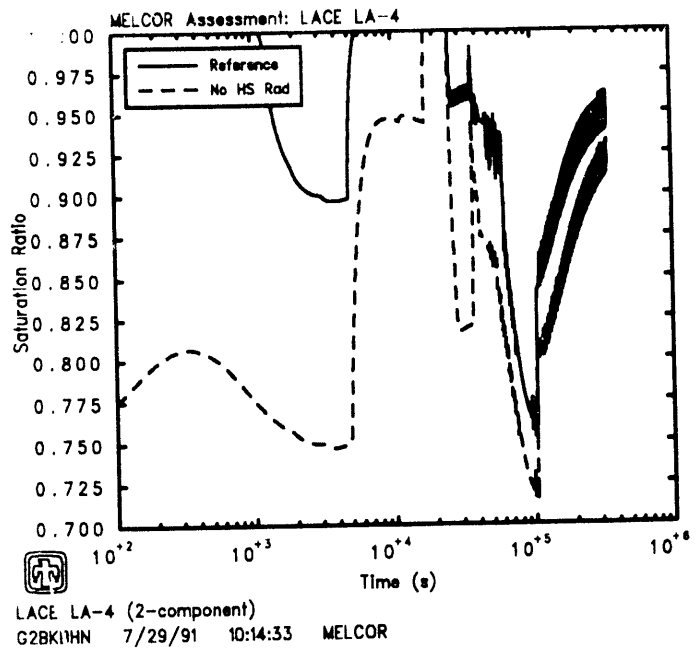


Figure 7.3.4. Saturation Ratio (top) and Water Aerosol Mass (bottom) - HS Radiation Sensitivity Study

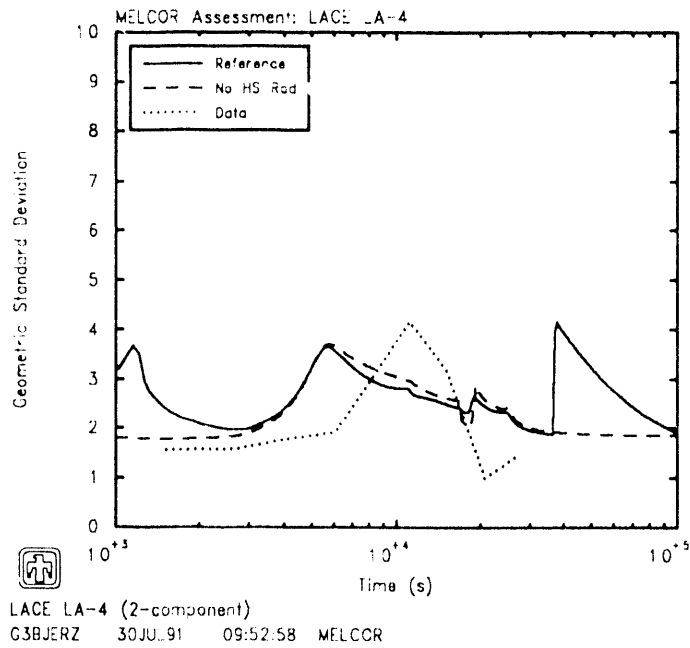
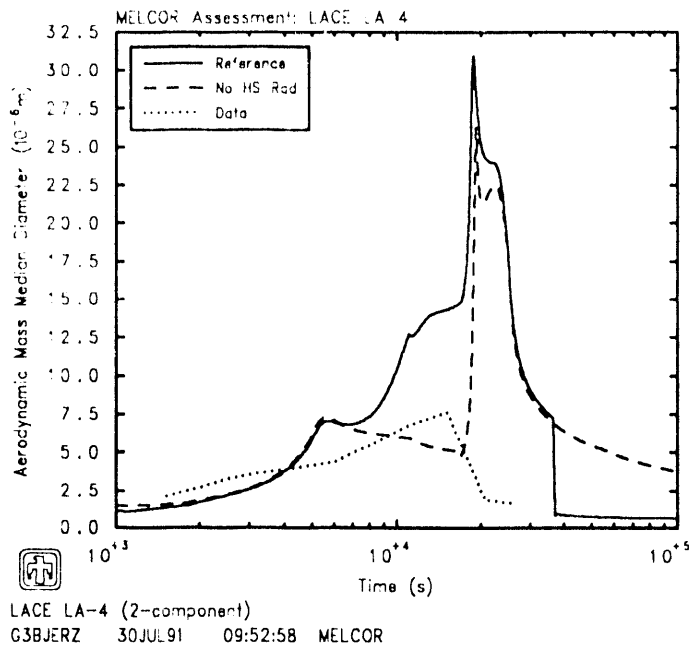


Figure 7.3.5. Aerodynamic Mass Median Diameter (top) and Geometric Standard Deviation (bottom) for Suspended Aerosols - HS Radiation Sensitivity Study

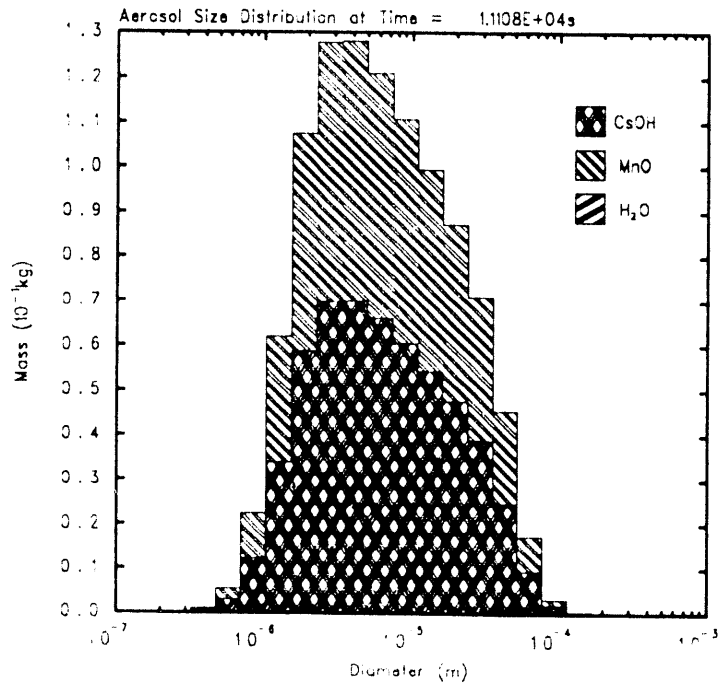
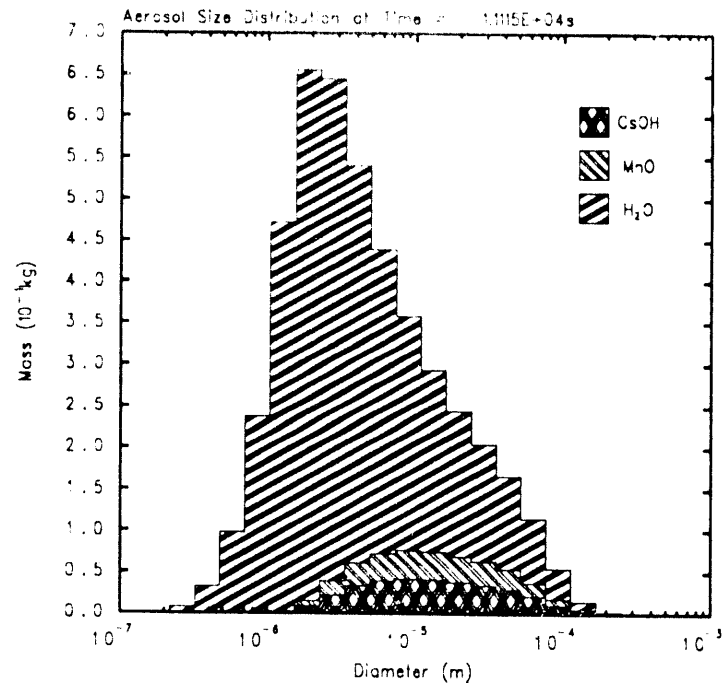


Figure 7.3.6. Size Distribution at Time = 1.1115E+04s for Suspended Aerosols with (top) and without (bottom) Radiation - HS Radiation Sensitivity Study

Table 7.3.1. Post-Test Aerosol Locations - HS Radiation Sensitivity Study

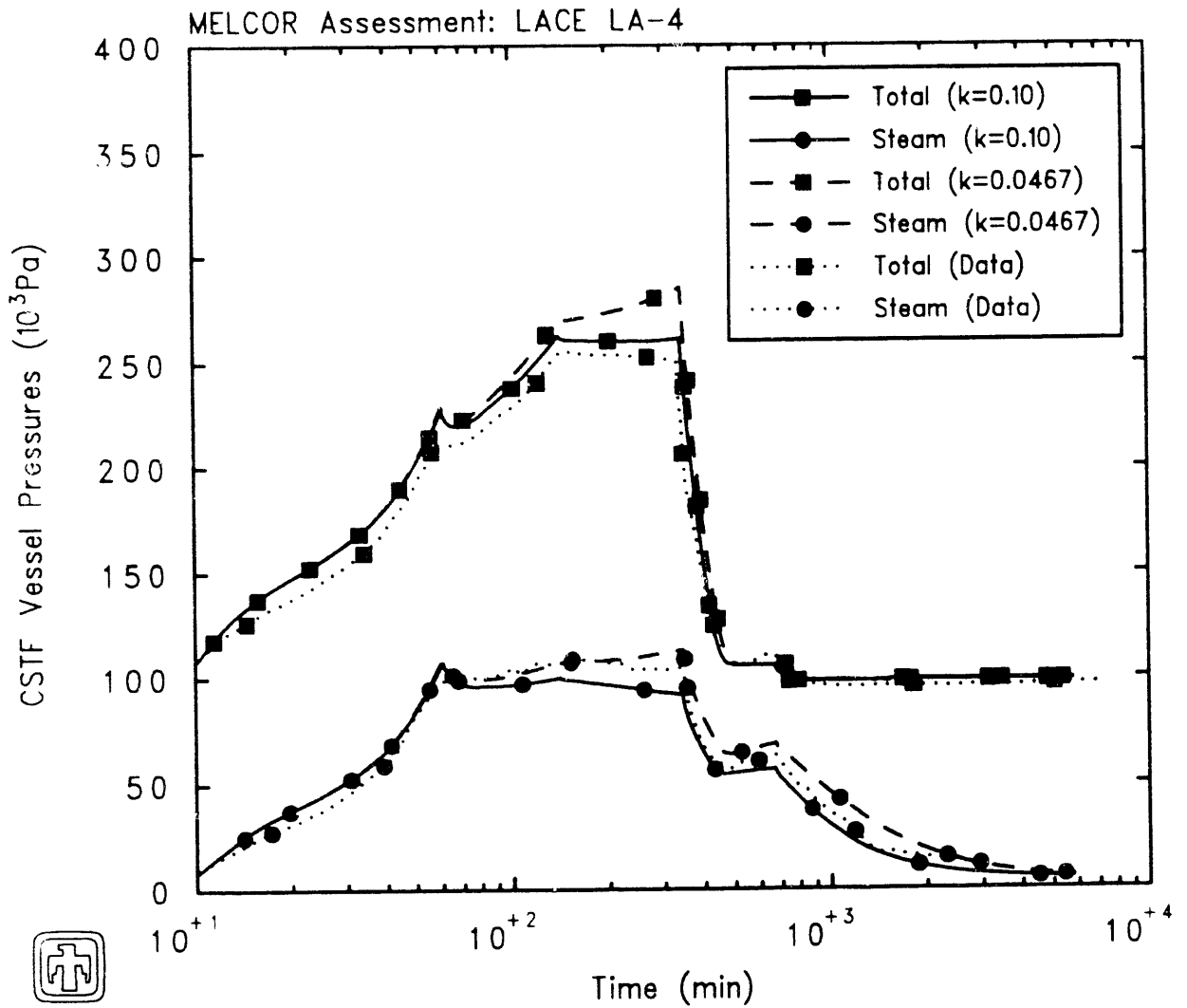
Aerosol Species	Location	Test Data (kg)	Code (kg)	
			Reference	No HS Radiation
CsOH	Settled	2.563	2.615	2.523
	Plated	0.304	0.230	0.235
	Leaked	0.007	0.002	0.088
MnO	Settled	1.927	2.153	2.069
	Plated	0.228	0.117	0.128
	Leaked	0.101	0.001	0.073
Sum	Settled	4.490	4.768	4.592
	Plated	0.532	0.347	0.363
	Leaked	0.108	0.003	0.161

7.4 Insulation Thermal Conductivity

The thermal conductivity of the fiberglass insulation is cited in the test documentation as nominally $0.0467\text{W}/\text{m}\cdot\text{K}$ [5]. However, that report does mention some degradation in the insulation visible, and a value of $0.10\text{W}/\text{m}\cdot\text{K}$ was used in the CONTAIN analysis [8]. That higher value was used in the reference MELCOR calculation. A sensitivity study was done with the lower, original value of thermal conductivity of the fiberglass, to confirm this selection.

The total and steam partial pressures predicted in the containment vessel for the two different values of insulation thermal conductivity are compared in Figure 7.4.1 (together with the corresponding test data). Both the total test vessel pressure and the steam partial pressure are progressively, significantly, higher for the “better” insulation during the steady state period; the steam partial pressure is also higher during the vent and cooldown periods with the lower value of insulation thermal conductivity.

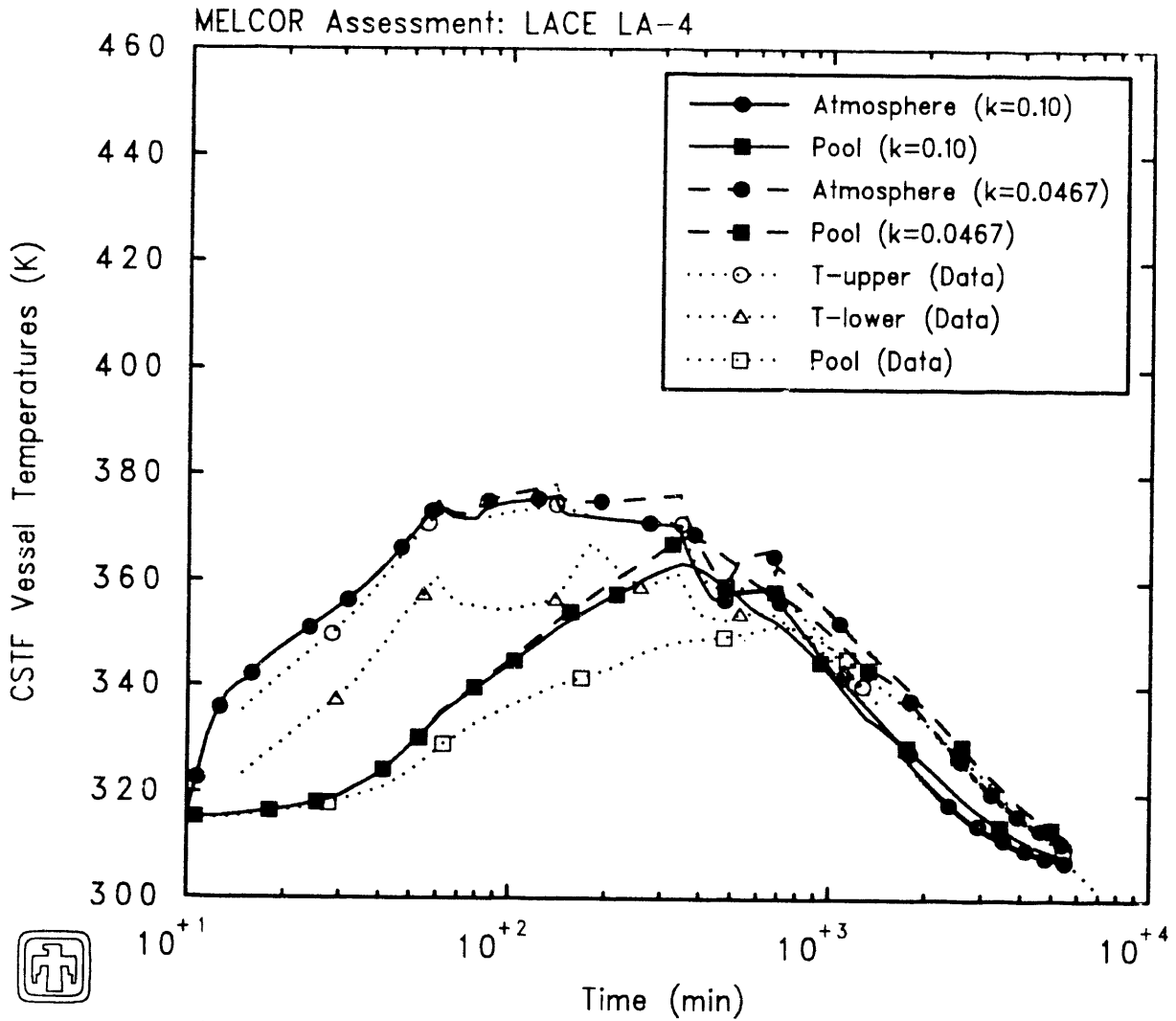
Figure 7.4.2 compares the bulk atmosphere and pool temperatures calculated for the two values of insulation thermal conductivity. Both temperatures are 1-5K greater for the lower thermal conductivity value during the steady state period, and 5-10K higher during the vent and cooldown period. (Wall temperatures in the steel containment box or similar change in temperature, while the outside insulation surface temperature was generally $\sim 10\text{K}$ higher with the “better” insulation; the final pool temperature was $\sim 200\text{g}/\text{m}^2$ or less than in the reference calculation.)



LACE LA-4 (2-component)

BKBHN 7/29/91 10:14:33 MELCOR

Figure 7.4.1. Total and Steam Partial Pressures - Insulation Conductivity Sensitivity Study



LACE LA-4 (2-component)

G2BKBHN 7/29/91 10:14:33 MELCOR

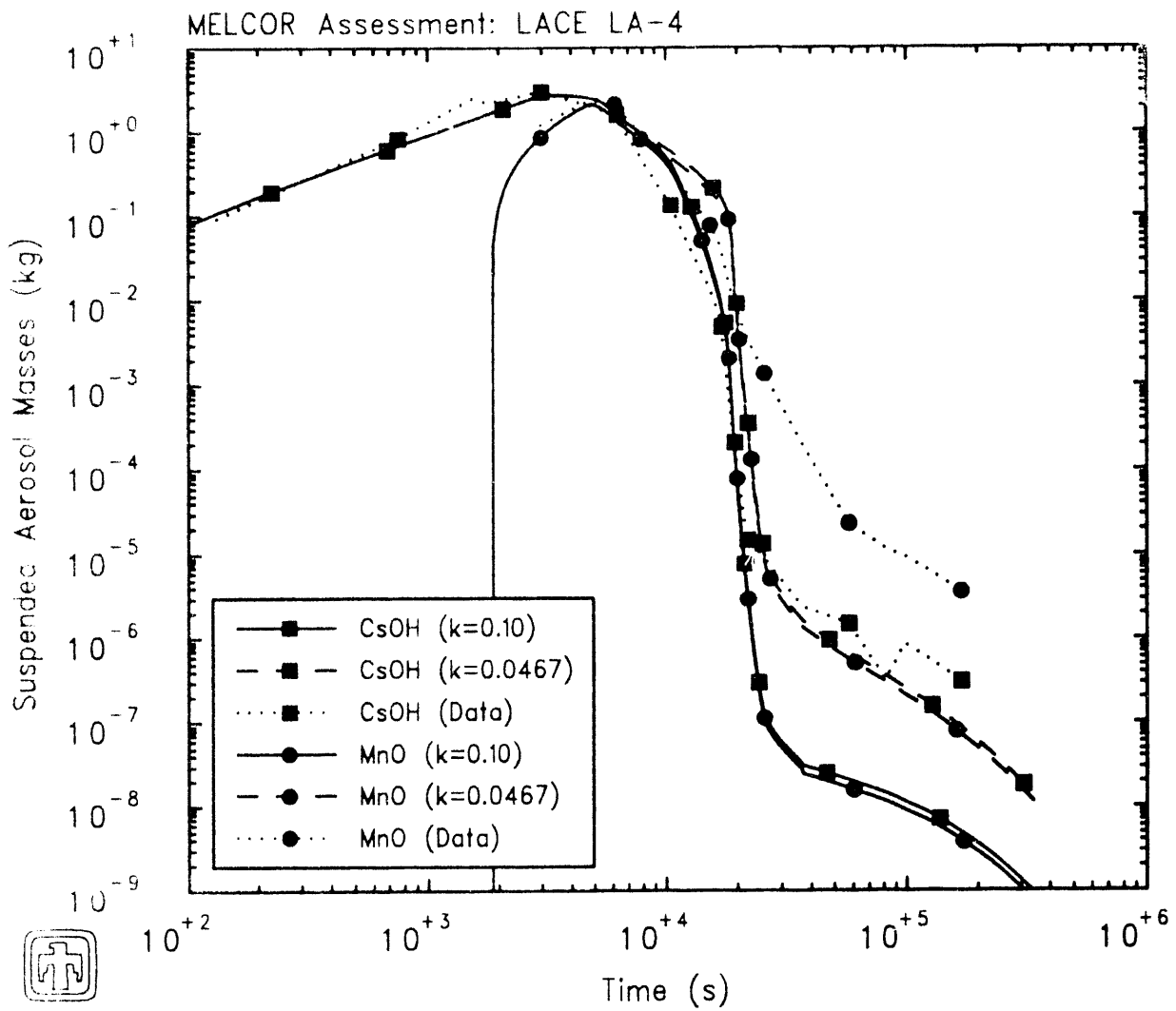
Figure 7.4.2. Atmosphere and Pool Temperatures - Insulation Conductivity Sensitivity Study

The suspended masses predicted for the two aerosols in this sensitivity study are given in Figure 7.4.3, together with experimental data. Using the lower, cited value for insulation thermal conductivity again resulted in a dramatic increase in the suspended aerosol masses during the ~ 10000 - 20000 s period. Figure 7.4.4 shows that the change in suspended aerosol masses is not due to very different saturation ratios being calculated, as occurred for similar suspended aerosol mass differences predicted with and without atmosphere-structure radiation heat transfer (discussed in the previous subsection, 7.3). Instead, the comparison in the lower half of Figure 7.4.4 indicates that the differences predicted in CsOH and MnO aerosol suspended masses are due to very different amounts of water aerosol present for condensation in these two calculations during the time period in question.

The aerodynamic mass median diameters and the geometric standard deviations are contrasted in Figure 7.4.5, and the mass distributions of the three aerosol species at ≥ 11000 s in Figure 7.4.6. The average diameter comparison shows that the CsOH and MnO particles are smaller during the ~ 6000 - 20000 s period, and hence settle out more slowly; the size distribution confirms that less water aerosol is present during this time, resulting in less condensation and slower particle growth. Once the water aerosol mass becomes equal for these two calculations (at ~ 20000 s), the CsOH-MnO aerosol component particles grow to about the same size and settle out at about the same rate.

Table 7.4.1 summarizes the measured post-test aerosol locations and the corresponding predictions from these two calculations. There is once again more aerosol leakage in the calculation with larger suspended aerosol masses predicted during the late, cooldown, period in that calculation. There is not much qualitative change in deposited or plated masses predicted with and without radiation, and only minor quantitative differences.

Again, as with the atmosphere-structure radiative heat transfer sensitivity study, the different values of insulation thermal conductivity only produced differences in the predicted aerosol response in those calculations where the water was modelled as a separate aerosol component.



LACE LA-4 (2-component)

G. KBHN 7/29/91 10:14:33 MELCOR

Figure 7.4.3. Suspended Aerosol Masses - Initiation Conductivity Sensitivity Study

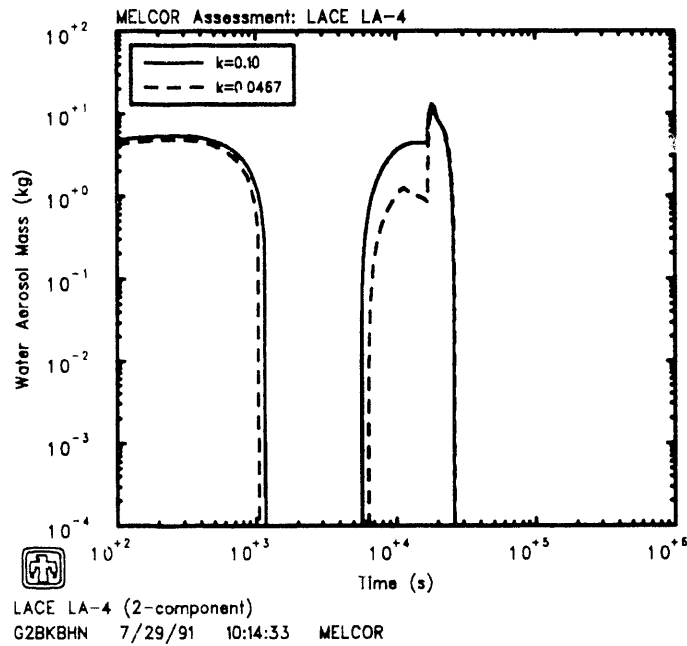
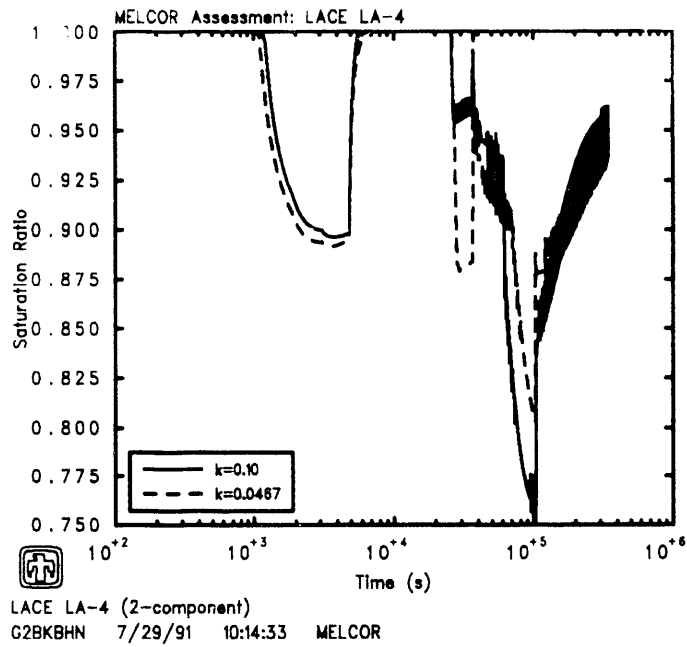


Figure 7.4.4. Saturation Ratio (top) and Water Aerosol Mass (bottom) Incineration Conductivity Sensitivity Study

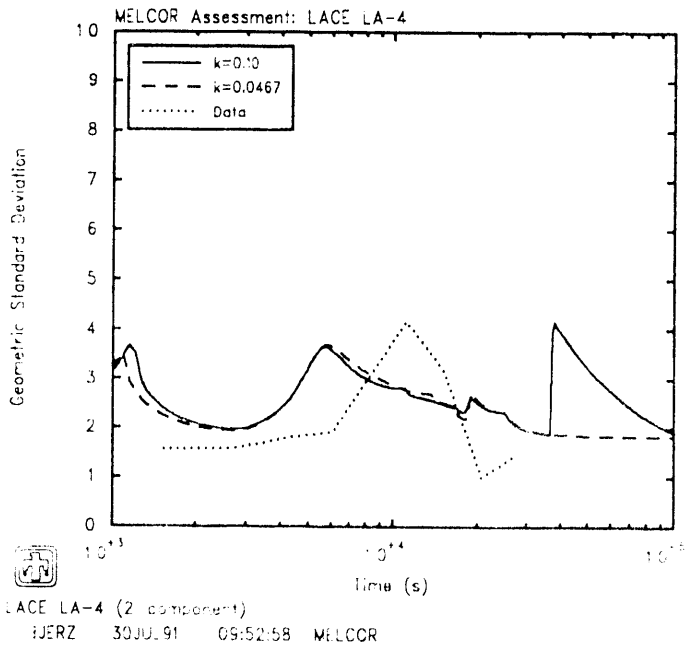
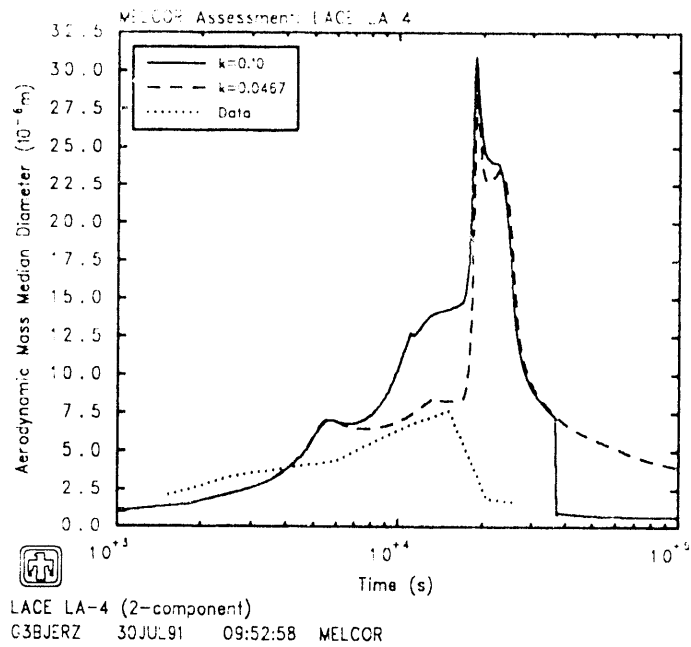


Figure 7.4.5. Aerodynamic Mass Median Diameter (top) and Geometric Standard Deviation (bottom) for Suspended Aerosol - Inactivation Conductivity Sensitivity Study

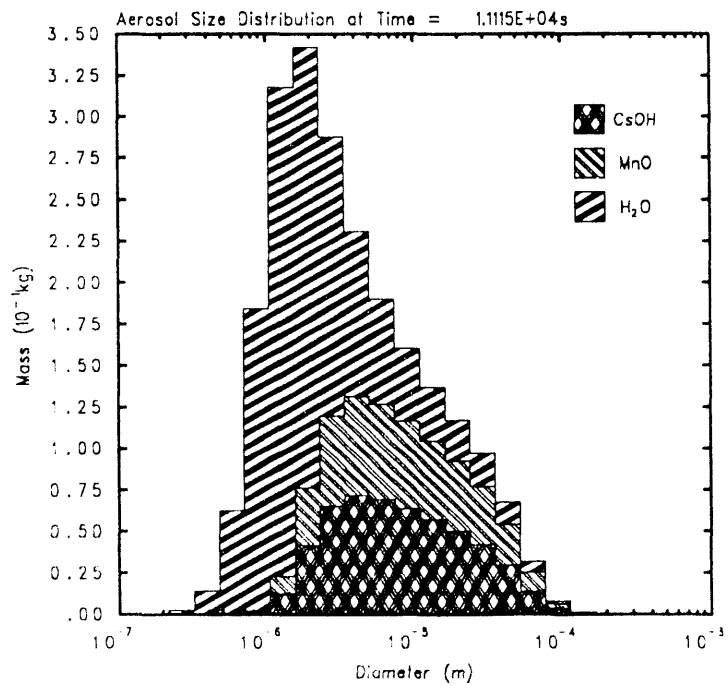
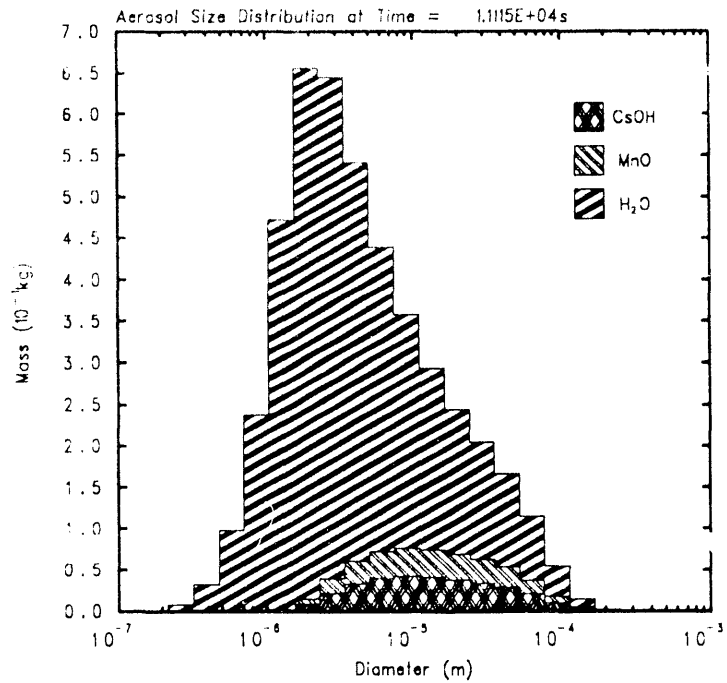


Figure 7.4.6. Size Distribution for Suspended Aerosols at ~11000s with Increased (top) and Cited (bottom) Insulation Thermal Conductivity - Insulation Conductivity Sensitivity Study

Table 7.4.1. PostTest Aerosol Locations – Insulation Thermal Conductivity Sensitivity Study

Aerosol Species	Location	Test Data (kg)	Code (kg)	
			Reference ("k=0.10")	Cited k ("k=0.0467")
CsOH	Settled	2.563	2.615	2.610
	Plated	0.304	0.230	0.193
	Leaked	0.007	0.003	0.044
MnO	Settled	1.927	2.153	2.135
	Plated	0.228	0.117	0.099
	Leaked	0.101	0.001	0.037
Sum	Settled	4.490	4.768	4.745
	Plated	0.532	0.347	0.292
	Leaked	0.108	0.003	0.081

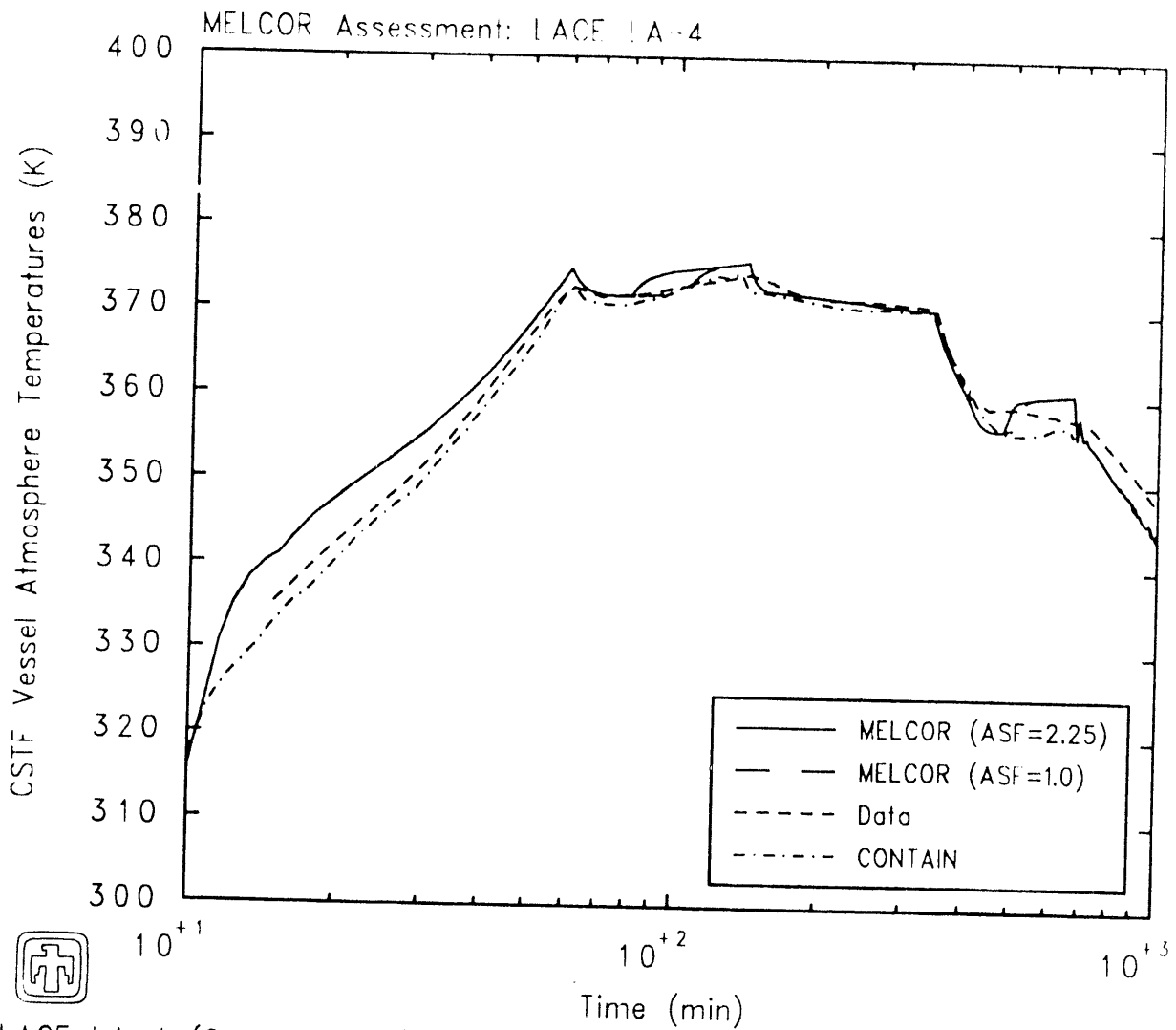
8 Comparison to CONTAIN

The reference MELCOR calculation described in Section 4 has been compared to a similar calculation [8] done recently with the CONTAIN code [7]. The referenced paper contains a number of post-test analyses; the one used for this comparison with MELCOR is the "Best Estimate with Insoluble Aerosol" calculation, even though a separate CONTAIN analysis presented in reference [7] ("Best Estimate with Soluble Aerosol") was in much better agreement with data during most of the experiment. That calculation included the hygroscopic effect for the CsOH aerosol; because that effect is not represented in MELCOR those results were not used for this code-to-code comparison.

As in our reference MELCOR calculation, the CONTAIN calculation used the higher insulation thermal conductivity, and included radiation heat transfer, but did not include any hygroscopic effects. Both should be considered non-blind, posttest analyses where the test data were available for comparison during the calculations. Because the reference MELCOR calculation was done with an agglomeration shape factor set to 2.25 (from the MELCOR and CONTAIN ABCOVE analyses [2]) while the CONTAIN LA4 calculation used a default agglomeration shape factor of 1.0 [9], the CONTAIN results are compared also to the results of the MELCOR sensitivity study calculation which used the default agglomeration shape factor of 1.0 (described in Section 6.4).

Figure 8.1 compares the test vessel pressures calculated by MELCOR and by CONTAIN, and includes the corresponding experimental data. (The time period plotted in these crossplots is shorter than that shown in the reference MELCOR calculation results in Section 4 because the CONTAIN calculation was not run to the end of the cooldown period, only to the end of the vent period.) The CONTAIN results are in better agreement with data than the MELCOR results during the early aerosol injection period, but in general the CONTAIN and MELCOR results are very similar to each other. The MELCOR results obtained using the two different ASF values are indistinguishable in this crossplot.

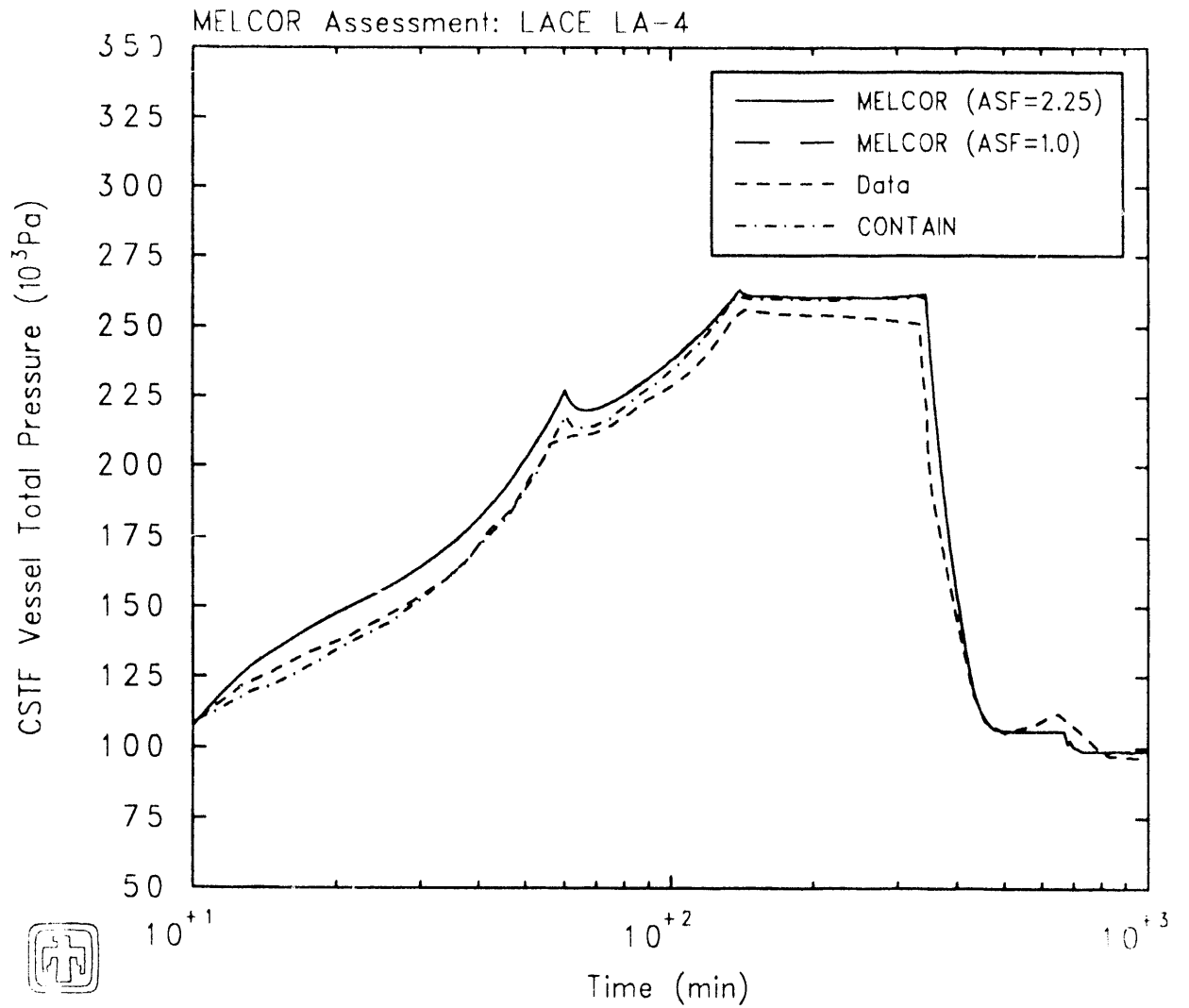
The atmosphere temperatures predicted by the two codes are given in Figure 8.2, together with the measured data for the upper part of the test vessel. (As discussed in Section 4, two distinct regions, or convection cells, were observed in this experiment: the upper region or cell was characterized by relatively uniform temperatures and included all the volume above the elevation of the steam outlet pipe, or about 95% of the total volume.) The CONTAIN result is again in better agreement with test data, especially early in the transient, but both codes give quite acceptable agreement with data during most of the test period, including the steady-state and vent periods of most interest. The MELCOR results obtained using the two different ASF values are almost indistinguishable in this crossplot, except for a brief divergence between ~75min and ~110min.



LACE LA-4 (2-component)

03BJERZ 30JUL91 09:52:58 MELCOR

Figure 8.1. Total Pressure - MELCOR - CONTAIN Comparison



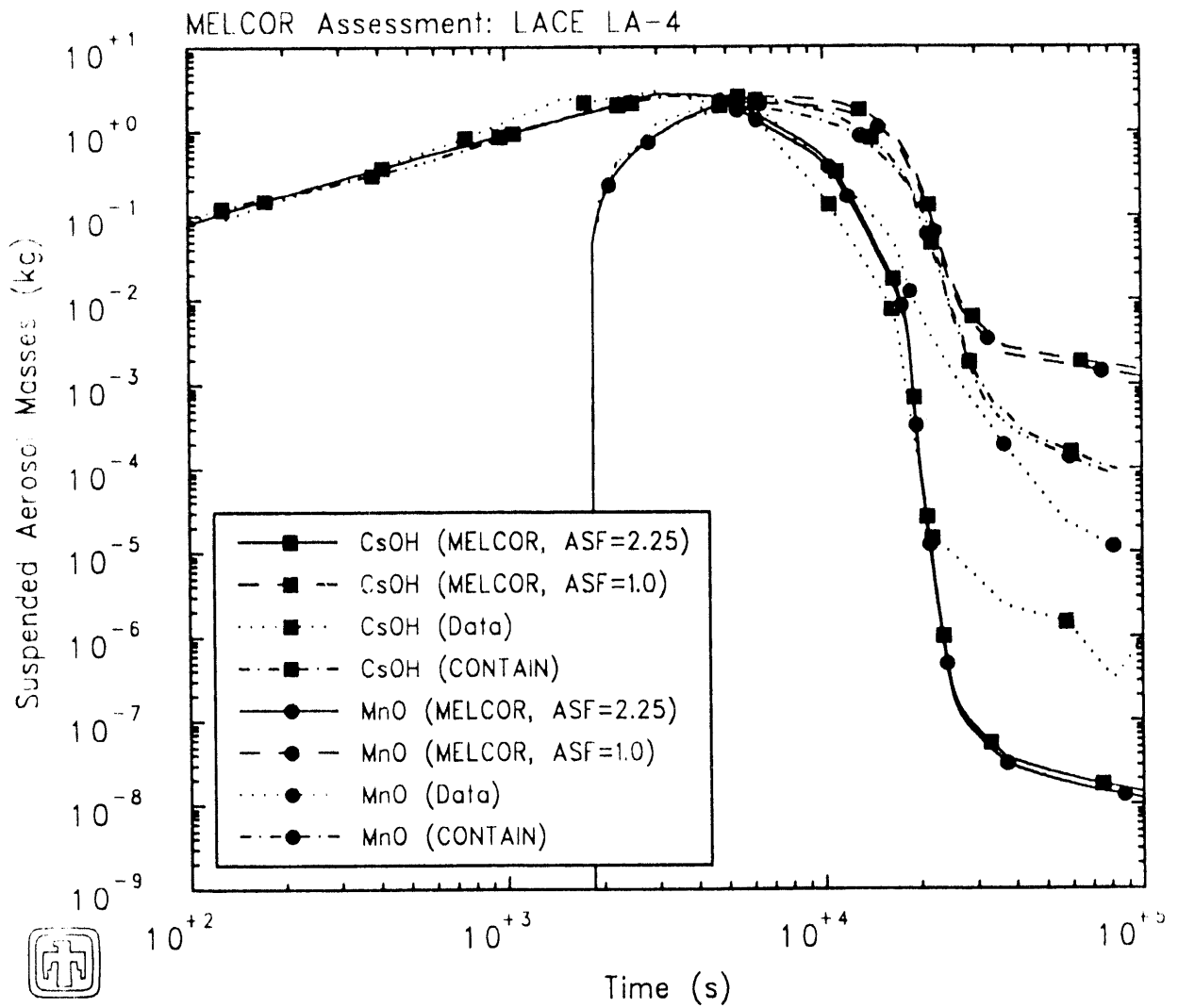
LACE LA-4 (2-component)
 G3BJERZ 30JUL91 09:52:58 MELCOR

Figure 8.2. Atmosphere Temperatures - MELCOR - CONTAIN Comparison

Despite the very similar thermal-hydraulic conditions being calculated, the results for the suspended aerosol masses are quite different for MELCOR and for CONTAIN during that steady-state and vent period, as illustrated in Figure 8.3. The results predicted by both codes are very similar to each other and to data during the aerosol injection periods (< 5000 s). The suspended aerosol masses calculated by CONTAIN (without hygroscopic effects) for both species are substantially higher than either test data or the MELCOR reference calculation results from ~ 6000 s through the end of the period analyzed by both codes; however, the MELCOR results using the same (default) agglomeration shape factor as in the CONTAIN analyses are very similar to the CONTAIN results for both aerosol species during the steady-state and vent periods (6000-20000s), before diverging from the CONTAIN predictions by about an order of magnitude during the last, cooldown, test period.

The saturation ratios and water aerosol masses suspended in the test vessel atmosphere predicted by the two codes are crossplotted in Figure 8.4. The differences during the aerosol injection periods ($t \leq 5000$ s) do not result in any differences in suspended aerosol masses, as seen in Figure 8.3. The rapid dropoff in suspended aerosol masses in the reference MELCOR calculation at ~ 10000 s, not seen in the CONTAIN calculation, occurs at a time when both codes predict a saturation ratio of 1. However, the reference MELCOR calculation (with an agglomeration shape factor of 2.25) predicts lower water aerosol masses during the time of interest (~ 10000 - 17000 s) than either CONTAIN or MELCOR using the default agglomeration shape factor, corresponding to more water condensation onto, growth of, and settling of the injected aerosols. The water aerosol mass predicted during the steady-state and early vent periods in the MELCOR sensitivity study calculation using the default agglomeration shape factor agrees very well with the corresponding CONTAIN result using the same default agglomeration shape factor, before diverging during the second half of the vent period. That late-time divergence in water aerosol masses corresponds to the divergence in suspended aerosol masses, and corresponds to different saturation ratios predicted in the ~ 25000 - 35000 s period, which in turn is probably due to different thermodynamic assumptions on how to treat excess water droplets in a rapidly depressurizing atmosphere.

Figure 8.5 shows the aerosol masses in each of the size sections for the reference MELCOR calculation and for the sensitivity study in which the default agglomeration shape factor is used at ~ 11000 s when the aerosol particles are settling out during the steady-state period, together with a corresponding plot for the CONTAIN aerosol size distribution at a similar time, taken from [8]. (The CONTAIN plots in [9] have no explicit ordinate values given to allow use of and comparison to proprietary data in a open publication.) As expected from the comparisons in Figures 8.3 and 8.4, the CONTAIN aerosol component size distribution is qualitatively very similar to that predicted using the default agglomeration shape factor in MELCOR, and both are quite different from the size distribution in the reference MELCOR calculation at



LACE LA-4 (2-component)

03:07:23 30JUL91 09:52:58 MELCOR

Figure 8.3. Suspended Aerosol Masses - MELCOR - CONTAIN Comparison

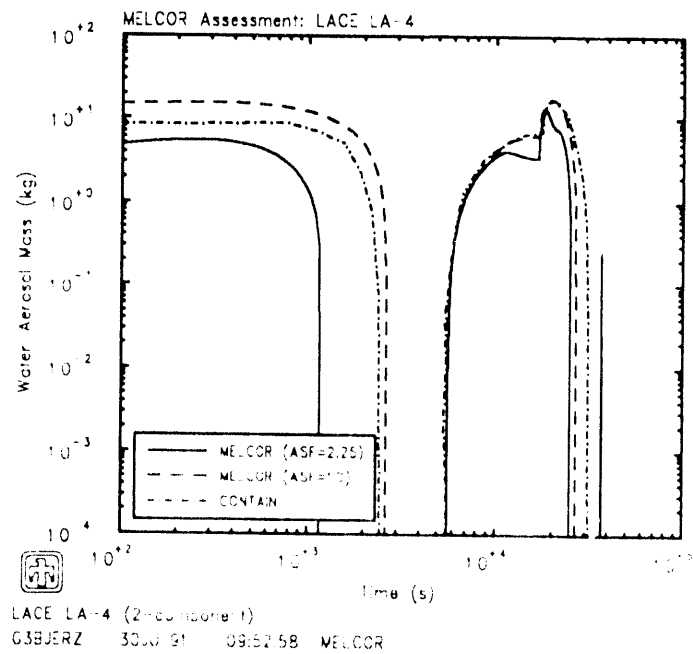
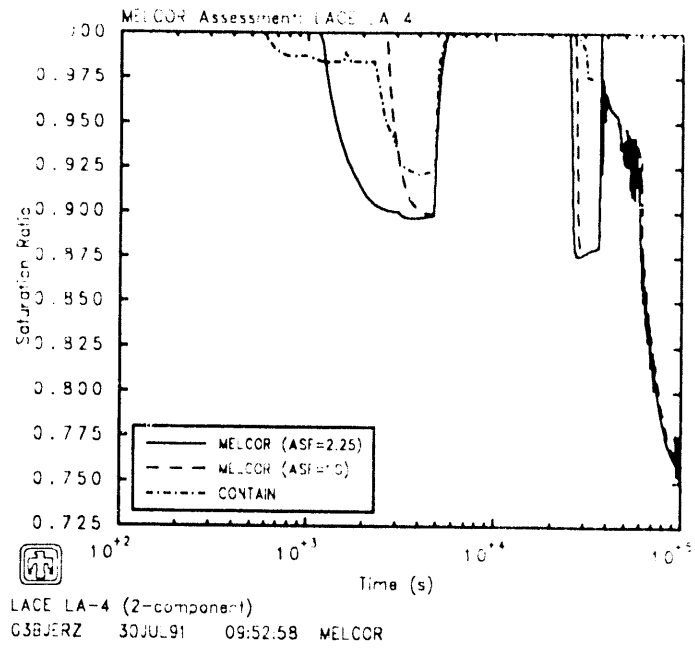


Figure 8.4. Saturation Ratio (top) and Water Aerosol Mass (bottom) for Suspended Aerosols - MELCOR - CONTAIN Comparison

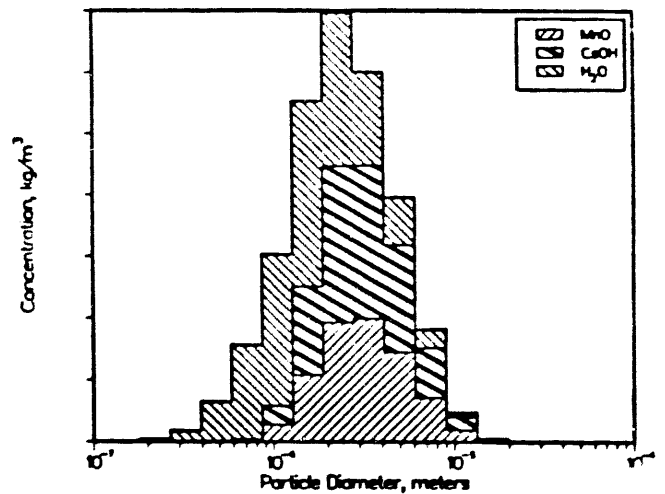
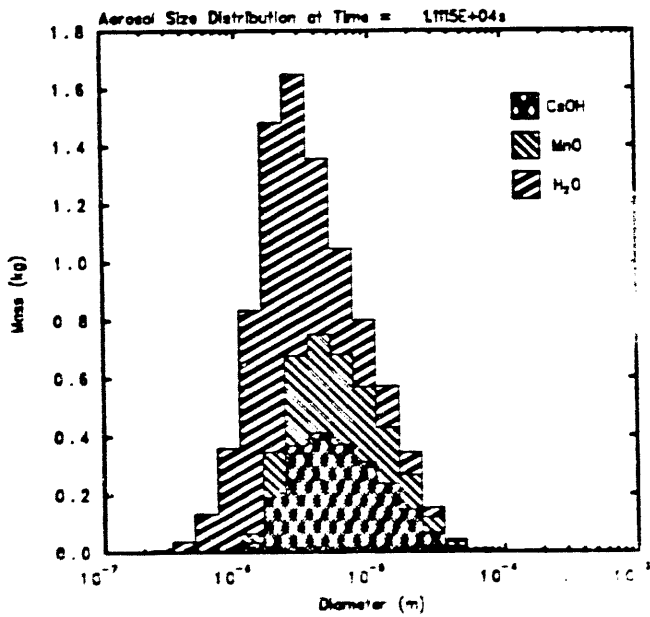
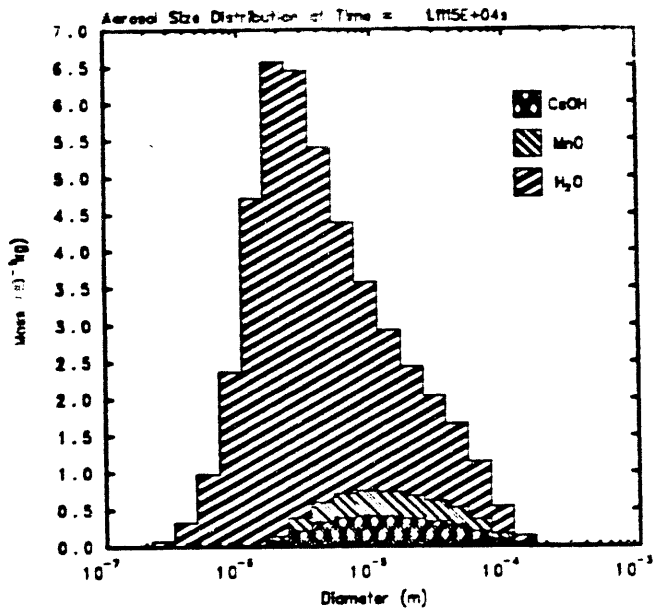


Figure 10. CONTAIN Prediction of Aeroseol Concentration at 10440 seconds (Insoluble, Fixed Grid)

Figure 8.5. Size Distributions for Suspended Aerosols at ~11000s for Reference Calculation (upper left), Default Agglomeration Shape Factor (lower left) and at ~10000s from CONTAIN (middle right) - MELCOR-CONTAIN Comparison

MELCOR and CONTAIN are known to give essentially identical results for suspended aerosol masses, in excellent agreement with test data, in the dry ABCOVE series of experiments done in the same test facility as the "wet" LACE experiments [2]. This comparison shows that, when the same input parameter values are used, MELCOR and CONTAIN give very similar results for suspended aerosol masses in the "wet" LACE LA4 experiment. The minor differences visible are most likely attributable to differences in thermal/hydraulics, particularly in treatments of condensation and transient supersaturated conditions.

9 Code Limitations Identified

Currently in MELCOR, aerosol sectional data are not readily available as either control or plot variables, and are only partially available as optional output variables. In particular, the mass median diameter of the aerosol size distribution was identified as a variable of interest in the ABCOVE aerosol tests analyzed during the 1986 MELCOR validation effort [2], and requested to be made available as an output variable back then. This option had not yet been added when these LACE LA4 assessment analyses were begun, but was added by the developers during this study.

As discussed in Sections 4 and 6.1, a sensitivity coefficient has recently been added to MELCOR, for this analysis, in which the degree to which aerosols drain with the liquid film can be adjusted. Set to 1.0, the default MELCOR treatment discussed above is maintained. Set to 0.0, no aerosol is assumed removed by draining film. The latter allows the effect of aerosol "washing-off" on the plated aerosol masses to be evaluated.

As mentioned in Section 3, a special code mod was added to provide the AMMD and GSD variables on the plot file for each aerosol component in each control volume, together with corresponding "wet" and "dry" composite values.

10 Summary and Conclusions

MELCOR was able to calculate most of the thermal/hydraulic and aerosol response phenomena observed during the LACE LA4 experiment. The lack of any hygroscopic effects in the MELCOR aerosol treatment was visible mostly as the lack of any calculated difference in the behavior of the hygroscopic CsOH and the nonhygroscopic MnO aerosols. MELCOR predicted aerosol particles generally larger than measured, which then settled faster than observed, and consequently less suspended aerosols were leaked and/or plated in the calculation than in the experiment.

The results strongly indicate that water should be modelled as a separate aerosol component, and that more sections (size bins) than the MELCOR default should be used despite the extra cost. Including atmosphere-structure radiative heat transfer, even at the relatively low temperatures (300-400K) characteristic of this test, produced better agreement with data, as did using a detailed volume-altitude table reflecting the differences in sump pool liquid surface area with elevation in the elliptical lower head. There was a strong effect of whether plated aerosol mass was allowed to wash off heat structures with condensate films draining down into the pool. The suspended aerosol results depended most strongly on the value used for the agglomeration shape factor, with a much weaker (but still visible) dependence upon the dynamic shape factor.

CONTAIN calculations for LACE LA4 gave slightly better agreement with data for some thermal hydraulic variables. The reference MELCOR results were in better agreement with measured suspended aerosol masses during the post-injection, steady-state and vent. periods compared to results calculated by CONTAIN without any hygroscopic effects in the aerosol equations. The reference MELCOR results, without any hygroscopic effects modelled, were very similar to CONTAIN results for the suspended aerosol masses during the steady-state period obtained when hygroscopic effects were included. The reason for the difference in predicted suspended aerosol masses in the two codes is the larger aerosol particles calculated by MELCOR; the reason for the difference in aerosol particle sizes is primarily the different agglomeration shape factors used.

Although there has been a lot of discussion recently on numeric effects seen in other MELCOR calculations, no machine dependencies were seen in this problem, and smooth convergence in results with reduced time steps was demonstrated.

Bibliography

1. R. M. Summers et al., "MELCOR 1.8.0: A Computer Code for Severe Nuclear Reactor Accident Source Term and Risk Assessment Analyses", NUREG/CR-5531, SAND90-0364, Sandia National Laboratories, January 1991.
2. C. D. Leigh, ed., "MELCOR Validation and Verification - 1986 Papers", NUREG/CR-4830, SAND86-2689, Sandia National Laboratories, March 1987.
3. F. J. Rahn, "The LWR Aerosol Containment Experiments (LACE) Project Summary Report", EPRI NP-6094-D, LACE TR-012, Electric Power Research Institute, November 1988.
4. J. D. McCormack, et al., "Final Report of Experimental Results of LACE Test LA4 - Late Containment Failure with Overlapping Aerosol Injection Periods", LACE TR-025, Westinghouse Hanford Company, October 1987.
5. D. C. Slaughterback, "Pre- and Post-Test Thermal-Hydraulic Comparisons of LACE Test LA4", EPRI RP-2802-4, LACE TR-027, Intermountain Technologies, Inc., February 1988.
6. J. H. Wilson, P. C. Arwood, "Comparison of (Posttest) Predictions of Aerosol Codes with Measurements in LWR Aerosol Containment Experiment (LACE) LA4", ORNL M-991, LACE TR-084, Oak Ridge National Laboratory, February 1990.
7. K. K. Murata et al., "User's Manual for CONTAIN 1.1: A Computer Code for Severe Nuclear Reactor Accident Containment Analysis", NUREG/CR-5026, SAND87-2309, Sandia National Laboratories, November 1989.
8. F. Gelbard, J. L. Tills, K. K. Murata, "CONTAIN Code Calculations for the LA-4 Experiment", Sandia National Laboratories, Proceedings, 2nd International Conference on Containment Design and Operation, Oct. 14-17, 1990, Vol. 2.
9. "Input Deck for LACE LA-4", memo from K. E. Washington to L. N. Kmetyk, December 7, 1990.

•
•

•
•

A Reference Calculation Input Deck

```
*
*eor melgen
*
title 'LACE LA-4 (2-component)'
*
tstart -3000.0
*
diagf melgen_diagnostics
outputf melgen_output
plotf plot_file
restartf restart_file
*
* non-condensable gas input
ncg000 n2 4
ncg001 o2 5
*
**** control volume input: there are three control volumes ****
**** the first is the experimental vessel, the other two ****
**** are infinite volumes that border the vessel ****
*
cv00100 expvol 2 2 2 * nonequil therm, vertical flow, containment
cv001a0 3
cv001a1 mass.1 950.0 pvol 1.070e5 tpol 315.05
cv001a2 tatm 315.65 ph2o 7811. * ph2o = .0730*pvol
cv001a3 mlfr.4 0.79 mlfr.5 0.21
***cv001b1 0.0 0.0
***cv001b2 19.03 852. * height, volume
** first attempt to approximate bottom curvature
cv001b1 0.00 0.00
cv001b2 0.13 0.40
cv001b3 0.20 0.93
cv001b4 0.30 2.05
cv001b5 0.45 4.48
cv001b6 19.03 852.00
** first attempt to approximate bottom curvature
.
cv001c1 ae 101 3
cf10100 'cf101' tab-fun 1 1.0 0.0
cf10103 101
cf10110 1.0 0.0 time
tf10100 lights 4 1.0 0.0
tf10110 0.0 2.69e3
```

tf10111	102420.0	2.69e3		
tf10112	102420.1	0.0		
tf10113	999999.0	0.0		
			water leak	
cr001c2	mass.1	102	3	
cf10200	'cf102'	tab-fun	1 1.0 0.0	
cf10203	102			
cf10210	1.0	0.0	time	
tf10200	water	6	1.0 0.0	
tf10210	-99999.	0.0		
tf10211	27000.0	0.0		
tf10212	27000.1	0.0243		
tf10213	74400.0	0.0243		
tf10214	74400.1	0.0		
tf10215	999999.	0.0		
cr001c3	pe	112	3	
cf11200	'cf112'	tab-fun	1 1.0 0.0	
cf11203	112			
cf11210	1.0	0.0	time	
tf11200	water-enth	6	1.0 0.0	
tf11210	-99999.	0.0		
tf11211	27000.0	0.0		
tf11212	27000.1	1.52948e03		
tf11213	74400.0	1.52948e03		
tf11214	74400.1	0.0		
tf11215	999999.	0.0		
			saturated steam	
cr001c4	mass.3	103	3	
cf10300	'cf103'	tab-fun	1 1.0 0.0	
cf10303	103			
cf10310	1.0	0.0	time	
tf10300	steam	10	1.0 0.0	
tf10310	-99999.	0.0		
tf10311	-3000.1	0.0		
tf10312	-3000.0	0.451		
tf10313	0.0	0.451		
tf10314	0.1	0.048		
tf10315	4812.0	0.048		
tf10316	4812.1	0.029		
tf10317	36000.0	0.029		
tf10318	36000.1	0.0		

```

tf10319 999999. 0.0
cv001c5 ae 113 3
cf11300 'cf113' tab-fun 1 1.0 0.0
cf11303 113
cf11310 1.0 0.0 time
tf11300 steam-enth 14 1.0 0.0
tf11310 -99999. 0.0
tf11311 -3000.1 0.0
tf11312 -3000.0 1.24378e06
tf11313 0.0 1.24378e06
tf11314 0.1 1.33200e05
tf11315 1830.0 1.33200e05
tf11316 1830.1 1.33180e05
tf11317 3030.0 1.33180e05
tf11318 3030.1 1.33107e05
tf11319 4812.0 1.33107e05
tf11320 4812.1 7.99903e04
tf11321 36000.0 7.99903e04
tf11322 36000.1 0.0
tf11323 999999. 0.0
* nitrogen instrument purge gases
cv001c6 mass.4 104 3
cf10400 'cf104' tab-fun 1 1.0 0.0
cf10403 104
cf10410 1.0 0.0 time
tf10400 nit 16 1.0 0.0
tf10410 -99999. 0.0
tf10411 -3000.1 0.0
tf10412 -3000.0 0.0014
tf10413 0.0 0.0014
tf10414 0.1 0.0016
tf10415 1830.0 0.0016
tf10416 1830.1 0.0018
tf10417 3030.0 0.0018
tf10418 3030.1 0.0020
tf10419 16800.0 0.0020
tf10420 16800.1 0.0014
tf10421 36000.0 0.0014
tf10422 36000.1 0.0012
tf10423 342000.0 0.0012
tf10424 342000.1 0.0
tf10425 999999. 0.0
cv001c7 te 114 8

```

```

tf11400  nit-enth 1 1.0 0.0
tf11410  0.0 301.15
*          nitrogen thru aerosol line (period 1: -50min to 0)
cv001ca  mass 4 201 3
cf20100  'cf201' tab-fun 1 1.0 0.0
cf20103  201
cf20110  1.0 0.0 time
tf20100  nit-1 6 1.0 0.0
tf20110  -99999. 0.0
tf20111  -3000.1 0.0
tf20112  -3000.0 0.0027
tf20113   0.0 0.0027
tf20114   0.1 0.0
tf20115  999999. 0.0
cv001cb  te 211 8
tf21100  nit-1-enth 1 1.0 0.0
tf21110  0.0 433.15
*          nitrogen thru aerosol line (period 2: 0 to 30.5min)
cv001cc  mass.4 202 3
cf20200  'cf202' tab-fun 1 1.0 0.0
cf20203  202
cf20210  1.0 0.0 time
tf20200  nit-2 6 1.0 0.0
tf20210  -99999. 0.0
tf20211   -0.1 0.0
tf20212   0.0 0.067
tf20213  1830.0 0.067
tf20214  1830.1 0.0
tf20215  999999. 0.0
cv001cd  te 212 8
tf21200  nit-2-enth 1 1.0 0.0
tf21210  0.0 510.15
*          nitrogen thru aerosol line (period 3: 30.5 to 50.5min)
cv001ce  mass.4 203 3
cf20300  'cf203' tab-fun 1 1.0 0.0
cf20303  203
cf20310  1.0 0.0 time
tf20300  nit-3 6 1.0 0.0
tf20310  -99999. 0.0
tf20311  1830.0 0.0
tf20312  1830.1 0.066
tf20313  3030.0 0.066
tf20314  3030.1 0.0

```

```

tf20315 999999. 0.0
cv001cf te 213 8
tf21300 nit-3-enth 1 1.0 0.0
tf21310 0.0 526.15
<
nitrogen thru aerosol line (period 4: 50.5 to 80.2min)
cv001cg mass.4 204 3
cf20400 'cf204' tab-fun 1 1.0 0.0
cf20403 204
cf20410 1.0 0.0 time
tf20400 nit-4 6 1.0 0.0
tf20410 -99999. 0.0
tf20411 3030.0 0.0
tf20412 3030.1 0.067
tf20413 4812.0 0.067
tf20414 4812.1 0.0
tf20415 999999. 0.0
cv001ch te 214 8
tf21400 nit-4-enth 1 1.0 0.0
tf21410 0.0 535.15
<
nitrogen thru aerosol line (period 5: 80.2 to 280min)
cv001ci mass.4 205 3
cf20500 'cf205' tab-fun 1 1.0 0.0
cf20503 205
cf20510 1.0 0.0 time
tf20500 nit-5 6 1.0 0.0
tf20510 -99999. 0.0
tf20511 4812.0 0.0
tf20512 4812.1 0.0037
tf20513 16800.0 0.0037
tf20514 16800.1 0.0
tf20515 999999. 0.0
cv001cj te 215 8
tf21500 nit-5-enth 1 1.0 0.0
tf21510 0.0 469.15
<
nitrogen thru aerosol line (period 6: 280 to 600min)
cv001ck mass.4 206 3
cf20600 'cf206' tab-fun 1 1.0 0.0
cf20603 206
cf20610 1.0 0.0 time
tf20600 nit-6 6 1.0 0.0
tf20610 -99999. 0.0
tf20611 16800.0 0.0
tf20612 16800.1 0.0026

```

```

tf20613 36000.0 0.0026
tf20614 36000.1 0.0
tf20615 999999. 0.0
      20616 te 216 8
tf21600 nit-6-enth 1 1.0 0.0
tf21610 0.0 48.15
      nitrogen thru aerosol line (period 7: 600 to 5700min)
      2071cm mass:4 207 3
      207100 'tf207' tab-fun 1 1.0 0.0
      207110 207
      207110 1.0 0.0 time
      207100 nit-7 6 1.0 0.0
      207110 -99999 0.0
      207111 36000.0 0.0
      207112 36000.1 0.0022
      207113 342000.0 0.0022
      207114 342000.1 0.0
      207115 999999. 0.0
      2071cm te 214 8
      207170 nit-4-enth 1 1.0 0.0
      207171 0.0 393.15
      208201 atmw 1 2 6 * equil therm, vertical flow, containment
      208201 0 -1
      2082a0 8
      2082a1 vpol 0.0 pvol 1.054e5 tatk 305.00
      2082a2 mlfr:4 0.79 mlfr:5 0.21
      2082a3 -5.0 0.0
      2082a4 25.0 1000. * height, volume
      209301 atmw 1 2 6 * equil therm, vertical flow, containment
      209301 0 -1
      2093a0 8
      2093a1 vpol 0.0 pvol 0.986e05 tatk 297.0
      2093a2 mlfr:4 0.79 mlfr:5 0.21
      2093a3 -5.0 0.0
      2093a4 25.0 1000. * height, volume
      210101 'path-1' 1 2 16.5 16.5
      210101 2.478e-4 9.478 0.0
      210102 1.38e-1 15 0.70 0.70
      210101 1.38e-4 9.478 0.15
      210101 0.1 100 0.0

```

```

*
cf30100 'vent' tab-fun 1 1.0 0.0
cf30103 301
cf30110 1.0 0.0 time
tf30100 varea 6 1.0 0.0
tf30110 -99999. 0.0
tf30111 16800.0 0.0
tf30112 16800.1 1.0
tf30113 36000.0 1.0
tf30114 36000.1 0.0
tf30115 99999. 0.0

```

```

*
cf31100 'delp' add 2 1.0 0.0
cf31110 1.0 0.0 cwh-p.001
cf31111 -1.0 0.0 cwh-p.002

```

```

*
fl00200 'path-2' 1 3 19.0 19.0
fl00201 0.853 6.901 0.0
fl00203 .275 .275
fl002s1 0.853 6.901 0.26
fl002w1 301 302 302

```

```

*
cf30200 'relief' tab-fun 1 1.0 0.0
cf30203 302
cf30210 1.0 0.0 time

```

```

*
cf32100 'vlwtrip' t-o-f 1 1.0 0.0
cf32110 -1.0e9 0.0
cf32111 1.0 1.0 civalu.312

```

```

*
cf31200 'delta-p' add 2 1.0 0.0
cf31210 1.0 0.0 cwh-p.003
cf31211 -1.0 0.0 cwh-p.001

```

```

*
tf31210 'fract-area' 1 1.0 0.0
tf31211 1.0 1.0

```

* heat structure input

```

*
tf11100 hss 1 1.0 0.0
tf11111 1.0 1.0

```

* vessel, spinner and upper head steel/fiberglass


```

hs00001000 17 1 -1
hs00001001 'upper-head'
hs00001002 19.03 0.0
hs00001100 -1 1 0.0
hs00001101 0.0193 8
hs00001102 0.0443 17
hs00001200 -1
hs00001201 steel 7
hs00001202 fiberglass 16
hs00001300 0
hs00001400 1 1 ext 1.0 1.0
hs00001500 45.604 7.62 7.62
hs00001600 1 2 ext 1.0 1.0
hs00001700 45.604 7.62 7.62
hs00001800 -1
hs00001801 315.65 8
hs00001802 305.00 17

hs00002000 22 2 -1
hs00002001 'walls-edge'
hs00002002 0.0 1.0
hs00002100 -1 1 3.81
hs00002101 3.8269 14
hs00002102 3.8519 22
hs00002200 -1
hs00002201 steel 13
hs00002202 fiberglass 21
hs00002300 0
hs00002400 1 1 ext 1.0 1.0
hs00002500 428.5 17.9 17.9
hs00002600 1 2 ext 1.0 1.0
hs00002700 428.5 17.9 17.9
hs00002800 -1
hs00002801 315.65 13
hs00002802 305.00 22

- bottom head steel/fiberglass
hs00003000 17 1 -1
hs00003001 'floor'
hs00003002 -0.0443 -1.0e-7
hs00003100 -1 1 0.0
hs00003101 0.0193 8
hs00003102 0.0443 17

```

```

hs00003200 -1
hs00003201 steel 7
hs00003202 fiberglass 16
hs00003300 0
hs00003400 1 1 ext 0.0 0.0
hs00003500 45.604 7.62 7.62
hs00003600 1 2 ext 1.0 1.0
hs00003700 45.604 7.62 7.62
hs00003800 -1
hs00003801 315.65 8
hs00003802 305.00 17
*
* additional internals - vertical for plating
hs00004000 6 1
hs00004001 'int-roof'
hs00004002 19.03 0.0
hs00004100 -1 1 0.0
hs00004101 0.008149 6
hs00004200 -1
hs00004201 steel 5
hs00004300 0
hs00004400 1 1 ext 1.0 1.0
hs00004500 40.8 7.0 7.0
hs00004600 0
hs00004801 315.65 6
*
hs00005000 6 1
hs00005001 'int-walls'
hs00005002 3.0 1.0
hs00005100 -1 1 0.0
hs00005101 0.008149 6
hs00005200 -1
hs00005201 steel 5
hs00005300 0
hs00005400 1 1 ext 1.0 1.0
hs00005500 136.9 12.0 12.0
hs00005600 0
hs00005801 315.65 6
*
hs00006000 6 1
hs00006001 'int-floor'
hs00006100 -0.008149 -1.0e-7
hs00006101 -1 1 0.0

```



```

class 7 is MnO
rnas004 1 2 7 0.0 0.000757 7 2 * aerosol source (class 7)
rnas005 2 43e-6 1.70 * gmd, gsd
cf00700 'cf007' tab-fun 1 1.0 0.0
cf00703 007
cf00710 1.0 0.0 time
tf00700 asource 5 1.0 0.0 * tf for aerosol source
tf00710 -3030.0 0.0 1830.0 0.0 1830.1 1.0 3030.0 1.0 3030.1 0.0
rnas006 1 2 7 0.0 0.000757 8 2 * aerosol source (class 7)
rnas007 1.82e-6 2.56 * gmd, gsd
cf00800 'cf008' tab-fun 1 1.0 0.0
cf00803 008
cf00810 1.0 0.0 time
tf00800 asource 5 1.0 0.0 * tf for aerosol source
tf00810 -3030.0 0.0 3030.0 0.0 3030.1 1.0 4812.0 1.0 4812.1 0.0
cf00200 'rn mass 7' equals 1 1.0 0.0
cf00210 1.0 0.0 rn1-amgt-7-1.001
cf91100 'sum mass7' add 2 1.0 0.0
cf91110 1.0 0.0 cfvalu.7
cf91111 1.0 0.0 cfvalu.8
cf91200 'int mass7' integ 2 1.0 0.0
cf91201 0.0
cf91110 1.0 0.0 cfvalu.911
cf91211 1.0 0.0 time

cf00300 'rn leak 1' add 4 1.0 0.0
cf00310 1.0 0.0 rn1-cvclt-2-1.002
cf00311 1.0 0.0 rn1-cvclt-7-1.002
cf00312 1.0 0.0 rn1-cvclt-2-1.003
cf00313 1.0 0.0 rn1-cvclt-7-1.003

cf00400 'rn leak 2' add 2 1.0 0.0
cf00410 1.0 0.0 rn1-tyclt-2-1.6
cf00411 1.0 0.0 rn1-tyclt-7-1.6

cf00500 'rn mliq 1' add 2 1.0 0.0
cf00510 1.0 0.0 rn1-cvclt-2-1.001
cf00511 1.0 0.0 rn1-amgt-2-1.001

cf00600 'rn mliq 2' add 2 1.0 0.0
cf00610 1.0 0.0 rn1-cvclt-7-1.001
cf00611 1.0 0.0 rn1-amgt-7-1.001

```

```

*
cf99900 'rn mliq' add 2 1.0 0.0
cf99910 1.0 0.0 cfvalu.991
cf99911 1.0 0.0 cfvalu.992
*
*
cf89000 'saturation ratio' divide 2 1.0 0.0
cf89002 3 0.0 1.0
cf89010 1.0 1.0e-30 cvh-psat(tvap).001
cf89011 1.0 1.0e-30 cvh-ppart.3.001
*
cf89100 'total aerosol' add 7 1.0 0.0
cf89110 1.0 0.0 rn1-amgt-1-1.001
cf89111 1.0 0.0 rn1-amgt-2-1.001
cf89112 1.0 0.0 rn1-amgt-3-1.001
cf89113 1.0 0.0 rn1-amgt-4-1.001
cf89114 1.0 0.0 rn1-amgt-5-1.001
cf89115 1.0 0.0 rn1-amgt-6-1.001
cf89116 1.0 0.0 rn1-amgt-7-1.001
*
cf89200 'water fraction' divide 2 1.0 0.0
cf89202 3 0.0 1.0
cf89210 1.0 1.0e-30 cfvalu.891
cf89211 1.0 1.0e-30 rn1-amgt-5-1.001
*
cf89300 'check' divide 2 1.0 0.0
cf89302 3 0.0 1.0
cf89310 1.0 1.0e-30 rn1-amgt-5-1.001
cf89311 1.0 1.0e-30 cvh-mass.2.001
*
rnms000 1.85 2.25 1.37 1.0 0.001 0.05 1.0 1.0e-5
*
rnds000 1 lhs ceiling
rnds001 2 lhs wall
rnds002 3 lhs floor
rnds003 4 lhs ceiling
rnds004 5 lhs wall
rnds005 6 lhs floor
rnds006 1 rhs inactive
rnds007 2 rhs inactive
rnds008 3 rhs inactive
rnds009 4 rhs inactive
rnds010 5 rhs inactive

```

*rnds011 6 rhs inactive

*

rncc000 2 1 2 2 2 2 1

*

rnset000 2 2 0.0 1.0

rnset001 3 3 0.0 1.0

*

dchdecpow tf-009

dchclsnorm yes

dchdefcls0 1 2 3 4 5 6 7

*

tf00900 decay 2 1.0 0.0

tf00910 0.0 0.0 100.e5 0.0

*

**** material properties

* steel

*

mpmat00100 steel

mpmat00101 rho 11

mpmat00102 cps 12

mpmat00103 thc 13

*

tf01100 rho-steel 1 1.0 0.0

tf01111 0.0 7850.0

*

tf01200 cps-steel 1 1.0 0.0

tf01211 0.0 500.0

*

tf01300 thc-steel 1 1.0 0.0

tf01311 0.0 47.0

*

concrete

*

mpmat00200 concrete

mpmat00201 rho 21

mpmat00202 cps 22

mpmat00203 thc 23

*

tf02100 rho-concrete 1 1.0 0.0

tf02111 0.0 2320.0

*

tf02200 cps-concrete 1 1.0 0.0
tf02211 0.0 650.0

tf02300 thc-concrete 1 1.0 0.0
tf02311 0.0 1.6

fiberglass

mpmat00300 fiberglass
mpmat00301 cps 31
mpmat00302 thc 32
mpmat00303 rho 33

tf03100 cps-f 1 1.0 0.0
tf03101 0 0
tf03110 0.0 753.0

tf03200 thc-f 1 1.0 0.0
tf03201 0 0
tf03210 0.0 0.0467
tf03219 0.0 0.10

tf03300 rho-f 1 1.0 0.0
tf03301 0 0
tf03310 0.0 96.0

turn on radiation
tf041401 0.9 gray-gas-a 4.15
tf041402 0.9 gray-gas-a 4.15
tf041403 0.9 gray-gas-a 4.15
tf041404 0.9 gray-gas-a 4.15
tf041405 0.9 gray-gas-a 4.15
tf041406 0.9 gray-gas-a 4.15
tf041407 0.9 gray-gas-a 4.15
tf041408 0.9 gray-gas-a 4.15
tf041409 0.9 gray-gas-a 4.15

end material

turn off radiation

end tape

diagf melcor_diagnostics

messagef melcor_messages

outputf melcor_output

plotf plot_file

restartf restart_file

dttime 10.

rmedtflg 1 1 1

	tstart	dtmax	dtmin	dtedit	dtplot	dtrest
time1	0000.0	60.	0.01	3000.	60.	3000.
time2	1830.0	60.	0.01	1830.	60.	1830.
time3	1830.0	60.	0.01	1200.	60.	1200.
time4	3030.0	60.	0.01	1782.	60.	1782.
time5	4812.0	60.	0.01	6000.	60.	6000.
time6	16800.0	150.	0.01	9600.	150.	9600.
time7	36000.0	600.	0.01	61200.	600.	61200.
time8	34200.0	600.	0.01	20000.	600.	10800.
tend	34200.0					
cpulim	3600.					
cpuleft	100.					

err1001 7136 0.0 2

err1012 7136 0.0 7

External Distribution:

Dr. P. Hosemann
Paul Scherrer Institute
CH-5303 Würenlioren
Switzerland

Mr. J. Duco
CEA
60-68 Avenue du General Leclerc
BP No. 6
92065 Fontenay-aux-Roses CEDEX
France

Mr. J. Puga
Unidad Eléctrica, S.A.
Francisco Gervás, 5
E-28020 Madrid
Spain

Mr. A. Markovina
Commission of the European Communities
Reactor Safety Division
Project Directorate
Joint Research Center, Ispra
I-21020 Ispra (Varese)
Italy

Mr. P. Fiorio
ENEA
CRE Casaccia
Via Anguillarese, 301
I-00060 S. Maria di Galeria, Rome
Italy

Mr. G. Eresman
Ontario Hydro
700 University Avenue
Toronto, Ontario
M5G 1X6 Canada

Dr. M. Hayns
Dept. Director Water Reactors Program
Harwell Atomic Energy Research Establishment
Didcot Oxon
OX11 0RA United Kingdom

Dr. K. Kollath
Gesellschaft für Reaktorsicherheit
Schwertnergasse 1
D-5000 Köln 1
Germany

Mr. K. Elisson
ASEA-ATOM
Box 53
S-72104 Vasteras
Sweden

Dr. D. Squarer
R&D Center
Westinghouse Electric
1310 Beulah Road
Pittsburgh, PA 15235

Dr. Y. C. Yeh
Dept. of Nuclear Regulation
Atomic Energy Council
67 Lane 144
Keelung Road, Section 4
Taipei, Taiwan
Republic of China

Dr. F. Rahn
Electric Power Research Institute
P. O. Box 10412
Palo Alto, CA 94303

Mr. A. Verkooijen
KEMA
P. O. Box 9035
6800 ET Arnhem
The Netherlands

Mr. W. Paschdag
Office of LWR Safety and Technology
Office of Nuclear Energy NE-42
U. S. Department of Energy
Washington, DC 20545

Prof. A. Sukhorovskii
I.V. Kurchatov Institute of Atomic Energy
125182 Moscow
Kurchatov Square
USSR

Dr. O. Gremm
Siemens A.G. KWV
Hammerbacherstrasse 12-14
Postfach 5220
D-8520 Erlangen
Germany

Dr. B. Kneize
Prüfunggruppe LWR-Sicherheit
KFK
Postfach 6649
D-7500 Karlsruhe
Germany

Dr. A. Wright
Oak Ridge National Laboratory
Bldg. 4700N-Room A10
P. O. Box K
Oak Ridge, TN 37831

Dr. A. de Witte
CNSA - MIRA
Delft University
Delft, The Netherlands
Delft, The Netherlands

Mr. J. J. van den Berg
Office of Energy Research and Nuclear Safety
7000 14th Avenue, 2nd Floor, Room 4
Washington, DC 20545
Department of Energy

Jai-Hsi Kao, Associate Scientist
Atomic Energy Control
Institute of Nuclear Energy Research
106, Ring Road
Tsing-Tai, 32500
Taipei
Republic of China

Saraj S. Chongs
Atomic Energy of Canada Limited
OASD-Operations
Sheridan Park Research Community
Mississauga, Ontario
Canada L7R 4R2

Cheng-Hsiung Chang
Canadian Nuclear Laboratories
7000, 14th Avenue
Kingston, Ontario K6H 1R9

Cheng-Hsiung Chang
Canadian Nuclear Laboratories
1250, 14th Avenue
Kingston, Ontario K6H 1R9

Cheng-Hsiung Chang, Associate Scientist
107, Ring Road
Atomic Energy of Canada Limited
Institute of Nuclear Energy Research
Tsing-Tai, 32500
Taipei, Republic of China

Cheng-Hsiung Chang
Atomic Energy of Canada Limited
1250, 14th Avenue
Kingston, Ontario K6H 1R9

Cheng-Hsiung Chang
Atomic Energy of Canada Limited

Cheng-Hsiung Chang
Atomic Energy of Canada Limited
1250, 14th Avenue
Kingston, Ontario K6H 1R9
Canada

Brookhaven National Laboratory (2)
Bldg. 130
32 Lewis
Upton, NY 11973
Attn: I. K. MacIn,
T. Pratt

Juan Bagues
Consejo de Seguridad Nuclear
Justo Dorado, 11
28040, Madrid
Spain

D. Jones
EI International
P. O. Box 50736
Idaho Falls, ID 83405

Giovanni Saponaro
ENEA
Natl. Comm. for R&D of Nuclear Energy
Via Vitaliano Brancati, 48
00144 Rome
Italy

Electric Power Research Institute (3)
P. O. Box 10412
Palo Alto, CA 94303
Attn: E. Fuller
R. N. Oehlberg
B. R. Singal

M. J. S. Khan (2) (2) (2) (2) (2)
Energy Research Corp.
P. O. Box 2074
Rockville, MD 20852

M. P. S.
Energy Research Corp.
10407 Woodmont Street
Bethesda, MD 20814

1000 V. S. ...
American Center Radiation & Nucl. Safety
Department Nuclear Safety
P.O. Box 208
Spartanburg, SC 29583
1980

1000 V. S. ...
1000 V. S. ...
1000 V. S. ...
1000 V. S. ...
1000 V. S. ...

1000 V. S. ...
1000 V. S. ...
1000 V. S. ...
1000 V. S. ...
1000 V. S. ...
1000 V. S. ...
1000 V. S. ...
1000 V. S. ...

1000 V. S. ...
1000 V. S. ...
1000 V. S. ...
1000 V. S. ...
1000 V. S. ...

1000 V. S. ...
1000 V. S. ...
1000 V. S. ...
1000 V. S. ...
1000 V. S. ...

1000 V. S. ...
1000 V. S. ...
1000 V. S. ...
1000 V. S. ...
1000 V. S. ...

1

1

France National Engineering Laboratory (3)
10, rue de l'Industrie
P.O. Box 1025
Marcy l'Etoile, F-69104
Attn: A. Brown,
Dr. J. Delmon,
Dr. W. Gobner

Japan Atomic Energy Research Inst.
Chemical Safety Engineering Lab.
Tama-ku, Naka-gun, Ibaraki-ken
305, Japan

Dr. S. Ito, Special Director General
Japan Institute of Nuclear Safety
1-1-1, Kashiwa, Tama-ku Bldg. 7F
6-17-1, Toratsunan
Mitsuda-Ku, Tokyo, 105
Japan

K. H. Hellmann
Karlsruhe Forschungszentrum Karlsruhe
Institut für Material- und Festkörperforschung
P.O. Box 104
76075 Karlsruhe 1
Germany

Dr. T. Kikuchi
Kyushu Advanced Energy Research Inst.
P.O. Box 7, Tsurumi 104-1
816
Saitama-Ken, 365-0255
Japan

U.S.A. Argonne National Laboratory (4)
9700 S. Cass Ave.
Argonne, NM 60439
Attn: Dr. J. Hryniak, K-551
Dr. R. L. Fleck, K-553
Dr. R. A. Johnson, K-555
Dr. S. J. Zinkle, K-555

Prof. Augustin Alonzo Santos
Universidad Politecnica de Madrid
E.T.S. Ingenieros Industriales
Jose Gutierrez Abascal, 2
28006 Madrid
Spain

Karel J. Brinkmann
Netherlands Energy Research Foundation
P. O. Box 1
1755 ZG Petten
The Netherlands

B. Raychaudhuri
Nebraska Public Power District
PRA & Engineering Review Group
P. O. Box 499
Columbus, NE 68601

U. S. Nuclear Regulatory Commission (16)
Washington, DC 20555

Attn: S. Acharya, NLS-372
Y. S. Chen, NLN-344
M. A. Cunningham, NLS-372
F. Eltawila, NLN-344
R. B. Founds, NLN-344
C. G. Tinkler, NLN-344
L. E. Lancaster, NLS-372
R. O. Meyer, NLS-007
J. A. Mitchell, NLS-314
C. P. Ryder, NLS-372
L. Soffer, NLS-324
B. Sheron, NLS-007
J. A. Murphy, NLS-007
L. M. Shotkin, NLN-333
A. Notarfrancesco, NLN-344
N. Lauben, NLN-353
R. Landry, NLN-344

S. Chakraborty
Swiss Federal Nuclear Safety Inspectorate
CH-5303 Würenlingen
Switzerland

Oak Ridge National Laboratory (8)
P. O. Box 2009
Oak Ridge, TN 37831-8057
Attn: S. R. Greene, MS-8057
T. L. Heatherly, MS-8057
S. A. Hodge, MS-8057
C. R. Hyman, MS-8057
B. W. Patton, MS-8057
D. B. Simpson, MS-8057
R. P. Taleyarkhan, MS-8057
M. L. Tobias, MS-8088

Peter P. Bieniarz
2309 Dietz Farm Road NW
Albuquerque, NM 87107

Savannah River Laboratory (2)
Westinghouse Savannah River Co.
Bldg. 773-41A
Aiken, SC 29808-0001
Attn: J. K. Norkus
L. A. Wooten

Science Applications Intl. Corp. (4)
2109 Air Park Rd. SE
Albuquerque, NM 87106
Attn: E. Dombrowski
M. T. Leonard
K. C. Wagner
K. A. Williams

Frank Elia
Stone & Webster Engineering Corp.
215 Summer Street
Boston, MA 02210

R. Viskanta
Purdue University
Heat Transfer Laboratory
School of Mechanical Engineering
West Lafayette, IN 47907

Mr. J. R. D. D. D. D.
Director
Office of Research
United States Power Inspectorate
Systems Research Institute
Washington, D. C.
20548-0001
202-277-1000

Mr. J. R. D. D. D.
Director
General Engineering Laboratory
General Research Centre of England
200, High Road
Barnsley, Yorkshire
S70 2BQ

Mr. J. R. D. D. D.
200, High Road
Barnsley, Yorkshire

Mr. J. R. D. D. D. (2)
200, High Road
Barnsley, Yorkshire
S70 2BQ

Mr. J. R. D. D. D. Atomic Energy Agency (2)
200, High Road
Barnsley, Yorkshire
S70 2BQ

Mr. J. R. D. D. D. Atomic Energy Agency (2)
200, High Road
Barnsley, Yorkshire
S70 2BQ

Mr. J. R. D. D. D.
200, High Road

E. E. Macalin
University of New Mexico
Department of Chemical and Nuclear Engineering
Albuquerque, NM 87131

J. C. Lee
University of Michigan
Dept. of Nuclear Engineering
Cooper Building, North Campus
College of Engineering
Ann Arbor, MI 48109-2104

University of Wisconsin (3)
Dept. of Nuclear Engineering
Engineering Research Building
1500 Johnson Drive
Madison, WI 53706
Attn: M. L. Corradini
G. A. Moses
T. J. Tautges

Dr. John Gleske
Battelle Memorial Institute
3675 Kinn Ave.
Columbus, Ohio 43201

Sung-Hong Chon
Paul Scherrer Institute
CH-5200 Würenlingen
Switzerland

Westinghouse Hartford Co. (2)
P. O. Box 1970
Richmond, WA 99352
Attn: D. Ogden
O. Wang

György Gyenes
Central Research Institute for Physics
Institute for Atomic Energy Research
H-1525 Budapest
P. O. Box 49
Hungary

Dr. Valery F. Strizhov
USSR Academy of Science
Institute of Nuclear Safety
Moscow, G. Tul'sky, 52
113191, USSR

Oddbjörn Sanderväg
Statens Kärnkraftinspektion
Swed. L. Nuclear Power Inspectorate
Box 27106 102 52 Stockholm
Sweden

Internal Distribution:

6344 E. Gelbard
6344 S. W. Webb
6400 D. J. McCloskey
6401 J. E. Kelly
6402 K. D. Bergeron
6410 D. A. Dahlgren
6412 A. L. Camp
6412 S. E. Dingman
6413 F. T. Harper
6418 S. L. Thompson (10)
6418 E. A. Boucheron
6418 R. K. Cole
6418 A. A. Elsbernd
6418 R. J. Gross
6418 E. N. Kuczyk (10)
6418 R. S. Longenbaugh
6418 G. M. Martinez
6418 R. C. Smith
6418 D. S. Stant
6418 R. M. Summers
6429 W. B. Guenter
6429 K. E. Washington
6429 K. K. Murata
6429 J. Tills
6441 S. A. Landenberger (5)
6457 Document Processing for DOE OSTI (8)
6454 G. C. Claycomb (3)
8523 2 Central Library Files

END

**DATE
FILMED**

01/09/91

